Water vapour in the UTLS – Climatologies and Transport

Patrick Rudolf Neis

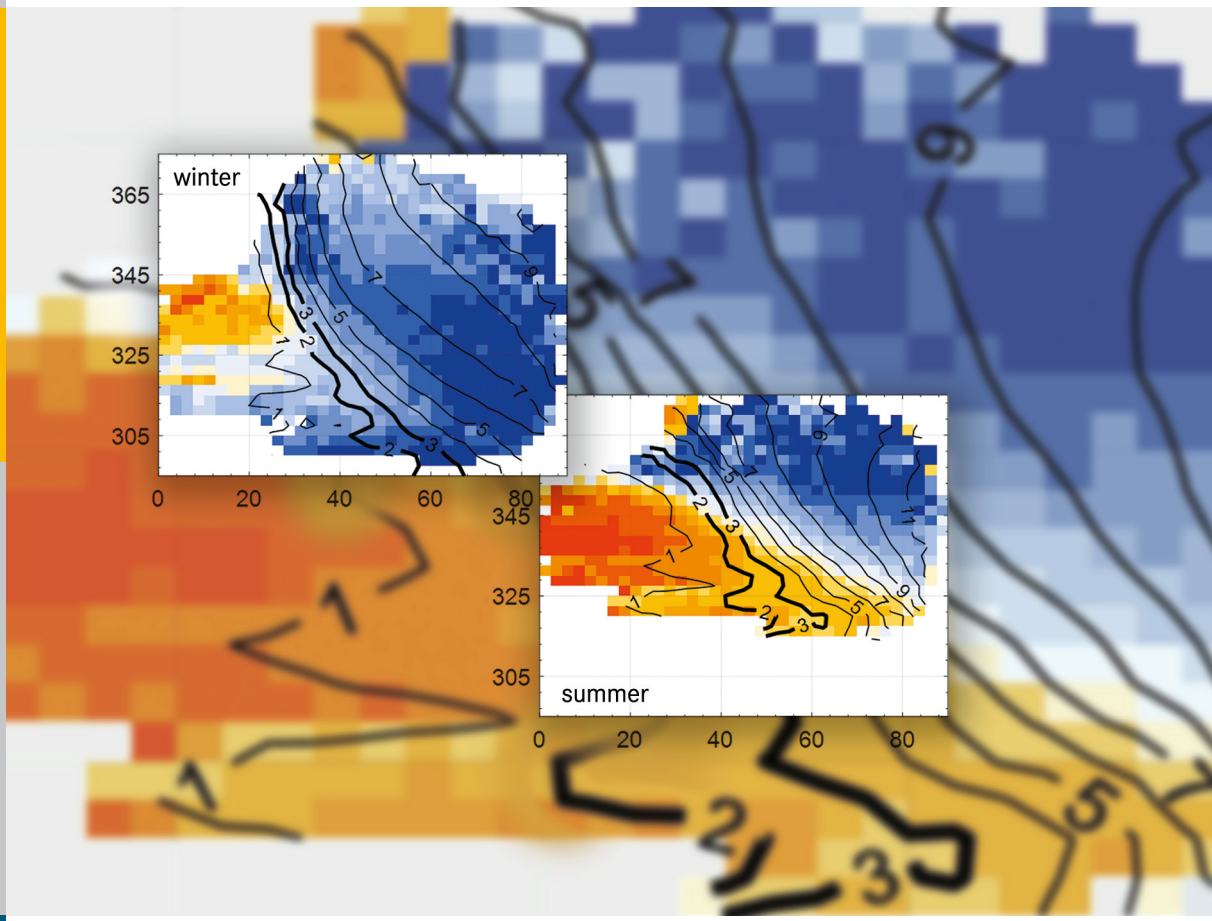

Energie & Umwelt / Energy & Environment
Band / Volume 394
ISBN 978-3-95806-269-6

JÜLICH
FORSCHUNGSZENTRUM

Schriften des Forschungszentrums Jülich
Reihe Energie & Umwelt / Energy & Environment Band / Volume 394

Forschungszentrum Jülich GmbH
Institute of Energy and Climate Research
Troposphere (IEK-8)

Water vapour in the UTLS – Climatologies and Transport

Patrick Rudolf Neis

Schriften des Forschungszentrums Jülich
Reihe Energie & Umwelt / Energy & Environment Band / Volume 394

ISSN 1866-1793 ISBN 978-3-95806-269-6

Bibliographic information published by the Deutsche Nationalbibliothek.
The Deutsche Nationalbibliothek lists this publication in the Deutsche Nationalbibliografie; detailed bibliographic data are available in the Internet at http://dnb.d-nb.de.

Publisher and Distributor:	Forschungszentrum Jülich GmbH Zentralbibliothek 52425 Jülich Tel: +49 2461 61-5368 Fax: +49 2461 61-6103 Email: zb-publikation@fz-juelich.de www.fz-juelich.de/zb
Cover Design:	Grafische Medien, Forschungszentrum Jülich GmbH
Printer:	Grafische Medien, Forschungszentrum Jülich GmbH
Copyright:	Forschungszentrum Jülich 2017

Schriften des Forschungszentrums Jülich
Reihe Energie & Umwelt / Energy & Environment, Band / Volume 394

D 77 (Diss. Mainz, Univ., 2017)

ISSN 1866-1793
ISBN 978-3-95806-269-6

The complete volume is freely available on the Internet on the Jülicher Open Access Server (JuSER) at www.fz-juelich.de/zb/openaccess.

ABSTRACT

The knowledge about the water vapour distribution in the upper troposphere and lower stratosphere is essential for understanding the cloud formation processes and the Earth's radiation budget. Since 1994, the European infrastructure MOZAIC (since 2011 IAGOS) measures water vapour, temperature as well as different essential climate variables, such as ozone and carbon monoxide (since 2001), aboard commercial passenger aircraft. Before analysing this more than two-decades comprehensive data set, the MOZAIC capacitive hygrometer is evaluated in a blind intercomparison against high precision water vapour instruments with the resulting sensors uncertainty of 5% relative humidity. To assure the data quality and the consistency of the data set, the new and improved IAGOS capacitive hygrometer is also evaluated against high precision water vapour instruments in a subsequent blind intecomparison. The water vapour data set is analysed with high vertical resolution around the thermal tropopause in the North Atlantic flight corridor and shows an increased probability of ice supersaturation with decreasing distance to the tropopause. This probability is especially pronounced in winter, but partially underestimated in its quantity in global weather models. Further analyses show a quasi-isentropic troposphere-to-stratosphere transport of water vapour near 50°N and below 350 K of potential temperature in summer. Within a final case study the future potential of the IAGOS data set is demonstrated by using the new cloud index besides the simultaneous water vapour measurements to separate the water vapour distributions into clear sky and in-ice cloud data. With this separation, investigations show different amounts of cloud occurrence and cloud properties for different global regions.

ZUSAMMENFASSUNG

Das Wissen über die Verteilung des Wasserdampfs in der oberen Troposphäre und unteren Stratosphäre ist essenziell für das Verständnis der Wolkenbildung und somit der Strahlungsbilanz der Erde. Seit 1994 wird im Rahmen der europäischen Infrastruktur MOZAIC (ab 2011 IAGOS) der Wasserdampf, die Temperatur sowie verschiedene essentielle Klimavariablen wie Ozon oder Kohlenstoffmonoxid (ab 2001) an Bord von kommerziellen Passagierflugzeugen gemessen. Um diesen auf derzeit über zwei Jahrzehnte angewachsenen Datensatz zu analysieren, wird zu Beginn der Arbeit das kapazitive MOZAIC-Hygrometer in einem Blindvergleich mit hochpräzisen Hygrometern evaluiert und die Unsicherheit des Sensors auf 5% relative Feuchte bestimmt. Im Anschluss wird durch einen weiteren Blindvergleich des weiterentwickelten, kapazitiven IAGOS-Hygrometer mit hochpräziesen Hygrometern die Datenqualität beim Übergang der beiden Sensoren gewährleistet. Eine vertikal hochaufgelöste Analyse der Wasserdampfmessungen um die thermische Tropopause im nordatlantischen Flugkorridor zeigt eine steigende Wahrscheinlichkeit der Eisübersättigung mit der Annäherung an die Tropopause. Diese von globalen Wettermodellen zum Teil in der Quantität unterschätzte Wahrscheinlichkeit ist besonders im Winter ausgeprägt, wobei im Sommer ein quasi-isentroper Troposphäre-nach-Stratosphäre Transport von Wasserdampf im Bereich 50°N und unterhalb 350 K potenzieller Temperatur beobachtet wird. In einer abschließenden Fallstudie wird das zukünftige Potenzial des IAGOS Datensatzes aufgezeigt, indem Wasserdampfmessungen und simultane Wolkenindexmessungen benutzt werden, um eine vertiefende Analyse der Wasserdampfverteilungen außerhalb und innerhalb von Eiswolken im Hinblick auf das Wolkenauftreten und deren Eigenschaften durchzuführen.

ACRONYMS

AIRTOSS-ICE	AIRcraft TOwed Sensor Shuttle - Inhomogeneous Cirrus Experiment
BCP	Backscatter Cloud Probe
CARIBIC	Civil Aircraft for the Regular Investigation of the Atmosphere Based on an Instrument Container
CIRRUS-III	Cirrus 3 campaign
ECMWF	European Centre for Medium Range Weather Forecast
EMA	Exponential Moving Average
FISH	Fast In-Situ Hygrometer
IAGOS	In-service Aircraft for a Global Observing System
ICH	IAGOS Capacitive Hygrometer
IFC	In-Flight Calibration
ISSR	Ice Supersaturated Region
JOE	Jülich Ozone Experiment
MCH	MOZAIC Capacitive Hygrometer
ML	Mid-Latitudes
MOZAIC	Measurement of OZone and water on Airbus In-service airCraft
NRT	Near Real-Time

PDF	Probability Density Function
PI	Principle Investigator
OJSTER	Open-path Jülich Stratospheric TDL ExpeRiment
SEALDH-II	Selective Extractive Airborne Laser Diode Hygrometer II
ST	Subtropics and Tropics
TDL	Tunable Diode Laser
TL	Tropopause Layer
TPH	Tropopause Height
UTH	Upper Tropospheric Humidity
UTLS	Upper Troposphere Lowermost Stratosphere
WMO	World Meteorological Organization
N_{ice}	Ice Crystal Number Concentration
PV	Potential Vorticity
RH_{ice}	Relative Humidity with respect to ice
RH_{liquid}	Relative Humidity with respect to liquid water
SAT	Static Air Temperature
TAT	Total Air Temperature
TRT	Total Recovery Temperature
VMR	Volume Mixing Ratio

CONTENTS

LIST OF PUBLICATIONS

During my time as PhD student several parts of my study have been published. These publications were partially peer-reviewed and are used to write this thesis. A list of these publications with the description of my contribution will be listed in the following.

- Smit et al. [2014]
  Smit, H. G. J., Rohs, S., **Neis, P.**, Boulanger, D., Krämer, M., Wahner, A., and Petzold, A.: **Technical Note: Reanalysis of upper troposphere humidity data from the MOZAIC programme for the period 1994 to 2009**, Atmos. Chem. Phys., 14, 13241–13255, doi:10.5194/acp-14-13241-2014, 2014.
  It was my part to perform a first analysis of the MOZAIC Capacitive Hygrometer (MCH) performance during the aircraft field campaign CIRRUS-III. During this campaign the MCH is evaluated briefly against well-established scientific hygrometer.

- Neis et al. [2015a]
  Neis, P., Smit, H. G. J., Krämer, M., Spelten, N., and Petzold, A.: **Evaluation of the MOZAIC Capacitive Hygrometer during the airborne field study CIRRUS-III**, Atmos. Meas. Tech., 8, 1233-1243, doi:10.5194/amt-8-1233-2015, 2015a.
  It was my part to perform the comprehensive analysis of the MOZAIC Capacitive Hygrometer (MCH) performance during the aircraft field campaign CIRRUS-III. Besides the evaluation against well-established scientific hygrometer, the manuscript was written as lead author.

- Neis et al. [2015b]

  Neis, P., Smit, H. G. J., Rohs, S., Bundke, U., Krämer, M., Spelten, N., Ebert, V., Buchholz, B., Thomas, K., and Petzold, A.: **Quality assessment of MOZAIC and IAGOS capacitive hygrometers: insights from airborne field studies**, Tellus B, 67, 28320, doi:10.3402/tellusb.v67.28320, 2015b.

  It was my part to perform the comprehensive analysis of the improved IAGOS Capacitive Hygrometer (ICH) performance during the aircraft field campaign AIRTOSS-ICE. During this campaign the ICH was evaluated against well-established scientific hygrometer and the results compared against the performance of the precursor MCH to ensure the transition to the new hygrometer. The manuscript was written as lead author.

- Clark et al. [2015]

  Clark, H., Sauvage, B., Thouret, V., Nédélec, P., Blot, R., Wang, K. Y., Smit, H. G. J., **Neis, P.**, ... , Cammas, J.-P.: **The first regular measurements of ozone, carbon monoxide and water vapour in the Pacific UTLS by IAGOS**, Tellus B, 67, 28385, doi:10.3402/tellusb.v67.28385, 2015.

  It was my part to process and to analyse the water vapour measurements of the studied IAGOS flights.

- Petzold et al. [2017]

  Petzold, A., Krämer, M., **Neis, P.**, Rolf, C., Rohs, S., Berkes, F., Smit, H. G. J., Gallagher, M., Beswick, K., Lloyd, G., Baumgardner, D., Spichtinger, P., Nédélec, P., Ebert, V., Buchholz, B., Riese, M., and Wahner, A.: **Upper tropospheric water vapour and its interaction with cirrus clouds as seen from IAGOS long-term routine in-situ observations**, Faraday Discuss., doi:10.1039/C7FD00006E, 2017.

  It was my part to process and to analyse the water vapour measurements of the studied IAGOS flights in the dependency of the new IAGOS parameter $cloud\ index$. Furthermore, it was my part to contribute to the manuscript.

CHAPTER 1

GENERAL INTRODUCTION

1.1 The Role of Water Vapour

Water enables and controls life on Earth.
Water can co-exist on the planet in the aggregates gaseous, liquid, and solid and thus effect human life, the climate and the weather. Its role in climate and weather is differentiated and is divided by the oceans, the ice masses, the clouds, and the humidity in the atmosphere [Peixoto and Oort, 1996].

In gaseous form, water vapour plays a major role in the balance of planetary radiation (Figure 1.1) as arguably the most important greenhouse gas in the Earth's atmosphere [Held and Soden, 2000]. As greenhouse gas, water vapour accounts for about 67% of the natural greenhouse effect at clear sky conditions which is defined as the difference between the planetary blackbody emitting temperature, by assuming a constant albedo, and the global mean surface temperature [Wild et al., 2013]. The reduction in outgoing long-wave radiation flux by absorption and emission of long-wave radiation in the atmosphere causes the actual global mean surface temperature of human-life-enabling 15°C, and is thus 33°C larger compared to an atmosphere without greenhouse gases. In an ideal situation, climate of the Earth and chemical composition of the atmosphere are finely balanced systems [Thompson, 1992].

Although, water vapour and its condensed form clouds account in sum for 75% of the natural greenhouse effect [Wild et al., 2013], anthropogenic changes in atmospheric carbon dioxide (CO_2) governs the temperature of the Earth's atmosphere. In contrast to the non-condensing greenhouse gases like CO_2, water vapour can condense and precipitate in the atmosphere and therefore water vapour concentrations are de-

termined by the temperature [Lacis et al., 2010]. This, in turn, makes the climate more sensitive to forcing by the non-condensable greenhouse gases with an additional radiative forcing and thus a changing in the atmospheric temperature caused by water water and cloud abundance adjustments (”water vapour feedback”) [Lacis et al., 2010].

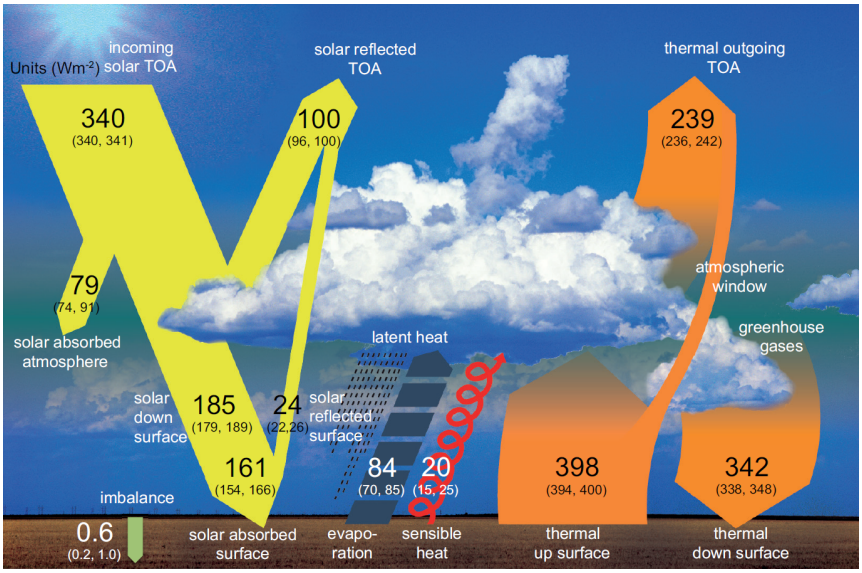

Figure 1.1: Schematic of planetary radiation budget under present-day climate conditions. Numbers represent best estimates for the magnitudes of the individual energy fluxes in W m^{-2}. Numbers in parentheses cover the range of uncertainties. The incoming and the sum of outgoing top-of-atmosphere (TOA) fluxes equalises. (Adapted from Wild et al. [2013].)

Studies showed that the effect of water vapour on the Earth’s radiative balance is that large that small errors in the spectroscopic parameters in global climate models can produce potentially large uncertainties in the prediction of the future climate. To avoid these large uncertainties in the calculated forcings, the humidity concentration, particularly in the upper troposphere may need to be known with an accuracy in the range of 3-10% [Harries, 1997]. The reason is, that upper troposphere (UT) and lowermost stratosphere (LS) is where the air is coldest and driest [Dessler and Sherwood, 2009, Held and Soden, 2000], and therefore the reduction of outgoing long-wave radiation is most sensitive to absolute changes in the UTLS water vapour [Riese et al., 2012].

Forster and Shine [2002] calculated that if the estimated lower stratospheric H_2O mixing ratio trends since 1960, is occurring globally, the contribution to surface warming would be 75% of that from the CO_2 alone. Forster and Shine also highlighted that an increase of water vapour causes a cooling of the lower stratosphere that is comparable to the contribution due to greenhouse gases and ozone changes alone. These

facts and the demand to refine experiments about background climatology of water vapour, underlines the urgent need to understand and assess the long-term changes and decadal scale trends by continuous observations [Dessler et al., 2013, Forster and Shine, 2002, Kley et al., 2000, Müller et al., 2016, Solomon et al., 2010].

Besides the major role in the planetary radiation balance, water vapour distributions in the upper troposphere and lower stratosphere influences the UTLS chemistry. Stratospheric water vapour, for example, is a product of photochemical methane oxidation and will increase with anthropogenically increasing tropospheric methane concentrations. This increase of water vapour could in a next step lead to a more frequent formation of polar stratospheric clouds and, finally, lead to ozone destruction in the stratosphere. The chemical impact of tropospheric water vapour is, for example, the reaction with photolysed ozone to the hydroxyl radical OH (”tropospheric vacuum cleaner”) which further reacts with hundreds of gases and also leads to the rapid formation of acids that are deposit in precipitation (”acid rain”) [Rohs et al., 2006, Thompson, 1992].

Another important aspect of water vapour distribution in the atmosphere is that it affects and responds to atmospheric motions that shape the global circulation of the atmosphere and thus climate. The hydrological cycle describes the movement of water within and between the Earth’s atmosphere, oceans, and continents. As water vapour, it is moved quickly through the atmosphere and redistributes energy related to evaporation and condensation of water within its global mean residence time of about 9 days [van der Ent and Tuinenburg, 2017].

The amount of energy is a function of surface and atmosphere temperature which is expressed in the Clausius-Clapeyron relation. This relation explains the water-holding capacity, or ”equilibrium vapour pressure”, of the atmosphere and describes a fractional increase of the saturation vapour pressure of 6-7% if the temperature increases 1 K [Held and Soden, 2000, Schneider et al., 2010]. Since global warming is a recent topic, also changes in the key component of the global atmospheric general circulation (Figure 1.2), the tropospheric Hadley circulation, are expected. Lau and Kim [2015] calculated based on these changes implications for convective ascent, cloud patterns, and thus the tropospheric humidity distribution, particularly in the tropics. They conclude that a global warming dependent moister increase in the tropical lower troposphere leads to amplification in the vertical convective mass flux, resulting in increased high clouds, suppressed low clouds, higher level of mass flow in the pole direction, a widening of subsidence zones with conjunction of increased frequency of dry events worldwide.

Another consequence is on the global mass circulation of tropospheric air through the stratosphere, the so-called Brewer-Dobson circulation (Figure 1.2), which is characterised by tropospheric air rising into the stratosphere in the Tropics, moving poleward before descending in the middle and high latitudes [Butchart, 2014, Plumb, 2002]. Bönisch et al. [2011] adduce proof that the observed increase in tropical upwelling may be attributed to a change in the Brewer-Dobson circulation pattern, i.e. the increased upwelling has the potential to trigger an intensified tracer transport from the tropical into the extratropical lower stratosphere which is part of the lower branch of the Brewer-Dobson circulation. Randel et al. [2006] found also that the enhanced tropical upwelling may cause the lower temperatures and lower water vapour near the tropical

tropopause which result in the globally and locally over Boulder, Colorado (40°N) observed decrease in the water vapour.

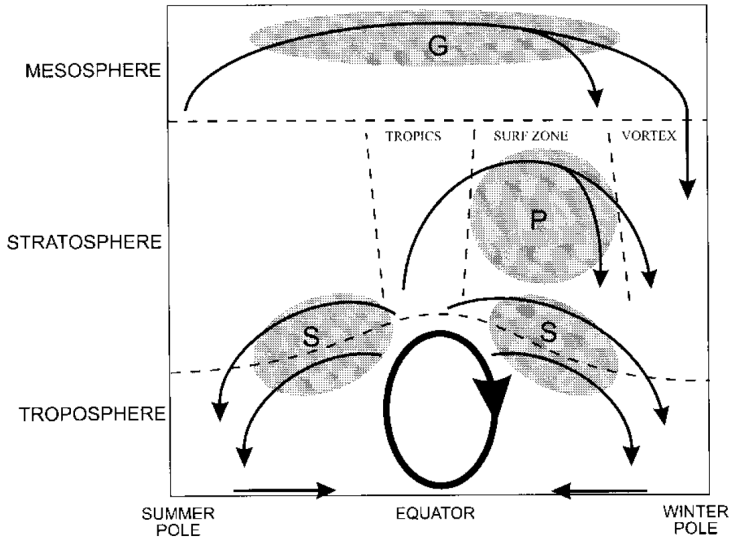

Figure 1.2: Schematic of residual mean meridional circulation in the atmosphere. The bold lined ellipse in the troposphere represents the thermally-driven Hadley circulation, whereas the single-ended arrows show the motion branches for the stratospheric and mesospheric circulation which develop in the shaded regions of breaking waves, i.e. synoptic- ("S"), planetary-scale ("P"), and gravity ("G") waves. (Adapted from Plumb [2002].)

Previously mentioned changes in the tropospheric humidity distribution also affects microphysical processes via the humidity-cloud interaction. And in particular these fundamental details of microphysical processes of ice clouds are still poorly understood which is an issue in the latest assessment report of the Intergovernmental Panel on Climate Change [abbreviated as IPCC, 2013]. The report states that clouds and aerosols continue to contribute the largest uncertainty to estimates and interpretations of the Earth's changing energy budget. Today's understanding of the impact of cirrus clouds on climate is still consistent with the conclusions by Cox [1991] of a significant warming tendency of tropical cirrus and a cooling effect of mid-latitude cirrus. However, the net global effect of cirrus clouds is currently still uncertain but with the assumption of a warming effect [Mitchell and Finnegan, 2009].

The control mechanism for cloud formation in the upper troposphere is relative humidity (RH), which reaches the necessary supersaturation when exceeding the temperature dependent water-holding capacity e_s of the air mass [Gierens et al., 2000, Spichtinger et al., 2003b].

$$\mathrm{RH} = 100 \cdot \frac{e}{e_s(\mathrm{T})}, \tag{1.1}$$

where e is the present water vapour partial pressure and e_s is the water vapour saturation pressure over liquid or ice water at temperature T, respectively. [1]

Thus, the intensity of dynamic motion, the presence and composition of so-called ice condensation nuclei (such as soot or biological particles) will influence the location, extension, and frequency of cirrus clouds and consequently the radiation balance [e.g. Gettelman and Kinnison, 2007, Krämer et al., 2009, 2016].

Besides the formation of cirrus clouds, growing ice crystals deplete humidity as a function of their number and size, which leads typically after around 0.5-1 days in ice supersaturation to crystal diameter sizes of 10 to 20 μm. The thereby beginning sedimentation influences the vertical redistribution of water vapour in the upper troposphere by dehydrating the altitude of the cirrus clouds and hydrating the air masses via evaporating the crystals in warmer temperatures below [Nedoluha et al., 2002, Rolf et al., 2015].

1.2 Measuring Atmospheric Water Vapour

Observing atmospheric water vapour should be reasonably a simple task, since it is abundant and exhibits absorption features over a broad range of electromagnetic spectrum. However, water vapour measurements proved in practice to be difficult, e.g. water vapour condensates on surfaces which is a challenging issue for in-situ techniques. Also the sharp vertical gradients around the tropopause and the low stratospheric mixing ratios of a few parts per million volume (ppmv) in contrast to the moist tropospheric air masses, present not only difficulties for remote sensing techniques. Furthermore, the analysis of remote sensing measurements is still complicated, since the fundamental physics behind the observed spectrum is not sufficiently well-known [Kley et al., 2000].

Müller et al. [2016] recently reviewed the current measurement techniques of atmospheric water vapour, which improve the knowledge about upper tropospheric and lower stratospheric (UTLS) water vapour distribution. There they conclude, that there is a need for an international programme to accurately characterise long-term and global changes in UTLS water vapour. Even though the high-resolution infrared radiation sounder (HIRS) instruments estimating the UTLS water vapour concentrations aboard National Oceanic and Atmospheric Administration (NOAA) operational satellites since 1978 [e.g. Shi and Bates, 2011]. As limitations of the single remote sensing data sets, they mention the poor vertical resolution and the relatively short lifetimes of several years of the nadir-looking sensors on satellites, as well as the high occurrence of short overlaps between different instruments. The only way to gain a long-term data set is to construct a merged data set of different types of HIRS instruments. This requires in advance a reducing of the inter-satellite biases either by in-situ calibration or by models' water vapour which is used as a transfer function between the data sets and short overlap periods [Hegglin et al., 2014]. Additional support in the amount

[1] The water vapour saturation pressure e_s follows the Goff and Gratch [1946] formulation of saturation water vapour pressure over a plane surface of pure water or ice, which was recommended by the World Meteorological Organization [WMO, 1957] and adapted to the international temperature scale 1990 (ITS-90) by Sonntag [1994].

and expansion of overlap in the measurements is provided by the microwave radiometer SAPHIR on board the Megha-Tropiques satellite since October 2011 [Brogniez et al., 2015].

Compared to the remote sensing instruments, the advantage of most in-situ techniques is their higher precision and spatial resolution, which makes them well suited for case studies on smaller scales. Most prominent in-situ measurements are balloon soundings for research applications and specially equipped research aircraft, although their primary goal is not to provide a global data set. The operational international network of weather balloons has been in operation since the 1940s but do not provide reliable measurements at pressures less than 400 hPa for detecting trends and variability in upper tropospheric and lower stratospheric water vapour. Number of studies have demonstrated a clear dry bias in the upper troposphere with this platform as a result of the very poor sensor response at low temperatures, pressures and water vapour concentrations [Dee et al., 2011, Elliot and Gaffen, 1991, Gaffen, 1993, Seidel et al., 2009].

Combining individual campaign data sets of high quality water vapour in-situ measurements in the UTLS is a valuable resource for investigations on trends and variability of water vapour [e.g. Krämer et al., 2009, Meyer et al., 2015, Rosenlof et al., 2001]. However, the spatial coverage of such measurements, the duration of such campaigns as well as the changing composition of measurement devices are making global scaled studies on seasonal and inter-annual variability of UTLS water vapour difficult.

The 2000 Assessment of Upper Tropospheric and Stratospheric Water Vapor (SPARC, Kley et al. [2000]) is the first comprehensive assessment of water vapour observations. It includes intercomparisons of the different water vapour instrumentations that show discrepancies in the critical UTLS concerning range of less than 10 ppmv. Since the SPARC report, disagreements in the results have remained between key data sets [e.g. Rollins et al., 2014, Vömel et al., 2007]. These persistent, systematic discrepancies between atmospheric water vapour measurement techniques under controlled laboratory conditions are in the order of 10% for 10 to 150 ppmv of water vapour and about 20% for UTLS water vapour mixing ratios (below 10 ppmv) [Fahey et al., 2014], which increases the uncertainty for many other follow-up applications such as radiation calculations and cloud formation studies.

1.3 Introduction of the MOZAIC and IAGOS Programmes

In 1994, the European research programme MOZAIC (Measurement of OZone and water on Airbus In-service airCraft) was initiated to respond to the increasing requests for long-term, routine, in-situ observational data of the upper troposphere and lower stratosphere (UTLS) with much greater spatial coverage, by using commercial passenger aircraft as measurement platforms [Marenco et al., 1998, Müller et al., 2016, Petzold et al., 2015]. The in-service aircraft are equipped with small, compact and light-weight scientific instruments for measuring atmospheric trace constituents on a daily basis. Since commercial aviation operates in the altitude band of 9 - 13 km, it is a very cost-efficient platform [Eyre and Reid, 2014], particularly for in-situ probing of the extratropical UTLS and thus complements the existing global observing network of space-borne and ground-based observations. Through the use of different commercial aircraft, the data are randomly selected with a good occupancy so that a statistically reliable and representative data set for

the UTLS is achieved [Alteköster, 2014]. The main element of MOZAIC in the beginning was to collect data on ozone (O_3), water vapour and temperature in the atmosphere. After the first experiences and a phase of development, the measurements were extended to carbon monoxide (CO) and nitrogen oxides (NO_y) in 2001 [Nédélec et al., 2015, Petzold et al., 2015].

In 2008, the research projects MOZAIC and CARIBIC (Civil Aircraft for the Regular Investigation of the Atmosphere Based on an Instrument Container) were merged into the European Research Infrastructure IAGOS which now serves as a single infrastructure designed for sustainable long-term and global operation [Volz-Thomas et al., 2009]. IAGOS-CARIBIC is a measurement programme similar to MOZAIC but with a more sophisticated instruments equipped container which investigates approx. four flights a month the atmosphere with only a single but extensively equipped cargo container aboard of commercial aircraft to monitor a wide set of parameters [Brenninkmeijer et al., 1999, Petzold et al., 2015]. The IAGOS-CORE component which displaces the MOZAIC part, comprises the implementation and operation of autonomous instruments installed on long-range aircraft of internationally operating airlines for continuous, global-scale and daily measurements of reactive gases and long-lived greenhouse gases (e.g. CO, CO_2, CH_4 and water vapour), important chemically active trace gases (e.g. O_3), as well as aerosol, dust and cloud particles [amongst others, Bundke et al., 2015, Filges et al., 2015]. The instruments are designed for fully automated operation aboard the aircraft in unattended mode for several weeks. The fully equipped IAGOS-CORE instrument rack weight is 100 kg and is mounted in the avionics bay of Airbus A340/A330 aircraft. The collected data are transmitted automatically to the IAGOS data centre with open data policy (GEO/GEOSS) [Petzold et al., 2015].

The main partners of IAGOS are Forschungszentrum Jülich GmbH (FZJ, Germany), Centre National de la Recherche Scientifique (CNRS, France), Max-Planck Gesellschaft zur Förderung der Wissenschaften e.V. (MPG, Germany), Karslruher Institut für Technologie (KIT, Germany), Deutsches Zentrum für Luft- und Raumfahrt (DLR, Germany), Leipniz-Institut für Troposphärenforschung e.V. (TROPOS, Germany), Meteo France (MF, France), and University of Manchester (Univ. MAN, UK).

One of the keys to the success of IAGOS is the participation of airlines which cover the operational costs of including instruments in the aircraft payload. Currently, Deutsche Lufthansa (DLH), Air-France (AFR), China Airlines (CAL), Cathay Pacific Airways (CPA), Iberia (IBE) and Hawaiian Airlines (HAL) support the research infrastructure.

1.4 Data Description

At the beginning of April 2017, the IAGOS-CORE fleet consisted of three Airbus A340-300 and five Airbus A330-300 aircraft. Each aircraft conducts on average 500 flights per year and the entire MOZAIC and IAGOS fleet has visited almost 200 airports since the beginning of the programme. Figure 1.3 illustrates the number of aircraft and number of flights conducted per year for MOZAIC and then IAGOS-CORE, which are quality controlled and available for analysis on the official IAGOS webpage (www.iagos.org).

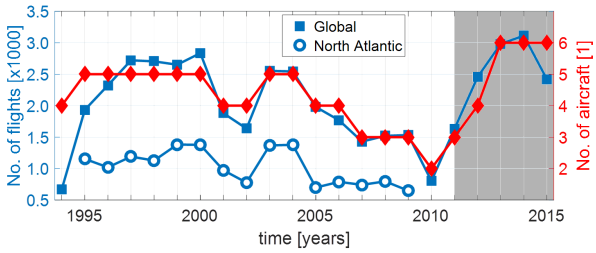

Figure 1.3: Time series of passed flights (blue line) and participating aircraft (red line). The blue squares represent the passed flights distributed over the globe for the complete time period, where as the blue circles represent the passed flights over the North Atlantic flight corridor in the time period 1995 to 2009. The MOZAIC programme took place from 1994 until 2011 and was continued with its successor IAGOS-CORE (grey background).

More than 51600 flights have been carried out since August 1994 (as at 10 April 2017). This includes data from the MOZAIC project (38494 flights from August 1994 to December 2014) and data from more than 13100 IAGOS-CORE flights since July 2011. A subset covering the North Atlantic flight corridor (40 - 60°N, 5 - 65°W) contains 15423 flights in the time period 1995 to 2009 with at least 650 flights every year. This large amount of flights ensures a long-term and global scale of coverage which is represented with the fractional horizontal distribution of the MOZAIC flights in Figure 1.4; however, the global data distribution is not uniform in every region. It is obvious that the highest concentration of data above 280 hPa, the so-called cruising altitude of long-haul passenger aircraft, is between Europe and the East Coast of North

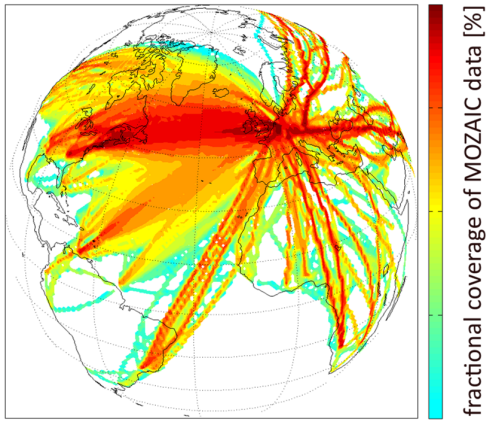

Figure 1.4: Fractional horizontal distribution of MOZAIC flights during the period of 1995 to 2009.

America. In addition, the different flight behaviour over maritime and continental area becomes obvious, i.e. flight tracks above the continental area seem to be strongly restricted whereas the flight tracks over maritime area are non-restricted. Flight tracks over the Pacific Ocean are covered with the introduction of China Airlines to IAGOS in June 2012 and Hawaiian Airlines in Spring 2017.

The on board recording of the data is completely automated by the equipped aircraft. While the aircraft is landed, the raw data of each flight is collected on board of the respective aircraft and send immediately to the data base in Toulouse. The unprocessed data first undergo automated validation procedures before being submitted into the data base (see Figure 1.5). Untouched raw data (L0A) are further automatically analysed using existing pre-flight or in-flight calibration information (L0B). For operational users such as climate monitoring services, the data are available as near real-time (NRT) data within 12 hours. When the prechecked data are validated by the responsible Principle Investigator (PI) of the instrument, they become available as preliminary data (L1). Flight data become final data (L2), when the instrument is removed from the aircraft and the post-flight calibration is conducted in the responsible laboratory by the PI.

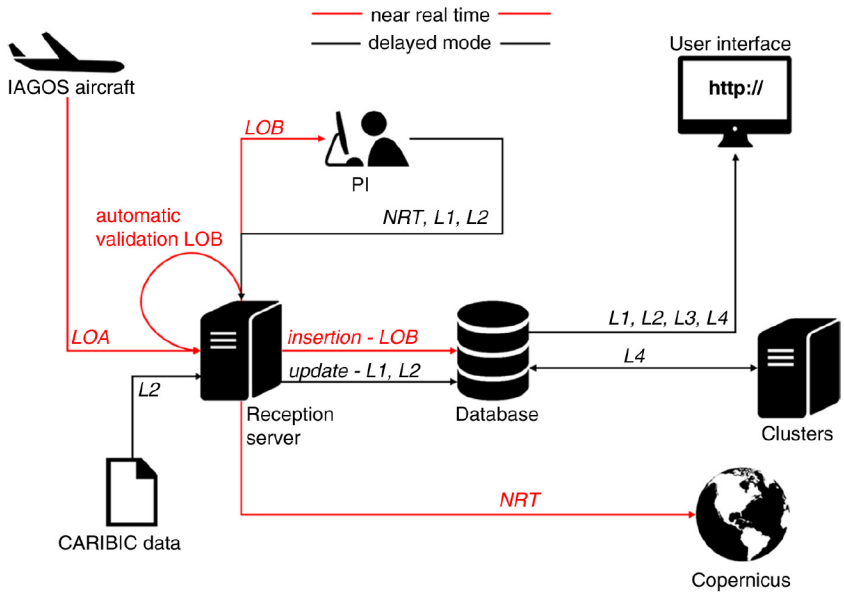

Figure 1.5: Data processing path from the aircraft raw state to the user available state. Data levels refer to raw data (L0A), to automatically analysed data using pre-flight or in-flight calibrations (L0B), to data validated by the responsible PI and published as preliminary data (L1) and to final data (L2) after removal of instrument from the aircraft and post-flight calibration. Climatological data (L3) and added-value products (L4) are also available, whereas near real-time (NRT) data are made available for data assimilation and model evaluation (Adapted from Petzold et al. [2015]).

These final data are used to calculate climatological data (L3) and added-value products (L4). Typically, final data are available to end users through the official web interface within a maximum of 6 months after flight, depending on the instruments operation period. A summary of the MOZAIC/IAGOS data levels and their respective description is provided in Table 1.1.

Table 1.1: Used data levels in the MOZAIC/IAGOS-CORE system.

Level	**Description**
L0A	Raw data
L0B	Automatically validated data
NRT	NRT for Copernicus use, bad data removed
L1	Data validated by PI (preliminary data)
L2	Calibrated data (final data)
L3	Averaged data and climatologies
L4	Added-value products

The content of the data base consists of a variety of in-situ measured atmospheric chemical and physical observations conducted by MOZAIC, IAGOS-CORE and IAGOS-CARIBIC instruments. A subset of these data is used in this work and described in Table 1.2. In addition to these measurements, the location of the observations and the meteorological parameters measured by the aircraft are stored.

Table 1.2: Used parameters on cruise altitude provided by the MOZAIC/IAGOS-CORE system.

Names	**Method**	**Time resolution**	**Uncertainty**	**Reference**
Water vapour	Capacitive hygrometer	5-300 s	$\pm$5% RH	Chapter 2 and 3
Temperature	Resistance thermometer	4 s	$\pm$0.5 K	Helten et al. [1998]
Ozone (O_3)	UV absorption	4 s	$\pm$2 ppbv	Nédélec et al. [2015]
Cloud particles	Backscatter cloud probe	4 s	20%	Beswick et al. [2015]

Also parameters available for cruise altitude provided by the A340/A330 aircraft system are stored in the data base, whereas a subset, which is summarised in Table 1.3, is used in this work in different applications. In principle, the flights are stored on the data base as continuous time series, i.e. the observations are provided at 4 s intervals along the flight track from take-off until landing, but it is also possible to download profile data, i.e. separated files for just ascent or descent parts [Petzold et al., 2015].

The quality assurance and quality control procedures will be briefly introduced by the performed steps in Jülich, where the MOZAIC and IAGOS water vapour and temperature devices undergo a quasi-automatic calibration and processing routine with which a homogeneous high level data set is ensured for the entire programme period. The cycle during an installation period of each capacitive hygrometer and resistance thermometer unit starts with a general hardware and communication check. After successfully passing this

Table 1.3: Used parameters on cruise altitude provided by the A340/A330 aircraft system.

Names	**Units**	**Precision**
UTC time	seconds since take off	4 s
Latitude	deg.	0.01
Longitude	deg.	0.01
Air pressure	hPa	10
Total air temperature	°C	0.25
Static air temperature	°C	0.25
Aircraft air speed	m s^{-1}	0.01

check, up to three devices can be calibrated in the environmental simulation facility at the Forschungszentrum in Jülich [Smit et al., 2000].

This facility enables the control of pressure, temperature, and water concentration. Under realistic atmospheric conditions the airborne water vapour sensing devices can be compared to accurate reference instruments, i.e. a dew point hygrometer for lower/middle tropospheric water vapour conditions and a Lyman-α fluorescence hygrometer for middle/upper tropospheric conditions. The entire simulation process is computer controlled to provide reproducible conditions, and a suite of measured parameters are stored for the follow-up quasi-automatic calibration analysis to calculate the temperature-dependent sensor calibration coefficients (for more details see Chapter 2.2 and Helten et al. [1998]). Unfortunately, a coding update in the calibration analysis procedure from year 2000 on created an error, which yielded in too high humidity values [Lamquin et al., 2012]. To fix this issue, an in-depth reanalysis of the calibration data identified a wrong assignment of two different temperatures and by applying the corrected calibration procedure, the full data set for 2000-2009 was reanalysed [Smit et al., 2014].

The sensors operation cycle continuous with 1-2 month in operation aboard the in-service aircraft, before the instrument is then changed and the operated sensor is again calibrated in the simulation facility to document its post-flight condition. Followed by the cleaning of the sensor, the routine procedures start again with the general communication check and the pre-flight calibration.

Since the MOZAIC and IAGOS devices are installed and operated aboard in-service aircraft, maintenance of the measurement instruments is severely restricted. Thus, a timely and automated processing of the flight data is of significant role for near real-time monitoring of the sensors condition. With the aid of this automatic quality control procedures, such as range checks, spike detection or humidity specific tests of physical feasibility by using the known pre-flight calibration coefficients, the PI is able to detect possible inconsistencies and to further initiate necessary sensor changes.

A slight deviation from the original operation cycle was observed at the beginning of the IAGOS programme. There, humidity sensors were partially operated significantly longer than the planned exchange after two months, a baseline shift in the sensors offset was observed. The humidity measurements have

been corrected with a modified In-Flight Calibration (IFC) method based on the method developed by Smit et al. [2008].

Therefore, raw voltage data of 15 consecutive flights is plotted analogues to Smit et al. [2008] in Figure 1.6 as a function of the sensor temperature. The resulting lower voltage envelope, which include very dry conditions in, e.g. flight sequences in the stratosphere or in descending air masses over the subtropical oceans, is further compared to the lower envelope of the ICH calibration data at the typical lowermost stratospheric background water vapour mixing ratio of 5 ppmv H_2O VMR [Kley et al., 2007, Nedoluha et al., 2007] for cruise altitude (ambient pressure = 230 hPa).

The resulting gap is then identified as sensor offset ΔU_D and corrected. Effects of the applied IFC method on the humidity distribution are shown with a comparison between MOZAIC and IAGOS humidity distributions in Chapter 6.3.

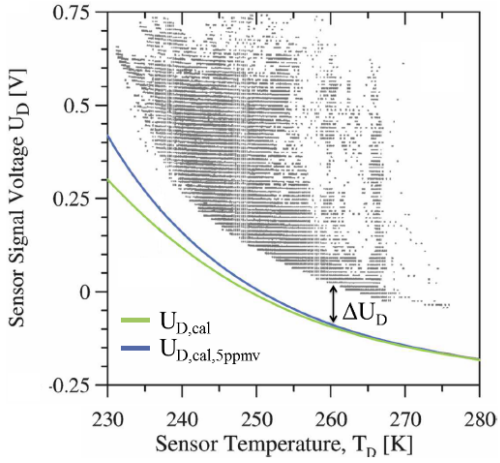

Figure 1.6: Raw signal (U_D) of capacitive humidity sensor aboard MOZAIC and IAGOS aircraft as a function of sensor temperature (T_D) obtained at cruise altitude (ambient pressure = 230 hPa). Green line: zero signal for calibrated sensor; blue line: superposition of zero signal and the contribution by 5 ppmv water vapour. The difference voltage between the blue line and the lower voltage envelope defines the sensor offset ΔU_D (Adapted from Smit et al. [2008]).

1.5 Objectives

Within the framework of this thesis, a broad spectrum of objectives have to be worked on. This includes technical aspects, such as the question about the general and especially the performance inside of ice clouds of the MOZAIC capacitive hygrometer (Chapter 2). The question, if the improved IAGOS capacitive hygrometer can confirm the performance and data quality of the former hygrometer is answered in Chapter 3.

With the development of an automatic calibration analysis routine, as well as the development of an automatic flight data analysis routine based on the existing manual routines, a homogeneous and traceable data set for the first scientific analysis of 15 years of MOZAIC is provided.

This analysis includes the question about the determination of water vapour background climatologies and possible trend analysis of observed humidity in the tropopause region over the North Atlantic in a high spatial and temporal resolution (Chapter 4). Chapter 5 studies the question about possible identification of stratosphere-troposphere exchange processes and their related transport pathways, whereas Chapter 6 is separated into two parts. The first one deals with the question about understanding the distribution and occurrence of ice supersaturated regions in the upper troposphere and lower stratosphere above the North Atlantic because of its close link to cirrus formation and lifecycle. Moreover, the second one uses the new IAGOS data set in a case study which includes the new cloud index measurements and studies the connection of ice supersaturation and cirrus cloud formation for different global regions.

CHAPTER 2

EVALUATION OF THE MOZAIC CAPACITIVE HYGROMETER DURING THE AIRBORNE FIELD STUDY CIRRUS-III

P. Neis[1,3], H. G. J. Smit[1], M. Krämer[2], N. Spelten[2], and A. Petzold[1]

[1]Forschungszentrum Jülich GmbH, IEK-8 Troposphäre, Jülich, Germany

[2]Forschungszentrum Jülich GmbH, IEK-7 Stratosphäre, Jülich, Germany

[3]Johannes Gutenberg Universität Mainz, Institut für Physik der Atmosphäre, Mainz, Germany

This Chapter is based on the manuscript "Evaluation of the MOZAIC Capacitive Hygrometer during the airborne field study CIRRUS-III" by P. Neis, H. G. J. Smit, M. Krämer, N. Spelten, and A. Petzold, published in Atmospheric Measurement Techniques as Neis et al. [2015a].

Summary. The MOZAIC Capacitive Hygrometer (MCH) is usually operated aboard passenger aircraft in the framework of MOZAIC (Measurement of Ozone by Airbus In-Service Aircraft) for measuring atmospheric relative humidity (RH). In order to evaluate the performance of the MCH, the instrument was operated aboard a Learjet 35A research aircraft as part of the CIRRUS-III field study together with a closed-cell Lyman-α fluorescence hygrometer (Fast in-situ Stratospheric Hygrometer, or FISH) and an open-path tunable diode laser system (Open-path Jülich Stratospheric TDL ExpeRiment, or OJSTER) for water vapour measurement. After reducing the CIRRUS-III data set to data corresponding to MOZAIC aircraft operation conditions, the 1 Hz RH data cross correlation between the MCH and reference instruments FISH (clear sky) and OJSTER (in-cirrus) yielded a remarkably good agreement of $R^2 = 0.92$ and slope $m = 1.02$ and provided a MCH uncertainty of 5 % RH. Probability distribution functions of RH deduced from the MCH and reference instruments agreed well between 10 and 70 % RH with respect to liquid water in the ambient temperature range of ca. -70 to -40 °C. The use of MCH data is limited to sensor temperatures above the calibration limit of $T_{\mathrm{sensor}} =$ -40 °C (corresponds to ambient temperature of $T_{\mathrm{ambient}} =$ -70 °C at typical

cruising speed of long-haul passenger aircraft). Good performance of the MCH for clear sky as well as for in-cirrus conditions demonstrated the sensor robustness also for operation inside ice clouds.

2.1 Introduction

Water vapour is one of the most important variables for weather prediction and climate research. Particularly, the interaction between the water vapour in the UTLS (upper troposphere and lowermost stratosphere) and tropopause dynamics is not well understood. Thus, in the latest IPCC report [IPCC, 2013], it is stated that the knowledge about potential trends and climate feedback mechanisms of upper tropospheric water vapour is low because of the lack of long data records of high quality in this specific region of the global atmosphere. Neither the global radiosondes network nor satellites can provide measurements of the required spatial and temporal resolution, while the regular in-situ measurement of upper tropospheric humidity (UTH) is still difficult.

Since 1994, the European research programme MOZAIC [Measurement of OZone and water on Airbus In-service airCraft; Marenco et al., 1998] and its successor IAGOS [In-service Aircraft for a Global Observing System; Petzold et al., 2013] provide regular data for relative humidity (RH) and other meteorological quantities like temperature and pressure as well as data on atmospheric composition (e.g. ozone and CO) with high spatial and temporal resolution on a global scale. The long-term observations are obtained by in-situ measurements aboard civil passenger aircraft using the existing infrastructure of the international air transport system. However, the continuous high-quality in-situ measurements are restricted to the major global flight routes and to the cruising altitude band of 9 - 13 km, i.e. the observations refer to a large extent to the UTLS region. Relative humidity data from the MOZAIC programme have been used for various climatological studies including the distribution of UTH [Kley et al., 2007, Luo et al., 2007, 2008], the distribution of RH with respect to ice [RH_{ice}, e.g. Gierens et al., 1997, 1999] and ice supersaturation regions [e.g. Gierens et al., 2000, Spichtinger et al., 2003a] in the upper troposphere.

Atmospheric RH is measured in the MOZAIC/IAGOS programme through a compact airborne humidity sensing device using capacitive sensors (MOZAIC Capacitive Hygrometer: MCH). The sensor itself and the applied calibration techniques are described in detail by Helten et al. [1998]. First validation studies from formation flights of a MOZAIC aircraft and a research aircraft are reported by Helten et al. [1999], while Smit et al. [2008] presents an approach for a potential in-flight calibration of MCH. A reanalysis of the global MOZAIC RH data set for the period 2000 - 2009 was performed recently [Smit et al., 2014].

In order to assess the validity of the long-term water vapour data and its limitations, Helten et al. [1999] provided an in-flight comparison of MOZAIC and POLINAT [Schlager et al., 1997, Schumann, 1997] water vapour measurements. However, this formation flight intercomparison was difficult to analyse because the twin-engine research aircraft Falcon 20 had to follow the MOZAIC Airbus A340 - 300 with changing time lags and distances whereby sampling of identical air masses can not always be ensured. In 2006, there was the opportunity to participate in the aircraft campaign CIRRUS-III along with high precision research-grade instruments for measuring the water vapour volume mixing ratio (VMR). The in-flight single-platform mea-

surements permitted a blind intercomparison of the MCH with high performance water vapour instruments by measuring the same air masses and under different atmospheric conditions. A similar analysis of the improved IAGOS Capacitive Hygrometer is in preparation and will be published elsewhere.

2.2 MOZAIC Capacitive Hygrometer

A detailed description of the MOZAIC Capacitive Hygrometer is given by Helten et al. [1998], Helten et al. [1999] and Smit et al. [2014]. In the following, we summarise the original descriptions.

The compact airborne MCH consists of a capacitive sensor (HUMICAP® of type H, Vaisala, Finland) whose capacitance depends on the relative humidity of the dielectric layer of the condenser and a platinum resistance sensor (Pt100) for the direct measurement of the temperature at the humidity sensing surface. The basic measurement process is based on the diffusion-limited adsorption of the H_2O-molecules by the dielectric membrane of the sensor. Since diffusion is strongly temperature-dependent, the sensor response slows down with decreasing temperatures. Figure 2.1 shows how both sensors are mounted in the used air sampling housing [Model 102 BX, Rosemount Inc.; see Stickney et al., 1990]. The relative humidity and temperature signals are fed into a microprocessor-controlled transmitter unit (HMP230, Vaisala) which passes the signals to the data acquisition system. The data conversion from capacitance signals to relative humidity values is performed off-line in a separate data quality assurance and analysis step.

In its original MOZAIC mounting position aboard an Airbus A340 the sensor housing is placed approx. 7 m downstream of the aircraft nose on the left side with a 7 cm distance from the aircraft skin to avoid possible contaminating interferences of the aircraft skin. Inside the Rosemount housing the air flow is separated into the main flow, which traverses straight through the housing and the minor flow, which follows a sharp right angle into a smaller channel where the sensors are placed. The housing is equipped with small holes in the side wall to neglect internal boundary layer effects by sucking off the internal boundary layer air through the holes. The right angle of the minor flow protects the RH- and T-sensors against dust, water, and particles.

Due to the strong speed reduction in the inlet part of the housing, the sampled air flow is significantly heated through adiabatic heating. Assuming 100% conversion of kinetic energy into heat during flow deceleration, the ambient temperature $\mathrm{T_{ambient}}$ (Static Air Temperature SAT) increases to the temperature at the sensor inside the housing, i.e. the sensor temperature $\mathrm{T_{sensor}}$ (Total Air Temperature TAT). The fact that the adiabatic conversion of energy is not exactly 100%, the latter quantity $\mathrm{T_{sensor}}$ is calculated from the actually measured sensor temperature, i.e. the typically 0.1 - 1.0 K colder recovery temperature (Total Recovery Temperature TRT), and the so-called recovery factor. This aircraft speed depending and empirically determined factor is provided by the housing manufacturer.

The relationship between ambient temperature $\mathrm{T_{ambient}}$ and sensor temperature $\mathrm{T_{sensor}}$ is a function of the aircraft speed, i.e. its Mach-number M:

$$\mathrm{T_{sensor}} = \mathrm{T_{ambient}} \cdot \left(1 + \left(\frac{c_p - c_v}{2c_v}\right) \cdot \mathrm{M}^2\right), \tag{2.1}$$

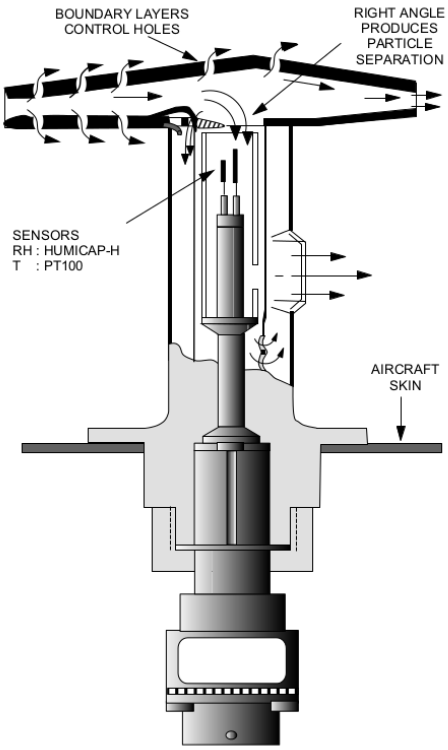

Figure 2.1: Cross section of the airborne capacitive sensing element. Right angle protects against particles and control holes in the side wall minimise internal boundary layer effects [Helten et al., 1998].

where $c_p (= 1005\,\mathrm{Jkg^{-1}K^{-1}})$ and $c_v (= 717\,\mathrm{Jkg^{-1}K^{-1}})$ are the specific heat of dry air at constant pressure and volume, respectively. The resulting difference between T_{sensor} and $T_{ambient}$ at 10-12 km cruising altitude for different Mach-numbers is displayed in Figure 2.2: for the MOZAIC-typical aircraft speed of Mach-number M = 0.81 the adiabatic heating effect is approx. 30 K. $T_{ambient}$ is derived from Eq. (2.1) with an uncertainty of less than $\pm$0.5 K resulting from uncertainties in T_{sensor} ($\pm$0.25 K) and M. Because of the strong temperature increase, the detected dynamic relative humidity $RH_{dynamic}$ is significantly lower than the static relative humidity RH_{static} of the ambient air at $T_{ambient}$:

$$RH_{static} = RH_{dynamic} \cdot \left(\frac{T_{ambient}}{T_{sensor}} \right)^{\frac{c_p}{c_p - c_v}} \cdot \frac{e_{s,liquid}\,(T_{sensor})}{e_{s,liquid}\,(T_{ambient})}, \tag{2.2}$$

where $e_{s,liquid}$ is the water vapour saturation pressure over liquid water at T_{sensor} and $T_{ambient}$, respectively. The water vapour saturation pressure over liquid water $e_{s,liquid}$ follows the Goff and Gratch [1946]

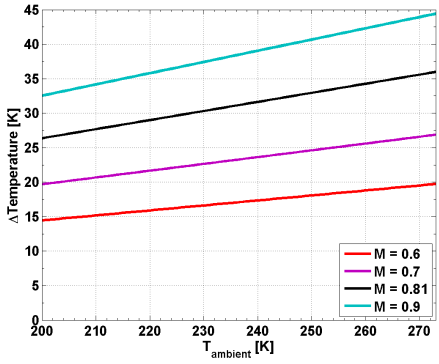

Figure 2.2: Sampled air flow is heated through adiabatic heating effects when entering the inlet. ΔTemperature describes the increase relative to the ambient temperature $T_{ambient}$ [Static Air Temperature SAT; see Helten et al., 1998] for several aircraft speeds, i.e. the Mach-number M, by assuming 100% conversion of kinetic energy to heat during flow deceleration.

formulation of saturation water vapour pressure over a plane surface of pure water or ice, which was recommended by the World Meteorological Organization [WMO, 1957] and adapted to the international temperature scale 1990 (ITS-90) by Sonntag [1994]. For fast high-flying aircraft the relation $RH_{static}/RH_{dynamic}$ reaches a factor of approx. 13, which leads to the fact, that the RH sensor operates in the lowest 10% of its full dynamic range. Since the sensor is operating in the lower part of its full dynamic range, an individual calibration of each sensor is necessary, which is accomplished in the atmospheric simulation chamber at Jülich [Smit et al., 2000] before installation on the aircraft and after detachment past 500 hours of flight, which corresponds to about 4 - 6 weeks between installation and deinstallation. These calibrations are made over a sensor temperature range between -40°C and +20°C against (i) Lyman-α fluorescence hygrometer [Kley and Stone, 1978] at water vapour mixing ratios below 1000 ppmv [relative accuracy $\pm$4%, Helten et al., 1998] and (ii) dew/frost point hygrometer (General Eastern, Type D1311R) at water vapour mixing ratios above 1000 ppmv with an accuracy of $\pm$0.5 K. The relative humidity of a calibrated sensor (RH_C) at constant temperature T is found to be linearly related to the uncorrected output value (RH_{UC}) provided by the HMP230 transmitter unit.

$$RH_C(T) = a(T) + b(T) \cdot RH_{UC}(T) \tag{2.3}$$

In Section 2.3.2 the calibration procedure of the MCH is described, which was used during the CIRRUS-III field study. It combines the standard procedure based on Helten et al. [1998] and the in-flight calibration described by Smit et al. [2008].

Evaluation of 9 years of pre- and post-flight calibrations in MOZAIC has shown that the offset $a(\mathrm{T})$ is the most critical parameter in determining the uncertainty of the measurements with a shift of about -5% RH, while the sensitivity (slope) $b(\mathrm{T})$ is less critical and only changes by about -2%.

2.3 Experimental Section

2.3.1 The CIRRUS-III Field Campaign

To extend the performance assessment of the MCH from the formation flight intercomparison [Helten et al., 1999], the sensor was operated aboard a twin-engine business-jet aircraft of type Learjet 35A as part of the CIRRUS-III field study, which was coordinated by Forschungszentrum Jülich.

Figure 2.3: CIRRUS-III flight track overview (Map Data © 2008 Google, Sanborn)

The overarching goals of CIRRUS-III were to understand the formation mechanism of cirrus clouds in different background conditions, their radiative effects and the microphysical properties of the cirrus cloud particles. In total 6 flights were conducted in the period between 23 and 29 November 2006 at mid-latitudes (45°N - 70°N, see Figure 2.3) and at flight altitudes between 7 and 12 km. These flights in the UTLS were launched from the Hohn Air Base in Northern Germany with the Learjet 35A operated by *enviscope* GmbH.

For the sensor intercomparison studies CIRRUS-III provided 4 flights (see Table 2.1). The dataset consists of approx. 13 flight hours in air masses colder than -40°C at cruise altitude, approx. 4 flight hours in cirrus clouds and 9 flight hours out of clouds. Furthermore, stratospherically influenced air masses have been sampled for 19 minutes with ozone VMR above 125 ppmv measured by the dual-beam UV-absorption ozone photometer JOE (Jülich Ozone Experiment) instrument [Mottaghy, 2001]. Two flights had to be discarded due to inlet heating problems at the reference instrument FISH. An overview of the individual flights is provided in Table 2.1.

Table 2.1: CIRRUS-III flight overview at cruise altitude. Air masses are divided into "troposphere" and "stratosphere" with the ozone VMR threshold of 125 ppmv.

Flight No.	Date	Take-off / Landing (UTC)	Temperature Range	H_2O VMR Range	In / out of Cirrus	Stratosphere / Troposphere
1	24. Nov.	10:47 / 14:53	-62.6 - -52.8°C	24 - 107 ppmv	95 / 96 min	2 / 190 min
2	28. Nov.	08:22 / 12:07	-62.4 - -44.1°C	17 - 138 ppmv	4 / 160 min	11 / 153 min
3	28. Nov.	13:31 / 17:25	-60.0 - -42.4°C	27 - 360 ppmv	56 / 124 min	5 / 175 min
4	29. Nov.	09:16 / 13:51	-61.2 - -45.8°C	16 - 216 ppmv	62 / 158 min	2 / 218 min
All			-62.6 - -42.4°C	16 - 360 ppmv	217 / 537 min	19 / 735 min

2.3.2 Instrumentation

During the CIRRUS-III field campaign, high precision research-grade instruments were operated on board of the aircraft to characterize the air masses probed during flight patterns in frontal cirrus clouds. An important part of the instrumentation was dedicated to the measurement of gas phase and total water. The instrumentation included a MCH and an open path tunable diode laser system [OJSTER; MayComm Instruments, Krämer et al., 2009, May and Webster, 1993] to measure gas phase water vapour VMR. Simultaneously, total water VMR (= gas phase plus ice water) was measured by the reference measurement instrument FISH [Fast In-Situ Hygrometer, Zöger et al., 1999]. The closed-cell Lyman-α fluorescence hygrometer was equipped with a forward facing inlet to sample gas phase water in clear sky and total water inside cirrus clouds. To determine whether a data point is in a cirrus cloud or not, the ratio of RH_{ice} from FISH (total water) and OJSTER (water vapour) was used [see Krämer et al., 2009]. FISH was calibrated using a laboratory calibration facility with the capability to simulate realistic atmospheric conditions, i.e. water

Table 2.2: Instruments and parameters used during CIRRUS-III field campaign.

Instrument	Detection Quantity	Measurement Technique	Response Time	Uncertainty	Reference
FISH	VMR [ppmv]	Lyman-α fluorescence hygrometer	1 s	7%±0.3 ppmv (precision 1%)	(1)
OJSTER	VMR [ppmv]	Open path TDL	1 s	10-15%	(2)
MCH	RH_{liquid} [% RH]	Capacitive sensor	LT: 1 s, UT: 10 s LS: 1 min	±(4-7)% @10-13 km below 10 km ±(4-6)%	(3)

FISH: Fast in-situ Stratospheric Hygrometer; OJSTER: Open path Jülich Stratospheric Tdl ExpeRiment; MCH: MOZAIC Capacitive Hygrometer; LT: lower troposphere; UT: upper troposphere; LS: lower stratosphere; For further information see Bange et al. [2013]. References: (1) Zöger et al. [1999], (2) May and Webster [1993], (3) Helten et al. [1998]

vapour VMR from several hundred to a few ppmv and pressure from 1000 to 10 hPa. During the calibration water vapour mixing ratio was determined using a commercial dew point hygrometer (MBW DP30). The instruments and the parameters derived from their measurements are listed in Table 2.2.

Prior to the CIRRUS-III campaign the MCH have been (pre-flight) calibrated in the simulation chamber at Forschungszentrum Jülich following the procedures briefly described in Section 2.2. Unfortunately a post-flight calibration was not possible due to sensor failure after deinstallation of the MCH from the Learjet aircraft at the end of the campaign. From long term experiences of MOZAIC pre- and post-flight calibrations it is well known that over the three months period between the pre-flight calibration and the end of the campaign the offset $a(\mathrm{T})$ can change significantly by about 5% RH while the slope $b(\mathrm{T})$ is changing by less than 2% on the relative scale [see Eq. 2.3 and Smit et al., 2014]. In order to determine the potential change of the offset $a(\mathrm{T})$ between pre-flight calibration and the end of the campaign the so called in-flight calibration method [Smit et al., 2008] has been applied.

Thereby, the sensor offset $a(\mathrm{T})$ at lowest relative humidity has been determined from the measurements themselves as obtained during periods when the aircraft is flying in the lower stratosphere, where the water vapour mixing ratio reached well defined minimum values. In our case, the minimum value in stratospherically influenced air masses was about 20 $\pm$ 1 ppmv as measured by the FISH instrument. Its resulting contribution to the $\mathrm{RH_{liquid}}$-signal of the MCH is minimal. Compared to the pre-flight calibration an offset change of 4.5 $\pm$ 1% $\mathrm{RH_{liquid}}$ was found. The $\mathrm{RH_{liquid}}$-flight data of the MCH obtained during CIRRUS-III campaign have been corrected for this offset drift. The resulting overall uncertainty of the RH measurements by the MCH, including contributions from temperature uncertainties, is about $\pm$5% $\mathrm{RH_{liquid}}$ which is in good agreement with mean uncertainty range obtained from long term MOZAIC-measurements [Smit et al., 2014] .

2.4 Results - Assessment of MCH Performance

The instrumentation deployed in CIRRUS-III allows an in-flight intercomparison of all water vapour instruments. Figure 2.4 illustrates an example of the kind of data collected from one research flight on 28 Nov. 2006 (Flight 2). Data from the water vapour sensing instruments used for the intercomparison are shown as VMR. The ambient temperatures $\mathrm{T_{ambient}}$ encountered during the flight ranged from -44.1°C to -62.4°C for relevant measurement altitudes. Respective water vapour VMR covered the range from 17 ppmv at the tropopause to approx. 150 ppmv in the free troposphere and even higher values during ascent from and descent into the airport.

For the instrument intercomparison we analysed the sensors with respect to $\mathrm{RH_{liquid}}$ since this is the parameter the MCH is calibrated against in the sensor temperature range (see Section 2.2). Further, data for water vapour VMR $>$ 1000 ppmv were excluded in this study because the FISH instrument becomes optically opaque and thus insensitive to changes in VMR [Zöger et al., 1999].

In Figure 2.5, we compare VMR data and $\mathrm{RH_{liquid}}$ data from MCH and gas-phase reference, i.e. OJSTER data in cloud, otherwise FISH data for a complete validation of the MCH for Flight 2. Largest

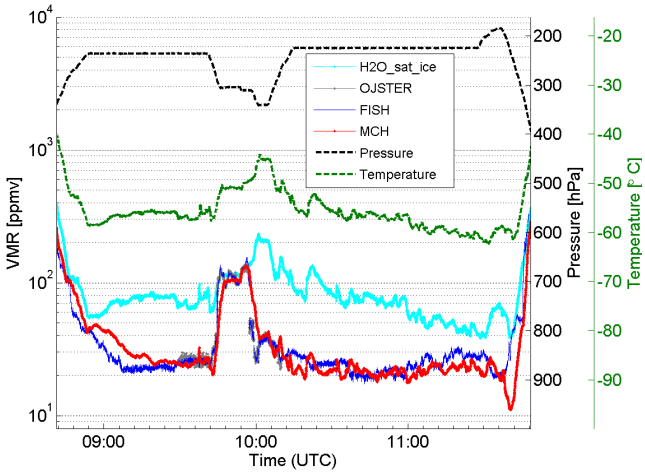

Figure 2.4: Time series of water vapour volume mixing ratios (VMR) from MCH (red), FISH (blue) and OJSTER (grey) during CIRRUS-III flight on 28 Nov. 2006. Ice saturation is shown in cyan, while pressure (black) and ambient air temperature (green) are plotted with dashed lines.

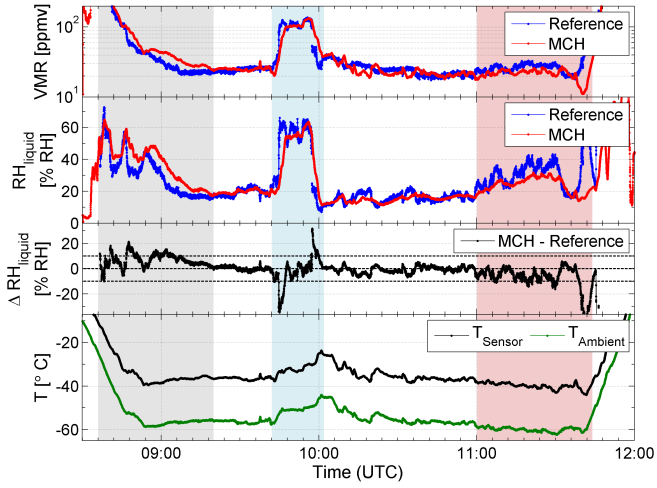

Figure 2.5: Top-down: VMR measured by the MCH (red) and the reference (blue), i.e. FISH (clear sky) and OJSTER (in-cirrus), RH_{liquid} and Δ RH_{liquid} (MCH - reference), as a function of flight time during Flight 2 on 28 Nov 2006. Sensor temperature T_{sensor} (black) as well as ambient temperature $T_{ambient}$ (green) are shown in the bottom panel of the figure. The blue-shaded area represents air masses with high humidity and possible cirrus cloud. Air masses with sensor temperatures at and below the calibration limit are shaded in red. The grey-shaded sequence illustrates the effect of increasing response time during decreasing sensor temperatures.

deviations of the MCH to the reference are found in clear sky air masses for cold conditions with sensor temperature $T_{sensor} < -40°C$ (this corresponds to ambient temperature below approx. -60°C at M = 0.70) and at transition sequences around the cirrus cloud. Except for these extreme conditions, the difference between the MCH and the reference is of the order of 10% RH_{liquid} or less. Given the fact that during CIRRUS-III the MCH was operated at its lower limit of performance, the agreement with the research-grade reference instruments is remarkably good.

An analysis of MCH performance at the limit of its operation range is provided as the example of Flight 2 in Section 2.4.2.

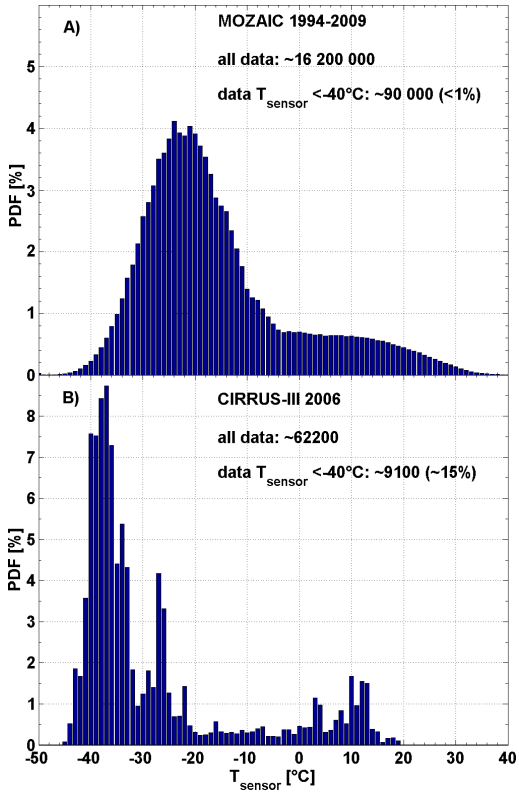

Figure 2.6: Frequency of occurrence for observations of T_{sensor} during approx. 15 years of MOZAIC (A, top panel) and CIRRUS-III (B, bottom panel), respectively.

2.4.1 MCH Performance against Reference Instruments

In order to prepare a data set for evaluation of the MCH performance, we introduce three filter operations to reduce the CIRRUS-III data set to MOZAIC typically operational conditions. First, it has to be noted that regular operation conditions of the MCH aboard long-haul passenger aircraft with a cruising speed of approx. M = 0.81 are characterised by sensor temperatures $T_{sensor} \geq$ -35°C (see Figure 2.6 A), which are within the lower MCH calibration limit of -40°C (see Section 2.2). However, during the operation aboard the slower flying Learjet 35A (cruising speed slower than M = 0.70), sensor temperature T_{sensor} values significantly lower than -40°C were reached (see Figure 2.6 B).

Consequently, data with sensor temperatures $T_{sensor} <$ -40°C were excluded from the analysis. This fact is illustrated in Figure 2.7 showing the difference in RH_{liquid} between MCH and FISH data for clear sky conditions and OJSTER data for in-cirrus conditions, according to sensor temperature T_{sensor}. Furthermore, the maximum ambient temperature $T_{ambient}$ was set to the level of instantaneous freezing of -40°C in order to minimise the perturbation of measurements by erroneously sampled liquid water droplets in warm clouds.

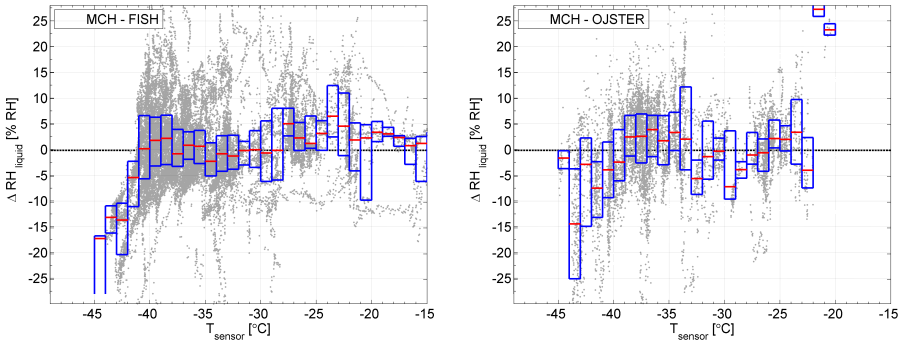

Figure 2.7: Differences in relative humidity RH_{liquid} of MCH and both reference instruments, i.e. FISH (left panel; clear sky) and OJSTER (right panel; in-cirrus), are scattered against the sensor temperature T_{sensor}. A drift towards too dry MCH measurements below the calibration limit of -40°C is clearly seen. The median values (red lines in the box) of the 1°C-binned data as well as the 25^{th} and 75^{th} percentiles are within the calibration limits.

Finally, flight sequences of the Learjet 35A with steep ascents and descents were excluded, since these flight conditions are not comparable to conditions aboard long-haul passenger aircraft. To obtain information about the MCH performance relevant for the MOZAIC data set, i.e. for nearly constant flight levels with moderately slow changes in temperature and humidity, the flight altitude for CIRRUS-III was smoothed over 90 seconds time intervals, and in case altitude changes exceeded $\Delta z > 6$ m in 5 seconds the respective data points were excluded from the intercomparison. These filtering operations lead to a data set

with MOZAIC typically operational conditions with a remaining fraction of about 36% of campaign data (see Table 2.3 for more details).

Table 2.3: Fraction of remaining data after filtering the data set of MOZAIC atypically operational conditions.

Method	**Remaining Data**	**Fraction of Remaining Data**
No filter	62207	100%
$T_{ambient}$ < -40°C	35650	57%
T_{sensor} > -40°C	31331	50%
w/o Ascent/Descent	26234	42%
All	22184	36%

The correlation between MCH and reference RH_{liquid} data and RH_{ice} data from FISH (clear sky) and OJSTER (in-cirrus) is shown in Figure 2.8. The scatter plots for the 1 Hz data sets reduced to MOZAIC-relevant conditions (hereafter referred to as "reduced dataset") show similar scattering around the line of unity. Linear regression analysis confirms this with similar results for both cases: a correlation coefficient of R^2 = 0.92 with a slope of virtually unity. The offset for the RH_{liquid} regression line is 0.18 ± 0.09% RH_{liquid} and for the RH_{ice} regression line 0.36 ± 0.15% RH_{ice}, respectively.

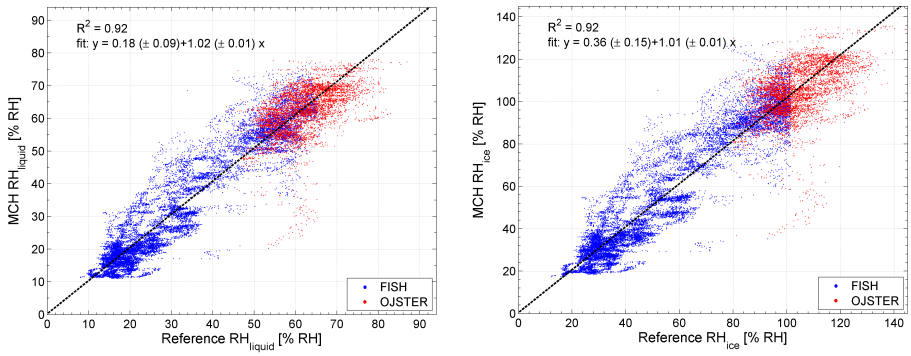

Figure 2.8: Comparison cross plot between reference, i.e. FISH (blue dots; clear sky) and OJSTER (red dots; in-cirrus), and MCH RH_{liquid} (left panel) and RH_{ice} (right panel) displayed as scatter plot with robust fitting curve (dashed line), respectively.

A more statistically based view on the data set is shown in Figure 2.9, where the correlation between the sensors averaged for 5% RH_{liquid} bins is shown. The MCH agrees very well with the reference instruments over the entire range of values measured in the cloud-free atmosphere. Inside cirrus clouds,

i.e. $RH_{liquid} > 65\%$, the sensors deviate as expected as a result of the increased response time of the MCH. Small scale supersaturations are smoothed out, while OJSTER can detect these with response time of approx. 1 s. Linear regression analysis weighted with the number of occurrence provides a correlation coefficient of R^2 = 0.99 with an offset of -0.15 $\pm$ 1.29% RH_{liquid} and a slope of 1.02 $\pm$ 0.03. Median values and almost all of the 25^{th} and 75^{th} percentiles fall within the $\pm 5\%$ RH_{liquid} range around the linear regression line, which confirms the previously determined MCH uncertainty of 5% RH_{liquid} (see also Table 2.4).

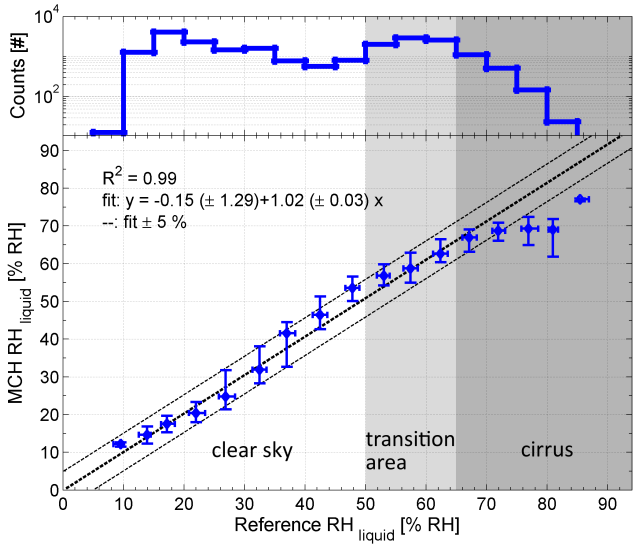

Figure 2.9: Correlation of RH_{liquid} data from MCH and the reference, i.e. FISH (clear sky) and OJSTER (in-cirrus), during CIRRUS-III; the straight line indicates the linear regression line while the dashed lines illustrate the sensor uncertainty range $\pm 5\%$ RH_{liquid}. In the transition area both reference instruments can be used (see Figure 2.8). The top panel shows the number of data points per 5% RH_{liquid} bin.

Table 2.4: Median, $25^{th}/75^{th}$ percentile values and counts of ΔRH_{liquid} (MCH - reference); data were classified into 5% RH_{liquid} bins relating to the reference, i.e. OJSTER data in cloud, otherwise FISH data.

RH bin [%]	0 - 5	5 - 10	10 - 15	15 - 20	20 - 25	25 - 30	30 - 35	35 - 40	40 - 45
ΔRH_{liquid} **[% RH]**	-	$3.0^{+0.2}_{-0.4}$	$1.0^{+1.6}_{-1.1}$	$0.4^{+2.2}_{-2.9}$	$-1.8^{+2.4}_{-2.7}$	$-2.3^{+5.5}_{-2.8}$	$-0.1^{+5.2}_{-4.4}$	$3.7^{+3.4}_{-7.3}$	$3.9^{+4.2}_{-2.9}$
counts [#]	-	13	1276	4037	2335	1471	1606	776	569
RH bin [%]	45 - 50	50 - 55	55 - 60	60 - 65	65 - 70	70 - 75	75 - 80	80 - 85	85 - 90
ΔRH_{liquid} **[% RH]**	$5.4^{+3.5}_{-3.1}$	$4.2^{+2.6}_{-2.9}$	$1.7^{+3.8}_{-4.2}$	$0.4^{+3.7}_{-2.8}$	$-0.8^{+2.7}_{-3.3}$	$-3.3^{+2.9}_{-2.8}$	$7.7^{+3.8}_{-4.0}$	$-12.3^{+3.8}_{-7.1}$	$-8.9^{+0.8}_{-0.8}$
counts [#]	813	2015	2910	2567	1109	512	148	24	3

For a better understanding of an uncertainty of 5% RH_{liquid} Figure 2.10 shows water vapour VMR as a function of temperature for 5% and 10% RH_{liquid} for pressure levels at typical passenger aircraft flight altitudes. As an example, at $T_{ambient} = 215$ K and pressure = 220 hPa a measured $RH_{liquid} = 5\%$ with the uncertainty of 5% RH_{liquid} corresponds to a VMR of approx. 5 ppmv $\pm$ 5 ppmv.

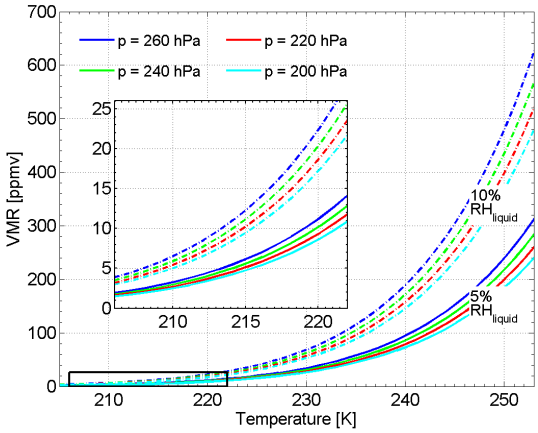

Figure 2.10: Water vapour volume mixing ratios (VMR) as a function of ambient temperature for 5% (solid lines) and 10% RH_{liquid} (dashed lines), respectively. The different pressure levels represent typical passenger aircraft flight altitudes. The inserted box shows a zoom to the lower temperature and VMR values.

The consistency of the MCH RH_{liquid} data is shown in Figure 2.11. The probability distribution function (PDF) for RH_{liquid} derived from MCH data agree very well with those derived from the reference for the entire data set. Larger deviations at higher values of RH_{liquid}, e.g. at cirrus cloud edges reflect the fact of the longer response time of the MCH. The sensor behaviour for those conditions at the limit of the sensor operation specifications is analysed in detail in the following section.

2.4.2 Limits of MCH operation

The comparison between the MCH RH_{liquid} data and the reference RH_{liquid} data, i.e. OJSTER data in cloud, otherwise FISH data, during the CIRRUS-III field study shows a remarkably good agreement for the reduced data set. However, the performance of the MCH sensor in conditions at its limits of operation, e.g. close to the lower calibration limit of T_{sensor} = -40°C or during strong humidity changes has to be analysed in detail in order to assess the sensor's operation range. For this purpose, the time series of Flight 2 is revisited in Figure 2.5, where the individual RH_{liquid} time series, the difference of both RH_{liquid} time series, as well as the $T_{ambient}$ and the T_{sensor} time series are shown.

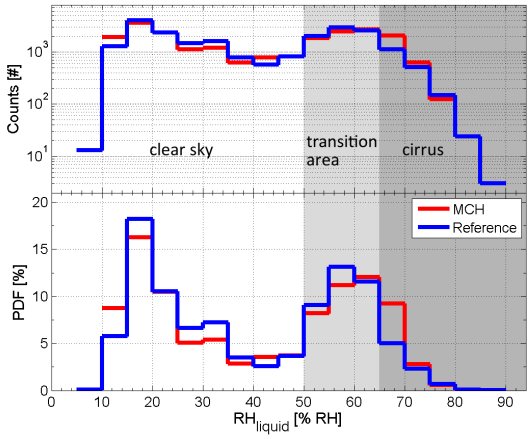

Figure 2.11: Number of data points (top panel) and frequency of occurrence (bottom panel) for observations of RH_{liquid} during CIRRUS-III; blue and red lines refer to data from reference, i.e. FISH (clear sky) and OJSTER (in-cirrus), and MCH, respectively. The number of counts of both data sets agree in almost all 5% RH_{liquid} bins. The exponential decline at higher values is in accordance to the result of Spichtinger et al. [2003a]. A bimodal distribution can be seen clearly in the probability density function (PDF) view of the data sets, where there is a clear sky section at lower values and a cirrus section at higher values, respectively. The differences in the PDF distribution can be mainly explained by the longer response time of the MCH inside and out of clouds.

The following 3 sequences of interest have to be analysed:

- Sequence 1 lasts from 08:40 to 09:10 UTC where the MCH shows still a good response at higher sensor temperatures of about -20°C and agrees within 5 - 10% RH_{liquid} with the reference. However, at decreasing sensor temperature, the response time of the MCH increases significantly. This results in a delay causing higher humidity values and higher differences in the comparison with the reference. Because of the dominating Van der Waals forces the adsorption of new water molecules by the dielectric membrane of the sensor occurs faster than desorption. For that, the response to positive humidity gradient is faster than to negative gradient, which can be seen in the behaviour of the RH_{liquid} differences in time.

- Sequence 2 illustrates a strong humidity change between 09:40 and 10:00 UTC while flying through a cirrus cloud. Because of slower MCH sensor response at colder sensor temperatures, the MCH RH_{liquid} values can not follow the rapid changes in RH_{liquid} as observed by the reference.

- Sequence 3 refers to a section of the flight between 11:00 and 11:40 UTC when T_{sensor} reaches values below the sensor calibration limit of T_{sensor} = -40°C, i.e. ambient temperatures below -70°C at

commercial aircraft speed of Mach-number M = 0.81. The MCH shows an increased response time, a loss of signal fine structure and increasing deviations between the MCH and the reference instruments occur.

Despite delayed sensor response for conditions at the limit of its operation range, the MCH shows a very good overall performance during the CIRRUS-III field study. Figure 2.12 illustrates the PDF of water vapour VMR data as a function of $T_{ambient}$ (panels A to C for the complete data set and panels D to F for the reduced data set, respectively) according to Kunz et al. [2008]. The frequencies of occurrence are calculated in 1°C bins for the MCH data set (panels A and D), the reference data set (panels B and E) and the deviation of MCH and reference PDF for the complete and reduced data set (panel C and F), respectively. The water vapour VMR is binned in logarithmic scale between 0.0 and 8.0 with a bin size of 0.8. The colour bars are binned in 5% spaces for a better interpretation of the contour plots.

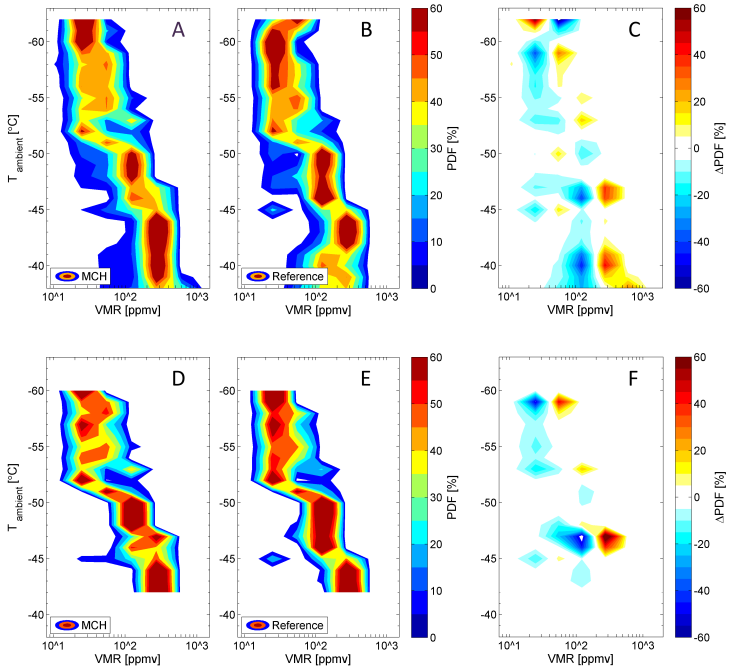

Figure 2.12: Probability density function (PDF) of the complete (A-C) and reduced (D-F) MCH (A, D) and reference (B, E), i.e. FISH (clear sky) and OJSTER (in-cirrus), water vapour volume mixing ratio (VMR) data related to the ambient temperature $T_{ambient}$. Water vapour volume mixing ratio is binned in the logarithmic space between 0 and 8.8 with a bin size of 0.8, the temperature in 1°C bins. Figures C and F show the difference of the MCH and reference PDF for the complete and reduced data set, respectively.

The MCH seems to remain at dryer values for the coldest temperatures of $T_{ambient} \cong$ -60°C, which is again a result of the delayed sensor response at sensor temperatures below the calibration limit. Further, small deviations at lower temperatures are also observed. In summary data sets for both cases show a similar behaviour in the water vapour VMR distribution with only small deviations but these deviations have no statistically significant relevance.

2.5 Conclusions and Recommendations

The CIRRUS-III (2006) aircraft campaign provided the first data set for the evaluation of the MOZAIC Capacitive Hygrometer (MCH) in a blind intercomparison with high performance water vapour instruments based on tunable diode laser absorption spectrometry (OJSTER, in-cloud reference) and Lyman-α fluorescence detection (FISH, clear sky reference).

Except for conditions at its operation limit (e.g. at sensor temperatures $T_{sensor} <$ -40°C and during rapid changes in RH_{liquid}), the MCH performs with a difference of 10% RH_{liquid} or less to the references.

In order to obtain a representative result for the MCH's uncertainty for its regular deployment aboard passenger aircraft, the data set was restricted to conditions corresponding to regular sensor operation aboard MOZAIC aircraft: data with sensor temperatures below -40°C were excluded due to the calibration limit. In MOZAIC less than 1% of RH observations are made at sensor temperatures colder than -40°C. Steep ascent and descent sequences of the aircraft were removed and the maximum ambient temperature ($T_{ambient}$) was set to -40°C to exclude effects of warm clouds.

The 1 Hz correlation yielded a robust linear fit with a slope of unity, with no statistically significant offset and a correlation coefficient of $R^2 = 0.92$ which was confirmed by the correlation of the binned RH_{liquid} data. The RH_{liquid} data grouped in 5% RH_{liquid} bins agree very well for the MCH and reference instruments over the entire cloud-free range and for the most of the cirrus clouds sequences and yield MCH uncertainty of 5% RH_{liquid}.

Comparing the MCH's and references' probability distribution functions (PDF) for RH_{liquid} shows no statistically significant effect of delayed sensor response at conditions beyond the operation range. Neither strong humidity changes, nor operation at the lower calibration limits causes considerable sensor failures. The main limitation for the use of MCH RH_{liquid} data are related to sensor temperatures below the calibration limit of $T_{sensor} =$ -40°C. However, these temperatures are encountered only rarely in the MOZAIC programme as long as the flight routes don't reach polar air masses with ambient temperatures below -70°C. In summary, the MCH is highly suitable for climatology analyses in the MOZAIC programme even if the sensor is not applicable to high time resolution measurements.

A value for the limit of detection is not appropriate for the MCH, but the variable to describe its performance is the here determined uncertainty of the RH_{liquid} measurements. RH_{liquid} measurements below 5%, which are common in the lowermost stratosphere, have to be used carefully because these data are close to the sensor uncertainty range, which as shown before in Section 2.4.1, results in a relative deviation of 100%.

Acknowledgements

The authors gratefully acknowledge Peter Spichtinger (Mainz Univ.) for fruitful discussions. The support by *enviscope* GmbH to the technical organization of the field study is also appreciated. Part of this work was funded by the German Federal Ministry for Research and Education (BMBF) in the framework of the joint programme IAGOS-D under Grant No. 01LK1223A.

CHAPTER 3

QUALITY ASSESSMENT OF MOZAIC AND IAGOS CAPACITIVE HYGROMETERS: INSIGHTS FROM AIRBORNE FIELD STUDIES

P. Neis[1,3], H. G. J. Smit[1], S. Rohs[1],U. Bundke[1], M. Krämer[2], N. Spelten[2], V. Ebert[4,5], B. Buchholz[4,5], K. Thomas[1], and A. Petzold[1]

[1]Forschungszentrum Jülich GmbH, IEK-8 Troposphäre, Jülich, Germany

[2]Forschungszentrum Jülich GmbH, IEK-7 Stratosphäre, Jülich, Germany

[3]Johannes Gutenberg Universität Mainz, Institut für Physik der Atmosphäre, Mainz, Germany

[4]Physikalisch-Technische Bundesanstalt, Gasanalytik und Zustandsverhalten, Braunschweig, Germany

[5]Technische Universität Darmstadt, Analytical Photonics Group, Darmstadt, Germany

This chapter is based on the manuscript "Quality assessment of MOZAIC and IAGOS capacitive hygrometers: insights from airborne field studies" by P. Neis, H. G. J. Smit, S. Rohs, U. Bundke, M. Krämer, N. Spelten, V. Ebert, B. Buchholz, K. Thomas, and A. Petzold, published in Tellus B as Neis et al. [2015b].

Summary. In 2011, the MOZAIC (Measurement of Ozone by AIRBUS In-Service Aircraft) successor programme IAGOS (In-service Aircraft for a Global Observing System) started to equip their long-haul passenger aircraft with the modified capacitive hygrometer Vaisala HUMICAP® of type H. The assurance of the data quality and the consistency of the data set during the transition from MOZAIC Capacitive Hygrometers to IAGOS Capacitive Hygrometers was evaluated within the CIRRUS-III and AIRTOSS-ICE field studies. During these performance tests, the capacitive hygrometers were operated aboard a Learjet 35A aircraft together with a closed-cell Lyman-α fluorescence hygrometer, an open-path tunable diode laser system and a closed-cell, direct tunable diode laser absorption hygrometer for water vapour measurement, respectively. For IAGOS-typical operation conditions, the comparison of relative humidity (RH) data from the capacitive hygrometers and reference instruments yielded remarkably good agreement with an uncertainty of 5% RH. The temperature-dependence of the sensor's response time was derived from the

cross-correlation of capacitive hygrometer data and smoothed data from the fast-responding reference instruments. The resulting exponential moving average function could explain the major part of the observed deviations between the capacitive hygrometers and the reference instruments.

3.1 Introduction

In the framework of the Global Climate Observing System [GCOS , 2010] water vapour was identified as one of the core variables to be monitored for a better understanding, prediction and mitigation of climate change. Particularly, the interaction between the water vapour in the UTLS (upper troposphere and lowermost stratosphere) and tropopause dynamics needs a detailed consideration. This region is characterized by thermal gradients and dynamic barriers controlling atmospheric transport processes. It is most important for climate change and dynamical processes to understand stratosphere-troposphere-exchange [Gettelman et al., 2011], but hardly observable from space or from ground. Since global aviation mainly operates in the altitude band between 9 and 13 km, in-service aircraft equipped with small, compact and light-weight scientific instruments for measuring atmospheric trace constituents are the most powerful tool for collecting in-situ observation data in the extra-tropical UTLS.

Since 1994, the European research programme MOZAIC [Measurement of OZone and water on Airbus In-service airCraft; Marenco et al., 1998] and its successor IAGOS [In-service Aircraft for a Global Observing System; Petzold et al., 2015] have provided regular data for relative humidity (RH) and other meteorological quantities like temperature and pressure as well as data on atmospheric composition (e.g. ozone and CO) with high spatial and temporal resolution on a global scale. Relative humidity data from the MOZAIC programme have been used for various climatological studies including the distribution of upper troposphere humidity [UTH; Kley et al., 2007, Luo et al., 2007, 2008], the distribution of RH with respect to ice [e.g. Gierens et al., 1997, 1999] and ice supersaturation regions [e.g. Gierens et al., 2000, Spichtinger et al., 2003a] in the upper troposphere. A reanalysis of the global MOZAIC RH data set for the period 2000 - 2009 was recently published [Smit et al., 2014].

Atmospheric RH is measured in the MOZAIC/IAGOS approach through a compact airborne humidity sensing device using capacitive sensors Vaisala HUMICAP® of type H (MOZAIC/IAGOS Capacitive Hygrometer: MCH and ICH). The MCH itself, the applied calibration techniques and evaluations are described in detail [Helten et al., 1998, Neis et al., 2015a], while Smit et al. [2008] presents an approach for a potential in-flight calibration.

In 2011, IAGOS aircraft were equipped with a modified Vaisala HUMICAP® of type H sensor. To assure the data quality and the consistency in the data set after the transition from MCH to ICH, we evaluate both sensors during the CIRRUS-III (MCH) and AIRTOSS-ICE (ICH) field studies.

3.2 Description of the modified IAGOS Capacitive Hygrometer

In the following, we describe the modification of the revised compact airborne IAGOS Capacitive Hygrometer. A detailed description and evaluation of the MOZAIC Capacitive Hygrometer is given elsewhere [Helten et al., 1998, 1999, Neis et al., 2015a, Smit et al., 2014]. The ICH uses a capacitive sensor (Vaisala HUMICAP® of type H, Finland) whose capacitance depends on the relative humidity of the dielectric layer of the condenser, and a platinum resistance sensor (Pt100) for the direct measurement of the temperature at the humidity sensing surface. The measurement principle is based on the diffusion-limited adsorption/desorption of H_2O-molecules by the dielectric membrane of the sensor. Since diffusion is strongly temperature-dependent, the sensor response slows down at lower temperatures. Figure 3.1 shows the set-up of the capacitive sensor. The improved hydroactive thin-film polymer composition, with increased capacitance from former 40 - 50 pF to now 180 - 220 pF was introduced in 2011 in the ICH to decrease the sensor response time by increasing its sensitivity.

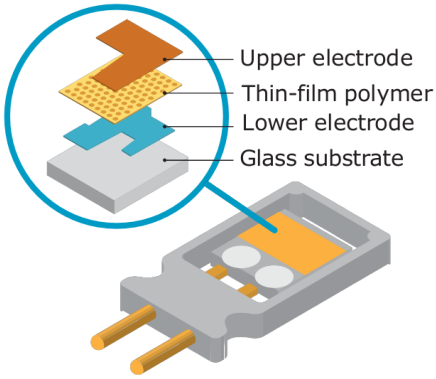

Figure 3.1: The advanced IAGOS Capacitive Hygrometer bases on a compact capacitive sensor measures relative humidity and differs from the MOZAIC Capacitive Hygrometer by the thin-film polymer composition. The improved hydroactive polymer composition of Vaisala HUMICAP® type H has a larger capacitance to increase the sensitivity. For signal processing the Vaisala HMT333 transmitter unit is used. ©Vaisala Oyj, 2015

3.3 Experimental Section

3.3.1 Field Campaigns CIRRUS-III and AIRTOSS-ICE

Both field studies CIRRUS-III and AIRTOSS-ICE used the same twin engine business-jet aircraft of type Learjet 35A operated by *enviscope* GmbH as measurement platform.

The overarching goals of CIRRUS-III, coordinated by the Forschungszentrum Jülich, were to understand the formation mechanism of cirrus clouds for different background conditions, their radiative effects and the microphysical properties of the cirrus cloud particles. In total six flights were conducted in the period between 23 and 29 November 2006 at mid-latitudes (45°N - 70°N) and at flight altitudes between 7 and 12 km. These flights in the UTLS were launched from the Hohn Airforce Base in Northern Germany.

For the sensor intercomparison studies CIRRUS-III provided four flights. The dataset consists of 13 flight hours in air masses colder than -40°C at cruise altitude, four flight hours in cirrus clouds and nine flight hours out of clouds.

As a main conclusion, Neis et al. [2015a] reported a good agreement of the MCH with the reference time series (see Sec. 3.3.2), with an uncertainty of 5% RH with respect to liquid water (RH_{liquid}). During sequences with decreasing sensor temperature, the MCH showed a decreasing sensitivity as a consequence of the increasing response time (see Sec. 3.4.1), i.e. small-scale fluctuations towards higher and lower humidity air masses couldn't be resolved.

In 2013, 2 years after the first aircraft had been equipped with the modified sensor, the ICH was operated aboard the Learjet as part of the field study AIRTOSS-ICE (AIRcraft Towed Sensor Shuttle - Inhomogeneous Cirrus Experiment) to evaluate the performance of the ICH and to assure the data quality after the transition from MCH to ICH. This field study was coordinated by the Johannes Gutenberg-University Mainz and the Leipzig Institute for Meteorology.

The main objectives of AIRTOSS-ICE were to study spatially inhomogeneous cirrus clouds and to understand their formation mechanism in different background conditions, their radiative impacts and the microphysical properties of the cirrus cloud particles. The uniqueness of this campaign was the opportunity to measure simultaneously on two height levels with a towed sensor shuttle [Frey et al., 2009].

This study focused on the main campaign with in total seven flights in the period between 29 August and 5 September 2013. Five of the flights were performed in two military restricted areas above the Baltic and the North Sea. The last two flights were heading to Iceland and back without the towed sensor shuttle. Flight altitudes between 8 and 12 km were reached. The main campaign flights were launched from the Schleswig Air Base in Northern Germany.

The dataset consists of ca. five flight hours in air masses colder than -40°C at cruise altitude, approx. one flight hour in cirrus clouds and four flight hours out of clouds. An overview of both field study data for cruise altitude is provided in Table 3.1.

Table 3.1: Field study data overview for cruise altitude.

	No. of flights	**Period**	**Temperature range [°C]**	**H_2O VMR [ppmv]**	**RH_{liquid} [% RH]**	**In/out of cirrus [min]**
CIRRUS-III	4	24.11. - 29.11.2006	-63 - -42	16 - 360	10 - 78	217 / 537
AIRTOSS-ICE	7	29.08. - 05.09.2013	-57 - -40	6 - 530	1 - 83	60 / 193

3.3.2 Instrumentation

During the CIRRUS-III and AIRTOSS-ICE field campaigns, high-precision research-grade instruments were operated aboard the aircraft to characterise the air masses probed during flight patterns in frontal cirrus clouds. An important part of the instrumentation was dedicated to the measurement of the gas-phase and condensed-phase water. An instrument overview and the parameters derived from these measurements are listed in Table 3.2. The CIRRUS-III instrumentation included a MCH and an open-path tunable diode laser (TDL) system [open-path Jülich Stratospheric TDL ExpeRiment OJSTER; MayComm Instruments, Krämer et al., 2009, May and Webster, 1993] to measure gas-phase water vapour volume mixing ratio (VMR). Simultaneously, total water VMR (= gas-phase plus evaporated ice water) was measured by the well-established, closed-cell Lyman-α photofragment fluorescence hygrometer FISH [Fast In-Situ Hygrometer, Meyer et al., 2015, Zöger et al., 1999], which was equipped with a forward facing inlet to sample gas-phase water in clear sky and total water inside cirrus clouds. FISH is regularly calibrated in the laboratory as well as in the field to a MBW DP30 reference frostpoint hygrometer and thus is regarded as transfer standard between aircraft measurements and the ground based reference. OJSTER is compared to and, if necessary, adjusted to the FISH measurements as described by Krämer et al. [2009]. To determine whether a data point is inside a cirrus cloud or not, the ratio of relative humidity with respect to ice (RH_{ice}) from FISH (total water) and OJSTER (water vapour) was used [see Krämer et al., 2009].

The AIRTOSS-ICE instrumentation was similar with an ICH and FISH. For gas-phase water vapour VMR measurements, a novel instrument, the calibration-free (first principles), direct tunable diode laser absorption (TDLAS) hygrometer SEALDH-II [Selective Extractive Airborne Laser Diode Hygrometer,

Table 3.2: Participating hygrometers during CIRRUS-III (a) and AIRTOSS-ICE (b).

Instrument	**Detection quantity**	**Measurement technique**	**Response time**	**Uncertainty**	**Reference**
MCH[a] & ICH[b]	RH_{liquid} [% RH]	Capacitive sensor	LT: 1 s MT: 10 s UTLS: 1 min	$\pm$5% RH	(1)
FISH[a,b]	VMR [ppmv]	Lyman-α fluorescence hygrometer	1 s	7%$\pm$0.3 ppmv (precision 1%)	(2)
OJSTER[a]	VMR [ppmv]	open-path TDL	1 s	10-15%	(3)
SEALDH-II[b]	Molar density	Direct TDLAS	0.5 s	4.3%$\pm$3 ppmv 0.083 ppmv at 1 s	(4)

MCH & ICH: MOZAIC & IAGOS Capacitive Hygrometer; FISH: Fast in-situ Stratospheric Hygrometer; OJSTER: Open-path Jülich Stratospheric TDL ExpeRiment; SEALDH-II: Selective Extractive Airborne Laser Diode Hygrometer; LT: lower troposphere; MT: middle troposphere; UT: upper troposphere; LS: lower stratosphere; for further information see Bange et al. [2013]. References: (1) Neis et al. [2015a], (2) Meyer et al. [2015], (3) May and Webster [1993], (4) Buchholz et al. [2013]

Buchholz et al., 2013] was used. The SEALDH-II was validated via a comparison to the metrological water vapour scale and a primary humidity standard [Buchholz et al., 2014]. Again, the cirrus cloud data points have been determined from the ratio of RH_{ice} from FISH (total water) and SEALDH-II (water vapour).

For both field campaigns we finally used reference water vapour time series combining FISH data in the cloud free sequences and TDL instrument data for the in-cloud sequences.

3.3.3 Data Overview

For the evaluation of the MCH and ICH performances and to assure the data quality after the transition, we classified the probed air masses of both field studies and related them to conditions met in the MOZAIC and IAGOS programmes.

An obvious criteria is the sensor temperature. Both capacitive hygrometers are regularly calibrated in the atmospheric simulation chamber at Jülich [Smit et al., 2000] before installation on the aircraft, and again after detachment. For both, these calibrations are made over a sensor temperature range between -40 and $+20\,^{\circ}$C against (i) a Lyman-α photofragment fluorescence hygrometer [Kley and Stone, 1978] for water vapour VMR below 1000 ppmv and (ii) a dew/frost point hygrometer (General Eastern, Type D1311R) for water vapour VMR above 1000 ppmv [Smit et al., 2000].

Another reason for classifying the field study data by the sensor temperature is the fact that [Neis et al., 2015a] have observed an improvement in the agreement with the reference humidity data with increasing sensor temperature, i.e. with decreasing response time of the hygrometer.

The distributions of measured sensor temperatures during 15 years of MOZAIC measurements, and during CIRRUS-III and AIRTOSS-ICE are shown in Figure 3.2 as probability distribution functions (PDF's). The large data set of 15 years of MOZAIC measurements can be described as a Gaussian distribution with its maximum at -22°C broadened with higher values from the ascent and descent sequences, when approaching or leaving the airport. T_{sensor} colder than the minimum calibration temperature -40°C occur in less than 1% of the data.

Most probable T_{sensor} during CIRRUS-III is at -38°C with 15% of the data colder than -40°C. The distribution is shifted to colder temperatures, i.e. shifted to longer response times relative to the MOZAIC PDF results.

AIRTOSS-ICE showed a shift to warmer temperatures compared to the MOZAIC data. The most probable T_{sensor} is at -18°C with less than 1% of the data colder than -40°C. This results in a shorter response time compared to both other data sets.

In the following section, we describe the methodology to determine the temperature-dependent response time. This property is needed for the comparison of the capacitive hygrometer evaluations during two field studies with different ambient conditions.

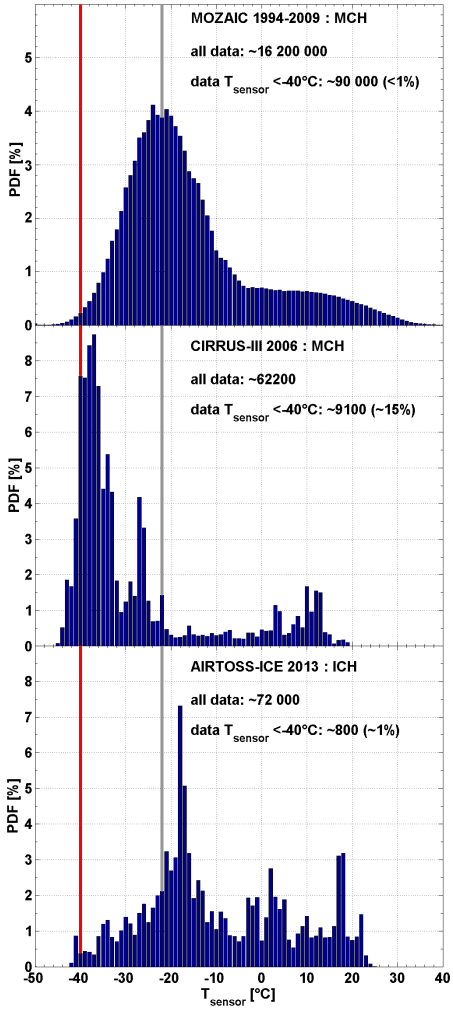

Figure 3.2: Probability distribution functions (PDF) show the distributions of the measured sensor temperatures during A) 15 years of MOZAIC measurements, B) CIRRUS-III, and C) AIRTOSS-ICE. The red line indicates the lower limit of the sensor calibration. The grey line illustrates the most probable value of MOZAIC distribution.

3.4 Methodology of Performance Evaluation

Former evaluation studies of the MCH showed a good agreement with high-precision water vapour instruments [Helten et al., 1998, Neis et al., 2015a]. However, they also reported a decreasing sensitivity of the MCH with decreasing sensor temperatures as a result of an increasing but unspecified response time.

The reduced temperature range of CIRRUS-III data does not permit a reliable analysis for the MCH on its own. But with a combined data set of CIRRUS-III and AIRTOSS-ICE measurements (see Fig. 3.2), the complete MOZAIC-relevant temperature range from -40°C to 0°C is covered to define the temperature-dependent response time and to evaluate both sensors without this technical restriction.

3.4.1 Temperature-dependent Response Time

The impact of the temperature-dependent response time τ can be seen in the extracted time-series sequence of an AIRTOSS-ICE flight in Figure 3.3. With increasing sensor temperature, the difference of the $\mathrm{RH_{liquid}}$ measurements of ICH and the reference, i.e. in clear sky and below 1000 ppmv water vapour VMR the FISH instrument, otherwise SEALDH-II, decreases.

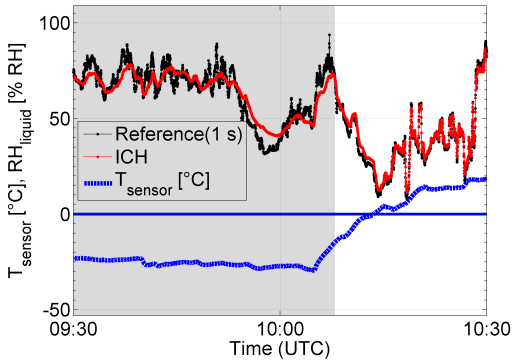

Figure 3.3: $\mathrm{RH_{liquid}}$ and T_{sensor} (blue dotted line) sequence of an AIRTOSS-ICE flight. Small-scale fluctuations of the measured reference $\mathrm{RH_{liquid}}$ (black line) can be resolved by the ICH (red line) in warmer air masses (white background). In colder air masses with $T_{\mathrm{sensor}} <$ -20°C the ICH seems to measure the smoothed background.

For different types of Vaisala radio sondes deploying also capacitive Vaisala HUMICAP® RH sensors [Miloshevich et al., 2004] have determined experimentally in a laboratory study the response time of the RH sensors at different temperatures which showed a strong exponential increase at decreasing sensor temperatures. Qualitativily, we expect a similar exponential response time behavior for the Vaisala HUMICAP® RH sensor of the MCH and ICH instrument at low temperatures.

Although the hydroactive thin-film polymer composition might be the same, the design of the Vaisala HUMICAP® RH sensor used in MCH or ICH is rather different compared to the sensor deployed on Vaisala radiosondes, such that significant quantitative differences in their temperature dependent time response can be expected. In this study the temperature-dependent time response τ is derived experimentally from the flight data as follows:

For each flight of the two field studies, an exponential moving average (EMA, [Lucas and Saccucci, 1990]) with a fixed τ (1 - 501 s in 2 s steps) is applied to the reference relative humidity time series RH_t (see Eq. 3.1). The used EMA is defined as a linear transformation of RH_t to a smoothed relative humidity time series ($\widetilde{\mathrm{RH}}_t$) according to

$$\widetilde{\mathrm{RH}}_t = \widetilde{\mathrm{RH}}_{t-1} + \alpha \cdot (\mathrm{RH}_t - \widetilde{\mathrm{RH}}_{t-1}), \tag{3.1}$$

where $\alpha = \frac{2}{\tau+1}$. Subsequently, the flight is grouped in distinct sensor temperature intervals. These temperature intervals T_i of width 5 K are defined as $T_i = (T_i - 2.5 < T_i \leq T_i + 2.5)$, where $T \in \{233 : 5 : 273\}$ K. Then the cross correlation factor R^2 is determined between the smoothed reference $\widetilde{\mathrm{RH}}_t$ and the responsible MCH or ICH RH_t measurement for every temperature interval.

An example shown in Figure 3.4 demonstrates the way to extract the most probable response time. Upon calculating all the cross correlation factors R^2 for the measurements in the temperature interval $T_i = 243$ K for AIRTOSS-ICE Flight 3, the most probable response time τ can be determined by the distinctive maxima in R^2. If there is in addition a minimum number of 600 values (equivalent to 10 minutes flight) in the temperature bin, this τ and T-value data pair is used for the further calculation of the temperature-dependent time response equation.

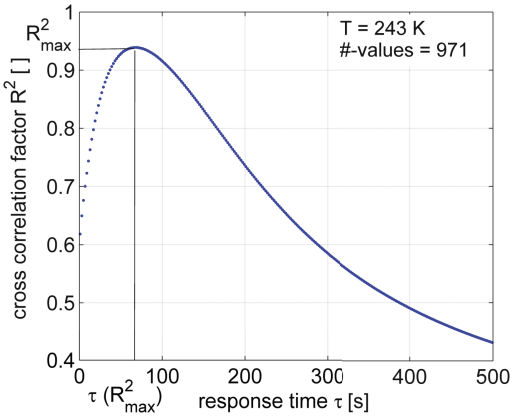

Figure 3.4: Example to demonstrate the way to determine the most probable, i.e. with maximum R^2, response time $\tau(R^2_{\max})$ in the temperature bin $T = 243$ K for AIRTOSS-ICE Flight 3.

In Figure 3.5 the determined τ values are plotted against T_{sensor} for all flights of the two field studies. Because the advanced ICH confirms and expands the MCH behaviour, it was possible to merge both field study response times for the calculation. As described before, the number of τ values per temperature depends on the number of measurement values (minimum 600 values) and the existence of the distinctive maxima in the R^2 distribution. A robust fit function yields the temperature-dependent time response equation

$$\tau = \exp(30 \; - \; 0.1033 \cdot T_{\mathrm{sensor}}), \tag{3.2}$$

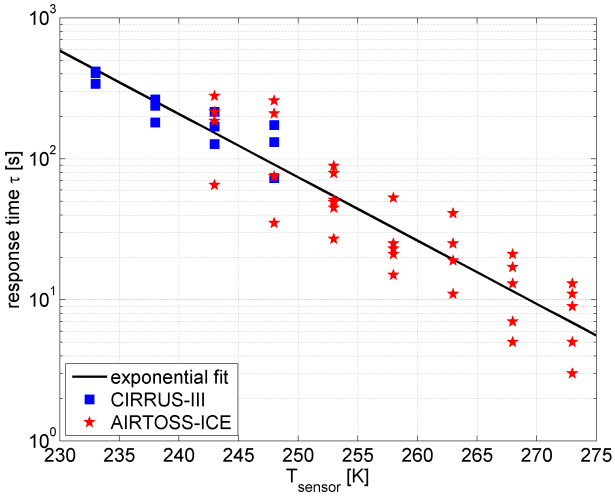

Figure 3.5: Determined response times per temperature bin and flight for the CIRRUS-III (blue squares) and AIRTOSS-ICE (red stars) flights. The robust exponential fit (black line) through the data leads to the MCH and ICH characteristic temperature-dependent response time τ (see Eq. 3.2).

with T_{sensor} in units of Kelvin. With decreasing sensor temperature, τ increases from a few seconds at 273 K to a few minutes below the calibration limit of 233 K. The increase in the spread of τ in some temperature intervals might be a result of the flight pattern with an increased or decreased amount of flight level changes.

The validity check for this function is visualised in Figure 3.6 with an example flight of AIRTOSS-ICE. The envelope of the original 1 Hz $\mathrm{RH_{liquid}}$ difference, i.e. ICH - reference, increases from $\pm 5\%$ to $\pm 10\%$ $\mathrm{RH_{liquid}}$ with decreasing T_{sensor} of -18°C to -30°C. The ability of the ICH to resolve small-scale fluctuations in $\mathrm{RH_{liquid}}$ reduces with the lower temperature. Later in flight, T_{sensor} increases significantly, which immediately leads to differences of less than 1% $\mathrm{RH_{liquid}}$ to the reference value.

The EMA smoothing function is defined by the previously determined temperature-dependent response time (see Eq. 3.1). After applying this function to the reference $\mathrm{RH_{liquid}}$ time series, the ICH time series is

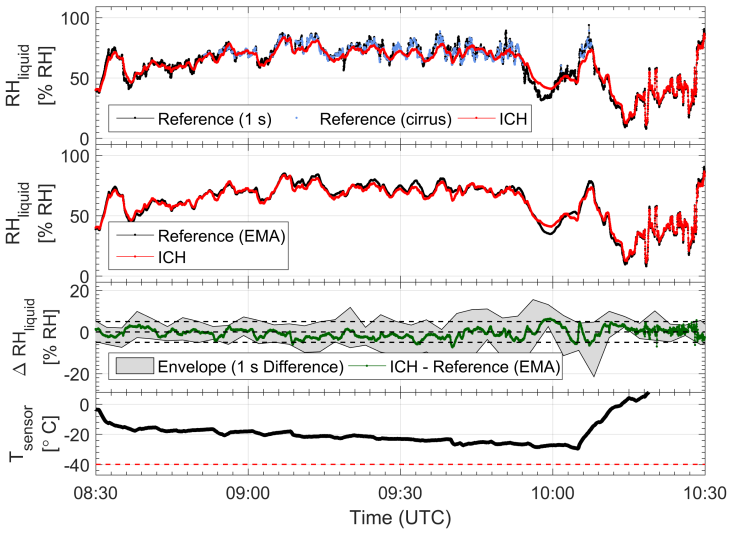

Figure 3.6: From top to bottom: RH_{liquid} measured by the ICH (red) and the original reference (black), i.e. FISH (clear sky) and SEALDH-II (in-cirrus (blue dots) and above 1000 ppmv); RH_{liquid} measured by the ICH (red) and the smoothed reference (EMA including the temperature-dependent response time, black); Δ RH_{liquid} (ICH and reference) as envelope for the original reference and as green line for the smoothed reference, as a function of flight time during the AIRTOSS-ICE Flight on 3 September 2013; and sensor temperature T_{sensor} (black) as well as the lower temperature limit of the calibration (red).

reproduced for almost the complete cold flight sequence without getting worse in the warmer sequence of the flight. The remaining deviations might originate in calibration uncertainties, as well as in the potential deviations in the response time for conditions when RH_{liquid} is either increasing or decreasing [Wildmann et al., 2014] and uncertainties in the reference measurement.

3.5 Results

We extracted a subset of the measured data set, which corresponds to the regular operation conditions of the MCH and ICH aboard long-haul passenger aircraft. The MOZAIC/IAGOS typical conditions are characterised by the sensor temperature T_{sensor}, which depends on the cruising speed of the aircraft. As described in Sec. 3.3.3, the regular passenger-aircraft speed of approx. 0.81 M causes a heating of the ambient temperature through adiabatic compression in the Rosemount housing and leads to sensor temperatures $T_{sensor} \geq$ -35°C, which is above the lower calibration limit of -40°C.

However, during CIRRUS-III the operation aboard the slower-flying Learjet 35A (cruising speed less than 0.70 M), T_{sensor} values significantly lower than -40°C were reached; see Fig. 3.2. Data with T_{sensor} less than -40°C were excluded from the analysis.

To minimise the perturbation of measurements by potentially sampled liquid water droplets in warm clouds, the maximum T_{ambient} was set to the level of instantaneous freezing of -40°C. A perturbation of measurements by potentially sampled ice crystals haven't been observed by [Neis et al., 2015a]. Since the steep ascents and descents of the Learjet 35A are not comparable to conditions aboard long-haul passenger aircraft, these flight sequences were also excluded from the analysis.

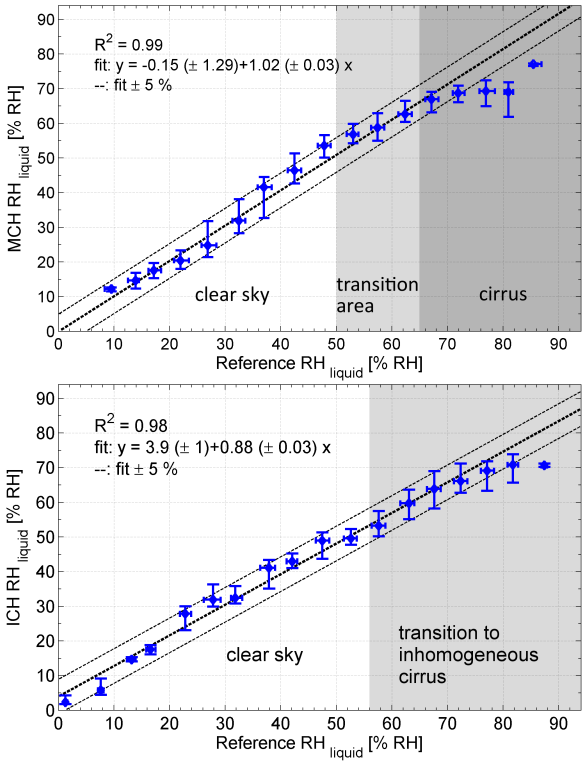

Figure 3.7: Top panel presents comparisons between the $\mathrm{RH}_{\mathrm{liquid}}$ data from MCH and the original reference, i.e. FISH (clear sky) and OJSTER (in-cirrus), during CIRRUS-III. Bottom panel shows results of comparisons between ICH and the original reference, i.e. FISH (clear sky) and SEALDH-II (in-cirrus and above 1000 ppmv), during AIRTOSS-ICE campaign; the straight line indicates the linear regression line, while the dashed lines illustrate the sensor uncertainty range $\pm 5\%$ $\mathrm{RH}_{\mathrm{liquid}}$. In the transition area measurements of both reference instruments can occur.

A statistically based view on the measured data set is shown in Figure 3.7, where the correlation between the sensors averaged for 5% RH_{liquid} bins is shown. The MCH agrees very well with the reference instruments over the entire range of values measured in the cloud-free atmosphere. Inside cirrus clouds (see top panel in Figure 3.7), i.e. $RH_{liquid} > 65\%$, the sensors deviate as expected since the increased MCH response time decreases with decreasing T_{sensor}. In turn, the sensitivity of the MCH decreases and small-scale fluctuations cannot be resolved. Linear regression analysis provides a correlation coefficient of R^2 = 0.99 with an offset of -0.15 $\pm$ 1.29% RH_{liquid} and a slope of 1.02 $\pm$ 0.03. Median values and almost all of the 25^{th} and 75^{th} percentiles fall within the $\pm$5% RH_{liquid} range around the linear regression line.

Similar results are found for the intercomparison of ICH and the measured reference (see bottom panel in Figure 3.7), where the correlation between the sensors averaged for 5% RH_{liquid} bins confirm the uncertainty of 5% RH_{liquid}. Inside the transition to inhomogeneous cirrus, i.e. $RH_{liquid} > \sim$56%, the variability of ICH values increases mainly as a result of the increased response time. The analysed originally measured data provides a correlation coefficient of R^2 = 0.98 with an offset of 3.90 $\pm$ 1.00% RH_{liquid} and a slope of 0.88 $\pm$ 0.03.

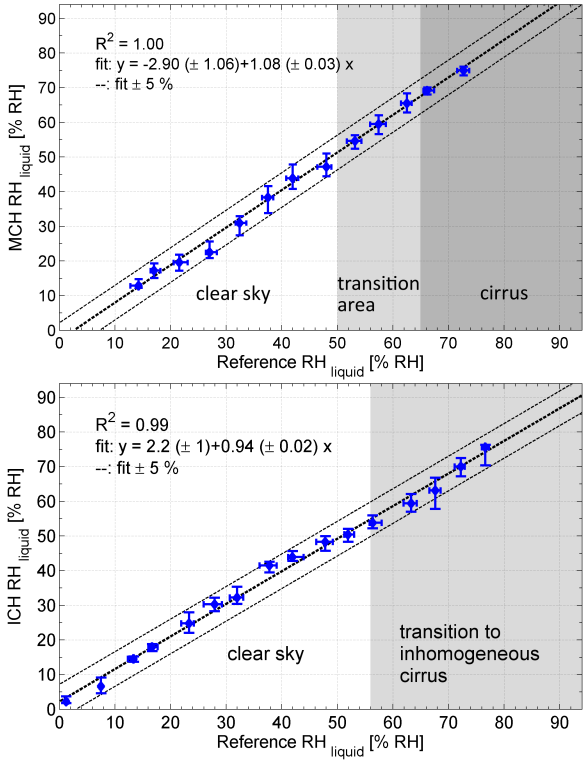

Figure 3.8: This Figure is the similar to Fig. 3.7, but the reference is EMA smoothed prior to comparisons.

After smoothing the reference data by the previously determined temperature-dependent response time, the correlation between MCH or ICH and the responsible reference data are shown in Figure 3.8. Since both correlations reveal an improvement, i.e. median values of each bin converge to the linear regression line with a clearly reduced variation, the main driver of measured deviations can be attributed to the temperature-dependent response time τ.

This fact can be confirmed by Figure 3.9, where the ratios of the measured ICH and MCH medians to the measured (left panel) and the smoothed (right panel) reference' medians are provided for CIRRUS-III (MCH, subfigure a)) and for AIRTOSS-ICE (ICH, subfigure b)), respectively.

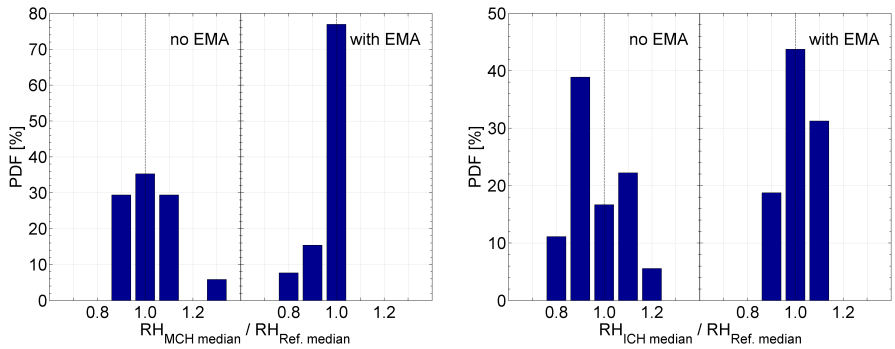

(a) (b)

Figure 3.9: Frequency of occurrence of the ratios of MCH to reference $\mathrm{RH_{liquid}}$ (subfigure a) and of ICH to reference $\mathrm{RH_{liquid}}$ (subfigure b), respectively. Both figures are divided into the PDF of original (left panel) and smoothed (right panel) reference data.

Both PDFs show clearly a more narrow distribution around the ratio 1 with the applied temperature-dependent response time algorithm. The asymmetry in the distribution of Figure 3.9(a) is caused by the sample of the 25 - 30% $\mathrm{RH_{liquid}}$ bin in the MCH versus smoothed reference distribution (see Fig. 3.8). However, the deviation is still within the 5% $\mathrm{RH_{liquid}}$ uncertainty.

3.6 Conclusions

Since 1994, long-haul passenger aircraft participating in the MOZAIC programme were equipped with a capacitive hygrometer Vaisala HUMICAP® of type H (MCH), measuring upper troposphere humidity. In 2011, the first aircraft of the successor programme IAGOS were equipped with the modified Vaisala HUMICAP® type H sensor (ICH). To assure the data quality and the consistency of the data set during the transition from MCH to ICH, we have evaluated both sensors during the CIRRUS-III (MCH) and AIRTOSS-ICE (ICH) field studies against similar reference techniques.

In order to obtain results for sensor uncertainties representative for its regular deployment aboard passenger aircraft, a subset of data was extracted, which corresponds to the typical MOZAIC/IAGOS operation conditions. Data with sensor temperatures below -40°C and thus below the calibration limit were excluded and strong ascent and descent sequences of the more agile aircraft were removed. Finally, the maximum ambient temperature was set to -40°C to exclude effects of warm clouds.

The RH_{liquid} data grouped in 5% RH_{liquid} bins agreed very well in cross correlations for MCH and ICH and the respective reference instruments over the entire cloud-free range and for the most of the cirrus clouds sequences and yields the uncertainty of 5% RH_{liquid}.

Main deviations between the capacitive hygrometers and reference RH_{liquid} data are related to decreasing sensor temperatures. Combining both field campaigns, it was possible to determine the temperature-dependence of the sensor's response time. MCH and ICH RH_{liquid} data were reproduced by applying the resulting exponential filter function to the measured reference RH_{liquid} data. The temperature-dependence of the capacitive hygrometer response time may also be used to extend the measurement range of the instrument to the dry conditions of the lowermost stratosphere. Contrary to earlier approaches [Helten et al., 1998] MCH and ICH data may now considered valid, if the flight time of the aircraft in the lowermost stratosphere exceeds the sensor response time for the given temperature.

Furthermore, we showed that the quality of the UTH data is preserved during the transition from the MCH to the modified ICH. Both sensors showed similar behaviour in same conditions, which ensures a long-time data set for UTLS water vapour climatology and trend analyses, when combining MOZAIC and IAGOS UTH data sets.

Acknowledgements

The authors gratefully acknowledge Fanny Finger (Leipzig Univ.) and Marcus Klingebiel (Mainz Univ.) for planning and leading the AIRTOSS-ICE field campaign. We also acknowledge Peter Spichtinger (Mainz Univ.) for fruitful discussions. The support by *enviscope* GmbH for the technical organization of the field study is also appreciated. Part of this work was funded by the German Federal Ministry for Research and Education (BMBF) in the framework of the joint programme IAGOS-D under Grant No. 01LK1223A and 01LK1301A.

CHAPTER 4

DISTRIBUTION OF WATER VAPOUR IN THE UTLS

4.1 Introduction

Since 1994, commercial passenger aircraft are measuring, amongst other, relative humidity with respect to liquid water (RH_{liquid}), and temperature in the European research programmes MOZAIC and IAGOS. These regular flights on a global scale are unique in its quantity, continuity, and quality of measurements of upper tropospheric and lowermost stratospheric (UTLS) air masses. In this chapter, the analyses of water vapour distribution properties in the UTLS over the North Atlantic flight corridor will be presented, based on a large set in statistical sense.

4.2 North Atlantic Flight Corridor as first Target Region for MOZAIC Data Analysis

The North Atlantic flight corridor covers 40 - 60°N latitude and 5 - 65°W longitude and is the overall first region for which the MOZAIC data set is explored for statistically relevant and robust analyses of upper tropospheric and lowermost stratospheric (UTLS) humidity. Prior analysis of Gierens et al. [1997, 1999, 2000] used the first 5 years of MOZAIC humidity data to describe the humidity distribution over the North Atlantic which was then used to improve the cloud scheme in the ECMWF forecast model including a new parametrisation of supersaturation with respect to ice in the cloud-free part of the grid box [Tompkins et al., 2007]. The suitability of the North Atlantic flight corridor for the UTLS analysis is caused by its long-term

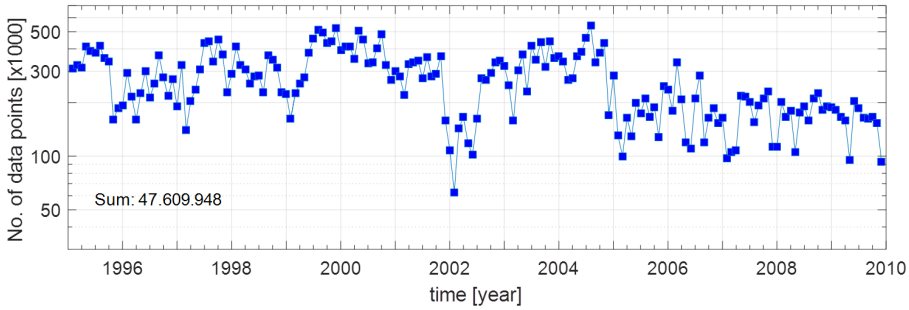

Figure 4.1: The number of data points probed by the MOZAIC programme in the North Atlantic flight corridor and above 280 hPa between 1995 and 2010 document the long-term, continuous, homogeneous, and dense data.

(since 1994), continuous (no gaps), homogeneous (less variation in the monthly number of data points), and dense data (high number of monthly data points).

Within the 15 years, a yearly amount of 500 to 1500 flights (compare with Chapter 1.3) accounts for about 48 million data points in the North Atlantic flight corridor at flight altitudes exceeding the 280 hPa pressure level. The measurements over the North Atlantic are well distributed over the entire analysed period (Figure 4.1) and on spatial scale considering 2°x 2° grid cells (see Figure 4.2). At least 750 samples

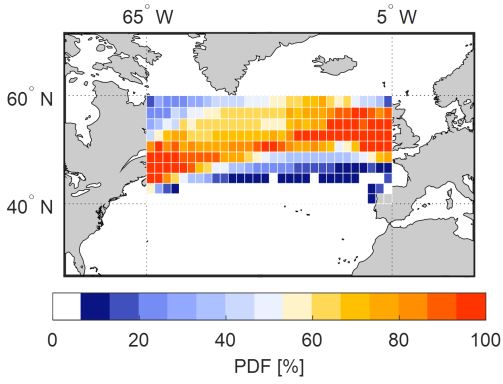

Figure 4.2: Probability density function of median monthly data points in the North Atlantic flight corridor at flight altitudes exceeding the 280 hPa pressure level during the period 1995 to 2009. 100% is according to a monthly median of at least 1200 data points in the 2° grid boxes. Continuous sampling over 15 years of measurements provide at least 750 data points per month in the bulk of the grid boxes.

per grid cell were measured which corresponds to one flight hour per month. Thus, flight tracks by the aircraft cover a much larger region, compared to the restricted flight tracks over the continents, e.g. South Africa and Eurasia (see again Chapter 1.3).

All RH_{ice} data measured in this selected region were correlated against ozone volume mixing ratio and colour-coded with the RH_{ice} probability density function (PDF) in every 25 ppbv ozone VMR bin (Figure 4.3). As precondition, only data are considered which are flagged with at least limited water vapour data validity, sensor temperatures in the range of the sensor calibration, i.e. T_{sensor} above -40°C (corresponds to ambient temperatures above -70°C for the MOZAIC-typical aircraft speed of Mach-number M = 0.81 (see Section 2.2)), ambient temperatures below -40°C and relative humidities with respect to liquid water below saturation to neglect liquid water contaminations. Three categories of air masses can be revealed, of which one type is characterized with high humidity (modal value in RH_{ice} at 100%), low ozone VMR (below 120 ppbv), and PV values less than 2 PVU (blue contour line). Second air mass type has low humidity data (modal value below 20% RH_{ice}), high ozone values (above 150 ppbv), and PV values above 5 PVU, whereas the third one represents the transition between the two former types.

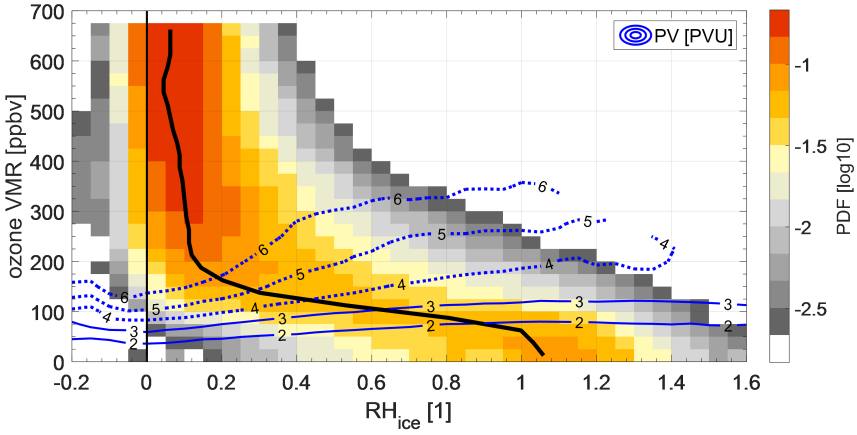

Figure 4.3: Cross correlation of measured RH_{ice} and ozone volume mixing ratio colour coded with the humidity probability for each 25 ppbv ozone VMR bin. The black line represents the most probable RH_{ice} value with a clear separation between low RH_{ice} above 120 ppbv ozone VMR and high values around ice saturation for ozone VMR below 75 ppbv. Additionally, the potential vorticity contour lines between 2 PVU and 6 PVU are shown with the blue dashed lines.

For a better understanding of the representativeness of the MOZAIC data, the opportunity was taken to use the complete campaign data set of the well-established, closed-cell Lyman-α photofragment fluorescence hygrometer FISH [see Section 3.3.2 and Meyer et al., 2015, Zöger et al., 1999]. The compared FISH data set includes in-situ measurements of research aircraft flights over Western Europe, i.e. longi-

tudes between 5°W and 5°E latitudes between 30° and 70°N, at flight altitudes less than 280 hPa, and the temperature restrictions equal to the MOZAIC's restrictions. Additionally, ozone measurements have to be available for each flight. The correlation of $RH_{ice,FISH}$ and ozone VMR colour-coded by the PDF of the cross correlation is shown in Figure 4.4. The main result with three characteristic air mass types is also obvious, whereby the most probable humidity data at low ozone VMR values is shifted from supersaturation to drier values below saturation. Further, the high precision of the FISH measurements leads to a more narrow humidity distribution above 200 ppbv ozone VMR. However, the statistical deviation of MOZAIC (blue dashed line) and FISH (black line) most probable RH_{ice} is in the order of the MCH uncertainty of 5% RH_{ice} (see Section 3.5). An additional reason can be the different region of measurements. Whereas the MOZAIC data provide measurements over the North Atlantic for a long time, the present FISH data set is restricted to their campaign base locations on continental Western Europe. Subsequent studies (Chapter 6) on IAGOS upper tropospheric humidity distributions in clear sky and cirrus clouds also showed moister conditions in both subsets over the maritime North Atlantic compared to the continental mid-latitudes.

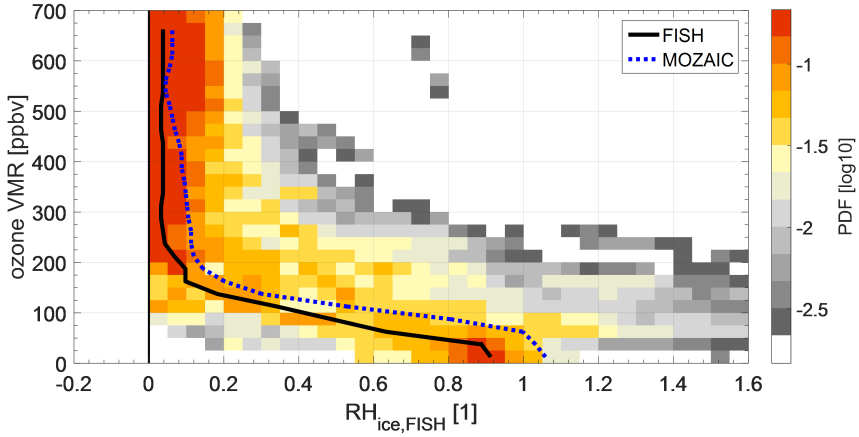

Figure 4.4: Similar to Figure 4.3: For the RH_{ice} and ozone volume mixing ratio cross correlation the complete data set of FISH measurements between 30°N and 70°N over Western Europe is used. Again, the black line represents the most probable RH_{ice} value. For a comparison between general distributions measured by FISH and by the MCH within the MOZAIC programme, the most probable MOZAIC RH_{ice} values are shown with the blue dash-dotted line.

As it is known from several studies [e.g. Bethan et al., 1996, Gierens et al., 1999, Thouret et al., 2006, Zahn et al., 2004], ozone can be used as a vertical coordinate especially for the stratosphere. With the empirical determined ozone volume mixing ratio (VMR) threshold of 120 ppbv [Thouret et al., 2006], the here found three characteristic types of air masses can be interpreted as the atmospheric layers troposphere (ozone VMR less than 120 ppbv), stratosphere (ozone VMR exceeding 120 ppbv), and the transition layer

defined by the tropopause (ozone VMR around 120 ppbv). In the following section, the MOZAIC measurements will be analysed within the scope of a new coordinate system depending on the tropopause height.

4.3 Vertical Separation of Observations relative to the Tropopause Height

Aircraft based measurements of atmospheric state variables and chemical composition usually refer to the aircraft flight altitude or pressure level, respectively. Furthermore, the atmosphere is layered into distinct spheres which are described by the chemical composition and gradients in the state variables. But the transition of the lowest spheres, i.e. the troposphere and stratosphere, can vary in height and depth in dependence of space and time [Gettelman et al., 2011]. This variation of the sphere's transition layer height can be understood by a MOZAIC example flight (see Figure 4.5), where the aircraft was flying for around 400 minutes at a constant pressure. While flying on constant pressure level, the aircraft measures stratospheric (yellow shaded) ozone volume mixing ratios above the threshold of 120 ppbv (red dashed line, Thouret et al. [2006]), values close to 120 ppbv ozone volume mixing ratio in the transition layer (grey shaded), and far lower values in upper tropospheric air masses. This example flight points out the need to distinguish between the three atmospheric layers regardless of the geometric altitude.

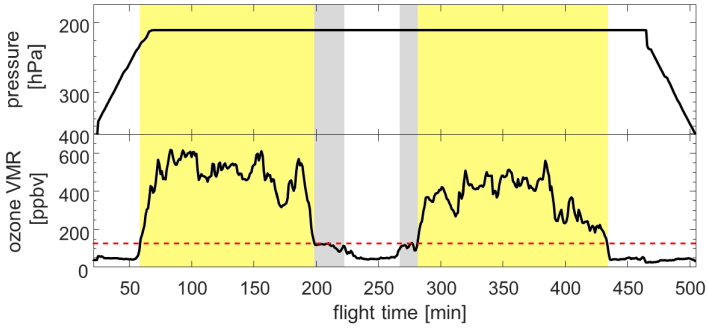

Figure 4.5: The upper panel shows the pressure of a MOZAIC example flight with around 400 minutes of constant flight pressure. The measured ozone volume mixing ratio (VMR) is represented with the black line in the lower panel. Stratospheric air masses with ozone VMR larger than the threshold of 120 ppbv (red dotted line) are shaded with yellow, whereby the air masses in the transition layer with ozone VMR close to 120 ppbv are shaded with grey.

The most frequently used atmospheric tracers for this type of study are ozone and CO [Gettelman et al., 2011, Hoor et al., 2002, 2004, Pan et al., 2004, Tilmes et al., 2010]. Both tracers have strong gradients across the transition layer, and their chemical lifetimes are longer than the transport timescale in this region. Ozone is measured in the MOZAIC programme from the very beginning and can describe the vertical position in the stratosphere with its positive and strong gradient. A benchmark for ozone volume mixing ratios in the

lowest stratosphere is around 120 ppbv [Gierens et al., 1999, Thouret et al., 2006]. The measurements are realised with the UV-absorption instrument Model 49-103 (Thermo Scientific), where the ambient air at cruise altitude pressure of 230 $\pm$ 50 hPa is sucked in with a Teflon KNF Neuberger pumping system. The detection limit of 2 ppbv and the accuracy of $\pm$2 ppbv $\pm$ 2% is warranted due to comparisons to the periodic reference of an internal ozone generator, regular inspections and absolute recalibrations in the laboratories by CNRS staff in Toulouse before and after each operation period of about 6 months [Marenco et al., 1998, Nédélec et al., 2015, Thouret et al., 1998a]. However, it can not be used to describe the vertical position in the troposphere, because the air masses are well-mixed and ozone is chemically removed in the troposphere. Carbon monoxide (CO) is measured by an improved infra-red filter correlation instrument with a precision estimated at $\pm$ 5 ppbv $\pm$ 5% [Nédélec et al., 2015]. CO, that is measured in MOZAIC since 2001, has its sources in the troposphere and negligible sources in the stratosphere. Pan et al. [2004] reported that CO volume mixing ratio below 80 ppbv is characteristic for the lowest stratosphere.

Due to the delayed start of CO measurements, the in-situ measured chemical approach is not possible for this work. Instead, the humidity data since 1994 will be vertically separated relative to the tropopause height. For this purpose, we have to define the tropopause in a meaningful way.

Since a broad spectrum of tropopause height definitions in scientific work exists [Ivanova, 2013], the two most often used definitions have been chosen.

- The thermal tropopause which is defined by the temperature lapse rate, i.e. where the lapse-rate decreases to 2°C/km or less and remains at least in the overlying layer of 2 km [WMO, 1957]. The basis data set for the thermal tropopause height is the 6 hourly, 1° horizontally gridded and previously on pressure level interpolated ECMWF ERA-Interim reanalysis data which is linearly interpolated in space and time for every MOZAIC flight track [Kunz et al., 2014].

- The dynamical tropopause which is defined by a sharp gradient in the potential vorticity (PV). The here used value to define the tropopause is PV = 2 PVU (1 PVU= 10^6 K m^2 kg^1 s^1, standard potential vorticity unit) [e.g. Holton et al., 1995]. The basis data set for the dynamical tropopause height is the ECMWF operational analysis and forecast data for meteorological fields (1 x 1°, 31 levels in 1994 to 137 levels in 2013, every 6 h) [Petetin et al., 2015].

Figure 4.6(a) displays the monthly mean pressure of the tropopause height in the North Atlantic flight corridor. The suitability of this region for air quality analysis around the tropopause is demonstrated with Figure 4.6(b) where the frequency distribution of the aircraft pressure at cruise altitude is on the tropopause height level around 230 $\pm$ 50 hPa. In addition, it is demonstrated that the thermal (WMO) tropopause lies always above the dynamical (PV2) tropopause.

This offset of $\sim$20 hPa between both definitions demonstrates the complexity to find a valid definition for the global transition or mixing layer, respectively. Hoerling et al. [1991] and Hoinka [1998] reported that the dynamical tropopause approach with a range of possible values (1.6 - 3 PVU) is only useful in the extratropics. They argue that the sign of PV values in the tropics mathematically change from positive values on the Northern Hemisphere to negative values on the Southern Hemisphere which therefore forces

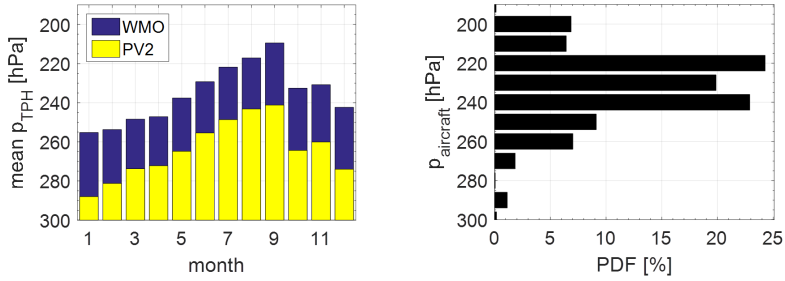

(a) (b)

Figure 4.6: (a) Mean of monthly median tropopause height: thermal (WMO; blue) and dynamical (PV2; yellow) tropopause definition. (b) Probability density function of measured pressure levels over the North Atlantic.

the PV values to zero at the equator. It is also reported that the statistically best match between thermal and dynamical tropopause height was found for PV = 3.5 PVU. This explains the continuous median offset of 20 hPa (blue line) from the thermal tropopause (black line) to the 2-PVU-tropopause as the ”lower limit of the tropopause region” [Brunner et al., 2001], like it is presented in Figure 4.7. On the other hand, Hoerling et al. [1991] reported that the empirically determined thermal approach misses the physical background and

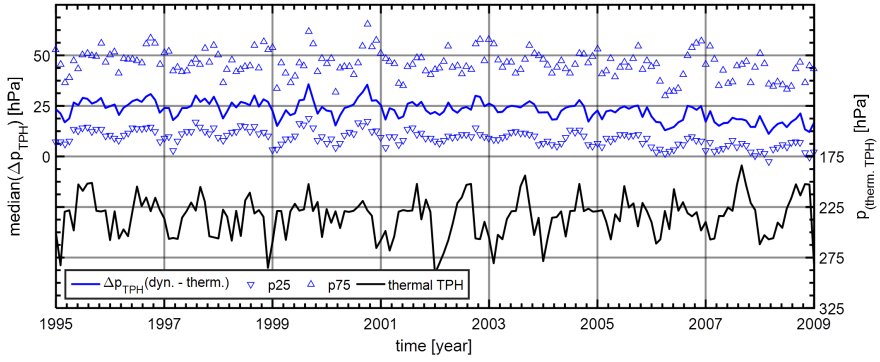

Figure 4.7: Time series of median monthly tropopause pressure difference (dynamic - thermal; blue line). The blue triangles show the 25^{th} and 75^{th} percentiles of the monthly differences and therefore representing the monthly variability. Right axis and black line refer to the pressure of the thermal tropopause height (TPH).

thus has its disadvantages in the vicinity of developing baroclinic disturbances which then again explains the high monthly variability in the pressure offset.

From now on, data will be distributed into three main layers according to Thouret et al. [2006], i.e. the upper troposphere, tropopause layer, and lowermost stratosphere, of which the outer layers are further subdivided into three sublayers. The width of the sublayers considers the average difference between the ozone and thermal tropopause of 780 m (30 hPa at this altitude) [Bethan et al., 1996]. The resulting seven 30 hPa thick bins separate the aircraft pressure relative to the tropopause pressure and are summarised in Table 4.1.

Table 4.1: The data are distributed into three main layers: the upper troposphere, tropopause layer, and lowermost stratosphere. The outer layers are additionally subdivided into three sublayers. The distribution criterion is the pressure difference between the aircraft pressure p_{AC} and the tropopause pressure p_{TPH} with the range of 15 hPa.

Main name	**Short name**	**p_{AC} - p_{TPH} [hPa]**
Lowermost Stratosphere	LS3	-90
	LS2	-60
	LS1	-30
Tropopause Layer	TL	0
Upper Troposphere	UT1	+30
	UT2	+60
	UT3	+90

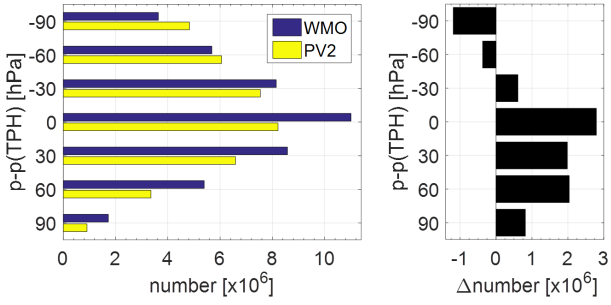

Figure 4.8: Comparison of vertical number of data distribution: thermal (WMO; blue) and dynamical (PV2; yellow) tropopause definition. The right panel shows the difference (WMO - PV2) in the number distribution in each vertical layer.

The impact of different tropopause definitions on the analysis is first shown with the vertical number of observations distribution in the seven layers. The dynamical tropopause definition contains 5% more data in the stratosphere compared to the thermal tropopause definition. Besides that, 34% and 45% more data contribute to the tropopause layer and tropospheric layer, respectively, when using the thermal definition (compare with Figure 4.8). Overall, the thermal tropopause definition increases the number of selected data by about 18%.

For both cases, the vertical temperature distribution shows the expected patterns with a decrease of temperature up to the coldest layer around the tropopause, followed by a temperature increase with height. The difference in the vertical temperature distribution in dependency of the definition is shown in Figure 4.9 where the median monthly temperature in the tropospheric layer is slightly colder with the dynamical approach. In contrast, the temperature increase in the first stratospheric layer is approx. 3 K stronger with the thermal tropopause definition which indicates a more stable stratification and for that a much stronger barrier for air mass transition through the tropopause layer.

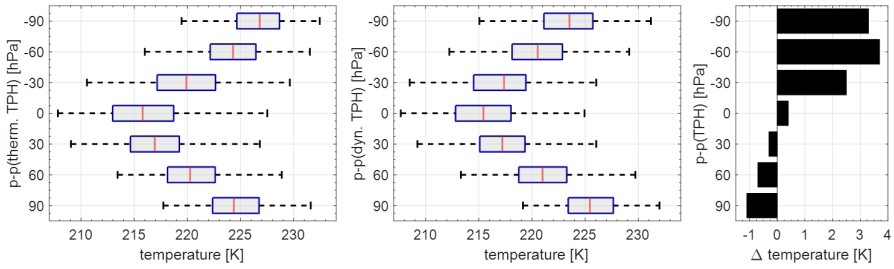

Figure 4.9: Vertical distribution of temperature. Comparison between distributions relative to the thermal (left panel) and dynamical (middle panel) tropopause criteria. The resulting difference (WMO - PV2) in the median temperature for each vertical layer is shown in the right panel.

Figure 4.10 describes the vertical distribution of the ozone volume mixing ratio. Both tropopause definitions yield a small variation of ozone in the tropospheric layers of about 50 to 100 ppbv. When entering the tropopause layer the thermal approach shows a median monthly ozone VMR of 120 ppbv which is consistent with the threshold value for the chemical tropopause by Thouret et al. [2006] and the mean ozone value of 127 ppbv at the thermal tropopause calculated of 90 vertical soundings over Jülich, Germany by Duhnke et al. [1998]. In contrast, the dynamical approach has an air mass content with ozone values below 120 ppbv which implicates a mixing layer including mainly tropospheric air masses. Furthermore, in the first stratospheric layer there are more than 25% of the ozone measurements in the range of tropospheric air masses. Nevertheless, both approaches show a significant increase of ozone VMR with height in the stratosphere, whereby the thermal definition yields a much stronger increase, i.e. more than 100 ppbv stronger, after entering the stratosphere.

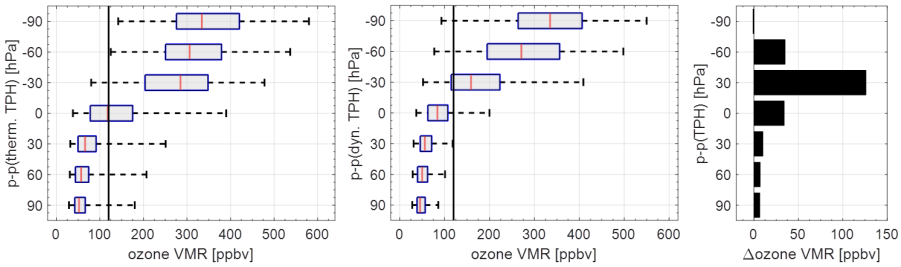

Figure 4.10: Vertical distribution of ozone volume mixing ratio (VMR). Comparison between distributions relative to the thermal (left panel) and dynamical (middle panel) tropopause criteria. The black vertical line represents the 120 ppbv ozone VMR threshold value for the chemical tropopause by Thouret et al. [2006]. The resulting difference (WMO - PV2) in the median ozone VMR in each vertical layer is shown with the right panel.

Altogether, this analysis showed again the difficulties to find a clear definition of the tropopause layer. While the dynamical tropopause seems to mark the bottom of the extratropical tropopause layer [Hegglin et al., 2009, Hoor et al., 2004], the thermal tropopause is located more in the centre and top of the extratropical tropopause layer [Hegglin et al., 2009]. However, the conclusion after these comparisons is, to select the thermal tropopause definition for the further analysis of the 15 years of relative humidity measurements over the North Atlantic. The reason for the decision is, that the stronger delimitation of tropospheric and stratospheric air masses by, e.g. the temperature gradient and ozone gradient, corresponds more to the concept of stratification and the concept of a mixing layer in-between these spheres.

4.4 Climatologies of Humidity

15 years of UTLS water vapour measurements by the MOZAIC programme generated an unique and powerful data set for further analyses. After selecting the thermal tropopause height definition to separate the measured data relative to the tropopause height into distinct layers (see Section 4.3), different types of illustration of humidity climatologies over the North Atlantic will be presented.

A climatology describes the average state of the atmosphere above a specified region. Thus, the median of the seasonal RH_{ice} distribution for every height layer is shown in Figure 4.11 (see also Table 4.2.). The tropospheric layer covers a wide spread of humidity from 10% RH_{ice} to 140% RH_{ice} in its extremes. There is also a high variation in the distribution characterised by 50% of the data within a range of 50% RH_{ice}. Furthermore, the distributions of the tropospheric layers are skewed to the left which implies a modal value higher than the median value of about 75 to 86% RH_{ice}.

The stratospheric layers cover a more narrow spread of humidity with height, i.e. the maximum in all stratospheric layer is reduced from saturation to 30% RH_{ice}, whereas the minimum is constant with about

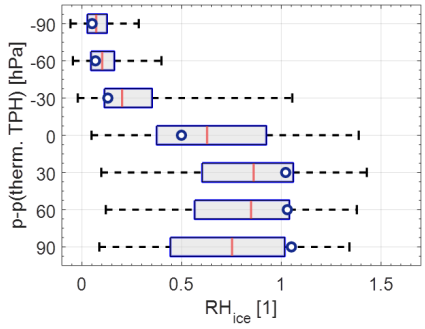

Figure 4.11: Vertical distribution of RH_{ice}. The box and whisker plots represent the median of seasonal [1, 25, 50, 75, 99] percentiles. The circles indicate the modal value in each vertical layer.

6% RH_{ice}. Compared to the large variability in the tropospheric distribution, 50% of the stratospheric data fall within a smaller range of 15% RH_{ice}. Moreover, the distributions of the stratospheric layers are skewed to the right which implies a modal value smaller than the median value of about 7 to 20% RH_{ice}.

The distribution in the tropopause layer can be interpreted as a mixture of the uppermost tropospheric and lowermost stratospheric layers. Besides the reduced median value of 63% RH_{ice}, the distribution includes dry and humid data, like it is expected from the definition as a mixing layer [Pan et al., 2004].

The probability density function (PDF) and the cumulated probability (see Figure 4.12 (a) and (b)) of the seven vertical RH_{ice} distributions illustrate the different air mass signatures also for similar atmospheric layers. The tropospheric layer closest to the tropopause (UT1), for instance, is the most humid layer which is shown by the slowest increase in the cumulative probability. Moreover, it is shown, that a bimodalisation is developing with increasing distance to the tropopause in the upper troposphere. That means, the UT1 layer includes mostly uplifted or cooled air masses which results in mostly saturated air. In comparison,

Table 4.2: Summary of statistical results with percentiles (perc.) and modal values for the vertical distributions of RH_{ice} data (see Figure 4.11 and 4.12).

p - p(therm. TPH)	**RH_{ice} [1]**					
[hPa]	**1 perc.**	**25 perc.**	**50 perc.**	**75 perc.**	**99 perc.**	**modal**
-90 (LS3)	-0.06	0.03	0.07	0.12	0.29	0.05
-60 (LS2)	-0.05	0.05	0.10	0.16	0.40	0.07
-30 (LS1)	-0.02	0.11	0.20	0.35	1.06	0.13
0 (TL)	0.05	0.38	0.63	0.92	1.39	0.50
30 (UT1)	0.10	0.60	0.86	1.06	1.43	1.02
60 (UT2)	0.12	0.57	0.85	1.04	1.38	1.03
90 (UT3)	0.09	0.44	0.75	1.02	1.34	1.05

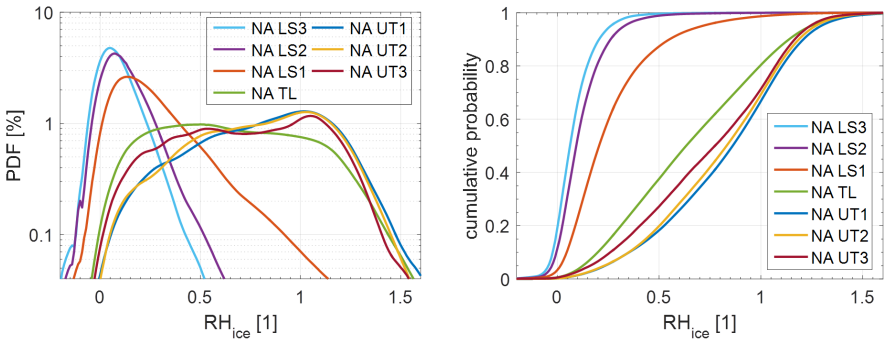

(a) (b)

Figure 4.12: Vertical RH_{ice} distributions as probability density function (a) and cumulated probability (b).

an additional dry mode develops with increased distance to the tropopause, e.g. at about 50% RH_{ice} in the UT3 PDF. In other words, this layer includes, besides the dominating uplifted or cooled air masses, air masses that are descending and warmed. Compared to the troposphere the stratosphere shows a different signature. A strong monomodal distribution in the stratospheric layers describes the stratification with negligible upward motion. This causes the strongest increase in the cumulative probability of the highest stratospheric layer (LS3) which, in consequence, denotes the driest vertical layer.

As described earlier, the relative humidity on a quasi-constant pressure level (see Table 4.3) depends on the temperature and the available water vapour quantity (such as the volume mixing ratio) according Equation 1.1. Figure 4.13 shows the temperature's PDF (a) and cumulated probability (b) in the seven vertical layers, respectively. With exception of layer LS3, the distributions show a quasi-Gaussian behaviour. The explanation for the left-skewed distribution in the highest lowermost stratospheric layer is the increasing stratification with height, whereby the restriction of data selection is still below 233.15 K (corresponds to -40°C) for ambient temperatures. Furthermore, the tropopause layer (TL) is the coldest layer with a modal value of approx. 216 K, like expected from the thermal definition; the UT1 layer is slightly warmer but comparable in its distribution, whereas the layer distributions of UT2 and LS1 as well as UT3 and LS1, respectively, are identical. Since the temperature PDFs are uniformly distributed, they can be reconstructed with a Gaussian fit function of type

$$f(x) = a \cdot exp(-((x-b)/c)^2). \tag{4.1}$$

With this function applied, the modal value (corresponds to variable b) of the temperature's PDF is calculated. This calculated modal values (Table 4.3) confirm the graphs in Figure 4.13(a) where the coldest layer is the TL with 216 K, followed by the UT1 with 217 K. Moreover, UT2 and LS1 are represented with the modal value of 220 K, whereby UT3 and LS2 have a calculated modal temperature of 225 K. The warmest layer LS3 confirms the strong stratification and reaches the modal value of 228 K.

Finally, the vertical distributions of H_2O VMR are shown in Figure 4.13(c) and (d). An overall clear picture appears with a lognormal distribution for every layer. With increasing height, the monomodal but slightly leftward skewed distribution is getting narrower until the MOZAIC humidity measurements reach its limits of accuracy on the H_2O VMR basis in the upper LS layers. The modal H_2O VMR (see Table 4.3) is calculated with 27 and 24 ppmv, respectively, in these layers, whereas the distributions for the other layers seem to be clearly structured with modal values of 27 and 43 ppmv down to the tropopause layer and with an higher increasing rate for the tropopause layers up to a modal value of 135 ppmv in the UT3 layer.

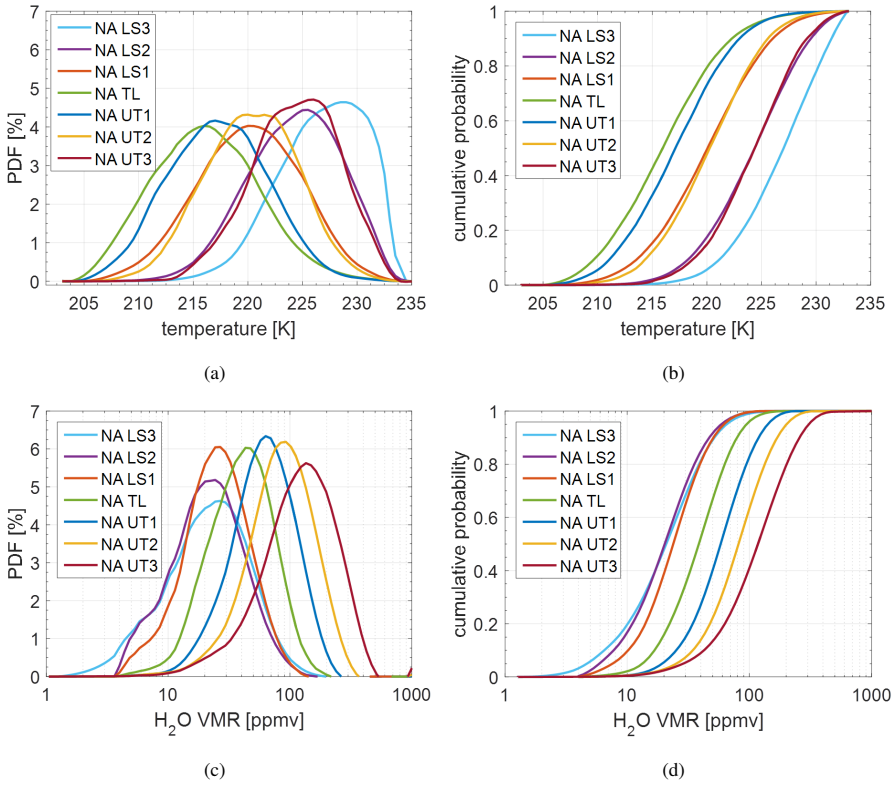

Figure 4.13: Similar to Figure 4.12: The probability density function (a, c) and the cumulated probability (b, d) of the seven vertical temperature (a, b) and H_2O VMR (c, d) distributions. The variation of H_2O VMR over several orders of magnitude requires a binning in the logarithmic space between 1 and 3 with a bin size of 0.0414.

4.5 Comparison with ECMWF Climatologies

Berkes et al. [2016] compared the MOZAIC temperature measurements from the past 18 years (1995 to 2012) with the independent but assimilated temperatures of ECMWF ERA-Interim. By so doing, the UTLS

Table 4.3: Modal values for the vertical distributions of calculated temperature, H_2O VMR data (see Figure 4.13), as well as the median pressures with its almost similar variation of 11 ± 1 hPa, calculated from half of the interquartile range.

p - p(therm. TPH) [hPa]	**-90**	**-60**	**-30**	**0**	**30**	**60**	**90**
modal temperature$_{\mathrm{calc.}}$ [K]	228	225	220	216	217	220	225
modal H_2O VMR [ppmv]	27	24	27	43	63	93	135
median pressure [hPa]	226	227	227	227	228	238	239

temperatures are analysed for different regions, including the North Atlantic, and separated into the lowermost stratosphere, the tropopause layer and the upper troposphere using the thermal tropopause from ERA-Interim as reference layer.

There they found, that the temperature inter-annual variability within all regions and layers is mostly consistent between in-situ observations and ERA-Interim which results in an absolute bias between both data sets for the North Atlantic of 0.81 ± 0.72 K warmer in-situ temperatures, a high correlation coefficient of determination of $R^2 = 0.97$ and a slope of 0.94 in the cross correlation's regression fit. Despite the fact of a good agreement, inconsistency in the linear temperature trends and their signs have been observed. For the North Atlantic lowermost stratosphere, the Mann-Kendall-test [Gilbert, 1987] derived a significant (p-value $= 0.05$) positive trend in ERA-Interim and a insignificant (p-value $= 0.98$) small negative trend in the in-situ measurements.

The reason for the observed deviations between the temperature trends was explained with the inconsistent bias between the temperature time series which was explained with improvements of assimilations and increasing amounts of measurements after 2006 in the model.

Now, the 6 hourly ECMWF ERA-Interim reanalysis data, 1° horizontally gridded and previously interpolated on pressure level [Kunz et al., 2014], are used for the same humidity analysis like in the previous two sections. To accomplish that task, the RH_{ice} and ozone volume mixing ratios are linearly interpolated in space and time for every MOZAIC flight track. Furthermore, only ERA-Interim data are used for the comparison with the MOZAIC cross correlation, which are also part of the MOZAIC data set. The resulting correlation of $RH_{ice,era}$ and ozone VMR_{era} is colour-coded by the PDF of the cross correlation (see Figure 4.14), whereas the overlaid contour lines of the MOZAIC PDF reveal the differences between both data sets. The high ozone (more than 150 ppbv), low humidity (modal value below 20% RH_{ice}) type of air mass is more narrow in the modelled humidity which can be mostly explained with the calibration uncertainties of the MCH (see Section 2.2). The main difference is found in the low ozone (below 120 ppbv), high humidity (modal value at 100% RH_{ice}) type of air masses. In both cases the most probable RH_{ice} is around saturation, but the assimilated data cuts off the humidity at about 115% RH_{ice} and excludes high supersaturation like it is measured in-situ by the FISH and MCH instruments. Nevertheless, the air mass type of the transition layer is well represented in all cases with a similar spread in the humidity distribution.

To compare the humidity and temperature climatologies of both data sets, the vertical distributions of median temperature, H_2O VMR, RH_{ice}, and fraction of ice supersaturated regions (ISSR), i.e. regions

where RH_{ice} exceeds 100%, are further subdivided into the four seasons winter (DJF), spring (MAM), summer (JJA), and fall (SON). In order to achieve the best possible representativeness of the seasons, the median values of seasonal distributions are calculated and averaged over the 15 years. The gained results for the MOZAIC data set are shown in the first row of Figure 4.15 and will be the first data set which is described in detail; ERA-Interim results and the differences between both data sets will continue afterwards.

The temperature distribution shows a similar behaviour in all four seasons. A negative vertical gradient up to the tropopause layer with the coldest temperatures is followed by a stronger positive gradient in the stratosphere. The only difference is found in the absolute median values, where the winter is the coldest season with approx. 212 K in its minimum and the summer is the warmest season with approx. 219 K in its minimum. Furthermore, the spring season is slightly colder than the autumn season.

The water vapour mixing ratio distribution shows a similar behaviour in the tropospheric layers but a different behaviour in the lowermost stratosphere. Whereas the warm seasons are the seasons with the highest H_2O VMRs with a linear decrease up to the TL the cold seasons exhibit the fewest amount of H_2O VMRs with a exponential decrease up to the TL. Moreover, the stratospheric layers represent a different type of air masses, where the median value in the summer season drops from about 30 ppmv in the lowest stratospheric layer to less than 20 ppmv in the highest layer. Compared to the summer all other seasons and stratospheric heights seem to be quite constant at about 20 ppmv.

As a result of the previous seasonal distributions, the RH_{ice} seasonal distribution arises. The cold seasons show a constant median relative humidity in the UT with a median RH_{ice} of about 90%, whereas the warm seasons start at 65% RH_{ice} and increase with height to a median of more than 80%. The tropopause layer

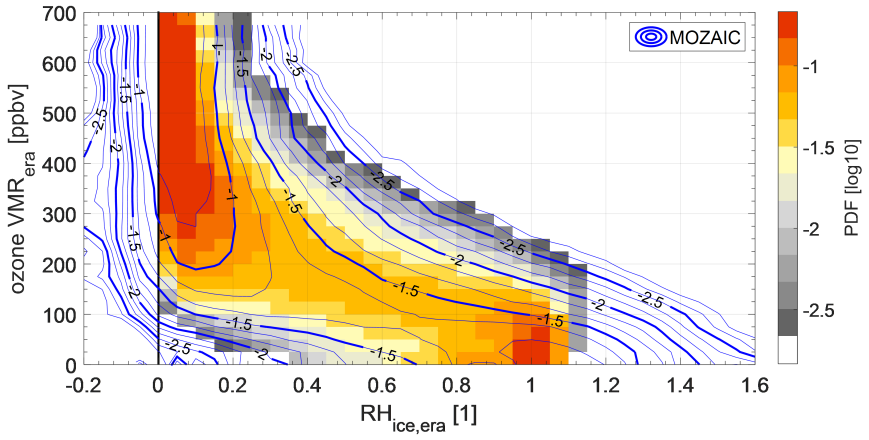

Figure 4.14: Similar to Figure 4.3: For the RH_{ice} and ozone volume mixing ratio cross correlation the complete data set of ECMWF ERA-Interim reanalysis is used. The blue contour lines refer to the MOZAIC-based distribution.

has no significant difference in the seasons with a median of approx. 63% RH_{ice}. In the stratospheric layers the behaviour is again similar for all seasons with the driest (down to 4%) summer and wettest (down to 12%) winter season.

Finally, the fraction of ISSRs in the seasonal vertical layers are compared. As it can be expected from the median RH_{ice} distributions, the stratospheric fraction of ISSR is insignificant for all seasons. In addition, the seasonal fraction of ISSR varies widely in the upper troposphere, where the cold months have a median value between 30 and 40% with its highest values in the lowest layers. In contrast, the warm seasons have a median value of 19 to 24% in the lowest UT layer and an increase to 28 to 32% in the highest UT layer.

Second row of Figure 4.15 presents the mean seasonal distribution of the median temperature, H_2O VMR, RH_{ice}, and fraction of ISSR from the ECMWF ERA-Interim data set. The absolute difference between ERA-Interim and MOZAIC distributions, the standard deviation of the difference can be seen in the third and fourth row. respectively.

There is an overall agreement in the seasonal distributions with the only significant differences in the fraction of ISSR distributions, where the model misses 10% of the UT ISSR fraction. The maximum difference of ISSR observations is in the lowest UT layer in the cold seasons with up to 23%. Nevertheless, this discrepancy was expected from the definition of model cloud parametrization which converses instantaneously the supersaturation into ice water [Tompkins et al., 2007] when ice is present because ice cloud conditions are not assimilated directly Ma et al. [2012]. The modelled temperature distributions differ in the order of magnitude of the temperature in-situ measurements but with with slightly colder conditions for all seasons and heights, expect the tropopause layer, of approx. 0.25 K. The median temperature difference of more than 0.25 K in the tropopause layer can be explained with the vertical resolution of the model. If the minimum in the vertical distribution is not matching a model level, then this minimum cannot be resolved and is shifted to the nearest pressure level but with a higher value. So this is the case for the temperature, where the reduced spatial resolution of the model smooths out the distinct minimum of temperature by about 0.5 K compared to the other layers. There is also a slightly higher variation in the difference in the stratospheric layers which cannot be explained here.

The seasonal distributions of modelled H_2O VMR and RH_{ice} show the closest agreement in summer seasons, when only the lowest lowermost stratospheric layer differs in the order of magnitude of the uncertainty (5% RH) or its limits of accuracy (10 ppmv) drier in the MOZAIC measurements, respectively. All other seasons show slightly higher humidities by more than 5% RH_{ice} or 10 ppmv compared to the MOZAIC measurements with highest deviations in winter which again affects the ISSR frequency.

4.6 Conclusions

For the first time, water vapour distributions in the vicinity of the extratropical tropopause layer are analysed with such a high vertical resolution, for such a long period, and with such a statistical robustness like it is possible with the MOZAIC in-situ measurements. In this chapter, the first analyses of 15 years of MOZAIC relative humidity measurements in the North Atlantic flight corridor are discussed. The suitability

of this region for an in-depth analysis is proven with well distributed flight paths on cruise altitude and the documented long-term, continuous, homogeneous, and dense data set.

With a comparison of MOZAIC in-situ measurements of ozone VMR and relative humidity with respect to ice (RH_{ice}), the probing of three atmospheric air mass layers is demonstrated. The confirmation of measuring in the upper troposphere (low ozone VMR, high relative humidity), lowermost stratosphere (high

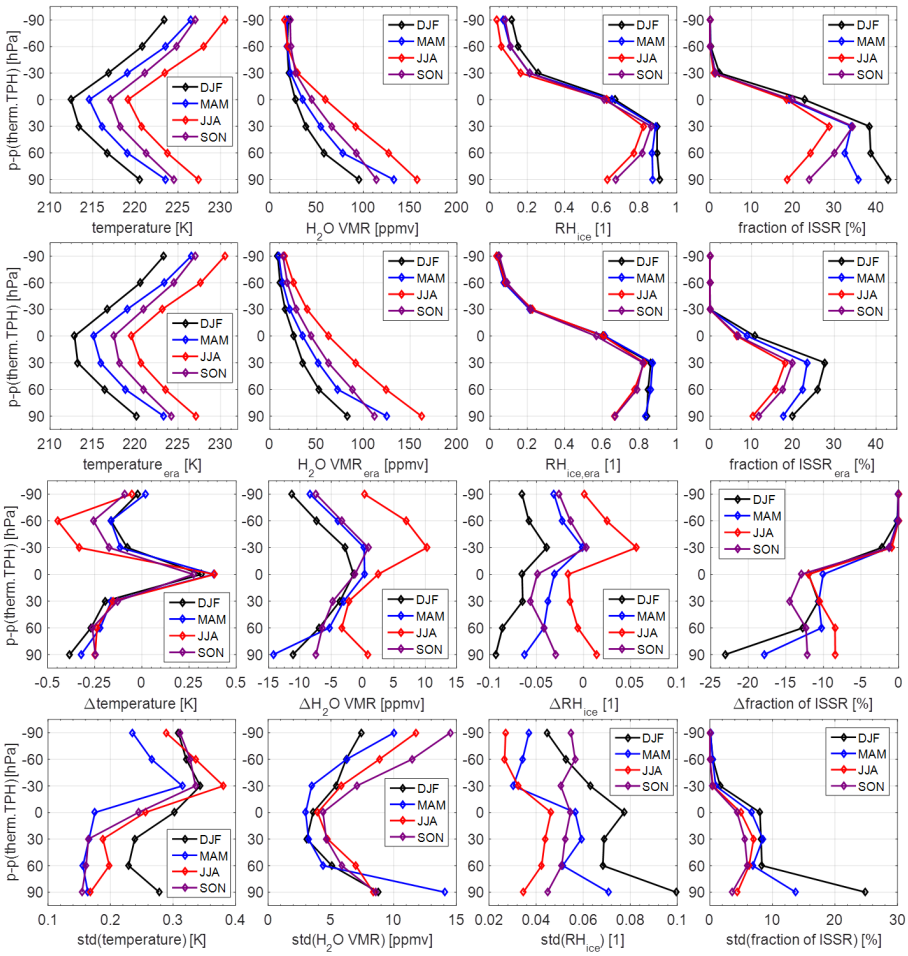

Figure 4.15: Mean seasonal distribution of median temperature, H_2O VMR, RH_{ice}, and fraction of ice supersaturated regions. From top to bottom: MOZAIC measurement data, ERA-Interim modelled data, difference between ERA-Interim data and MOZAIC data (i.e. ERA-Interim - MOZAIC), and standard deviation of the difference between ERA-Interim data and MOZAIC data.

ozone VMR, low relative humidity) and the tropopause layer (transition between both layers) is achieved with the similar distribution gained by the complete data set of the well-established hygrometer FISH.

The need for distributing the samples into the corresponding seven atmospheric layers centred around the tropopause prior to further analysis is reflected by evaluating the consequences of tropopause definition selection. The conclusion of using the thermal tropopause definition instead of the dynamical one in this study, is justified with the stronger delimitation of tropospheric and stratospheric air masses by, e.g. the temperature and ozone gradients which corresponds more to the concept of stratification and to the concept of a mixing layer between the spheres.

Having achieved that, the MOZAIC humidity measurements in the North Atlantic flight corridor were subject to a comprehensive analysis. The three stratospheric layers are characterized by a monomodal distribution of RH_{ice} in the dry mode down to 5% RH_{ice} and a development of an increased skewness rightward down to the tropopause layer. This mixing layer is defined by a broad RH_{ice} distribution with a spread of 54% (interquartile range). It is also seen that upper tropospheric layers are most probable supersaturated and develop a dry mode with increased distance to the tropopause which might be explained by subsided air masses.

While temperatures follow linear Gaussian distributions with coldest layer in the tropopause, the water vapour volume mixing ratios (H_2O VMR) show an exponential Gaussian distribution with stepwise decrease with height. H_2O VMR measurements in the driest stratospheric layers indicate irregularities which is explained by the lower limit of MCHs accuracy ($\sim$10 ppmv).

Finally, the results are compared with model statistics gained from ECMWF ERA-Interim reanalysis data, which was extracted from the 6 hourly model output and linearly interpolated on the flight tracks. Main features of the ozone VMR$-RH_{ice}$ comparison are confirmed, whereas MCH data scatter statistically in the dry values and the model cuts off ice supersaturation when ice is present.

Seasonal vertical distributions agree well in the variables of temperature, relative humidity and water vapour volume mixing ratio, but temperatures in the tropopause layer show a significant signal to warmer temperatures in the model. Humidity in the summer is matched from both observations, however, in-situ measurements seem to be moister in the range of measurement uncertainty ($\sim$5% RH_{ice}). The missing of about 10 - 15% probability in the upper tropospheric fraction of ice supersaturation is the most obvious difference and requires further investigations.

CHAPTER 5

TRANSPORT PROCESSES AND PATHWAYS

5.1 Introduction

Vertical distributions of relative humidity with respect to ice, in-situ measured in the North Atlantic flight corridor and seasonally averaged, figured out a clear height dependency with high variability. This high variability will be further investigated with respect to its temporal evolution over 15 years of observations, to evaluate the possibility of determining trends or shifts in the distributions. In a next step, a coordinate transformation into the potential temperature (Theta) − equivalent latitude coordinate system will be conducted on the data to present in detail global (transport) processes which are relevant for the observed distributions over the North Atlantic, seasons of tropospheric-stratospheric exchange, and finally the potential pathways for these.

5.2 Seasonality and Time Series

The average state of the upper troposphere and lowermost stratosphere above the North Atlantic is described in the previous Chapter for different vertical layers, different timescales and species. Advantage but also disadvantage of an average state is its unknown freedom of variation with time. But to describe the present state of the atmosphere or to connect potential anthropogenic or natural events, e.g. of strong and persistent forest fires [Clark et al., 2015] or volcanic eruptions, to the present state, it is necessary to analyse that

unique and powerful data set on a continuous time scale. The selection criteria is similar to the analysis before.

Briefly summarised:

- limited to the area above the North Atlantic (40 - 60°N, 5 - 65°W),
- flight altitudes above the pressure level 280 hPa,
- sensor temperatures above the minimum calibration temperature of T_{sensor} = -40°C,
- ambient temperatures below -40°C to avoid supercooled water droplets,
- thermal tropopause as the natural reference to classify the data into seven 30 hPa thick layers.

The monthly state of the closest atmospheric layers around the tropopause layer, i.e. the highest upper tropospheric layer (UT1) with data between 15 and 45 hPa below the tropopause, and lowest lowermost stratospheric layer (LS1) with data between 15 and 45 hPa above the tropopause, is determined over the complete period between 1995 and 2009. $\mathrm{RH_{ice}}$, $\mathrm{H_2O}$ VMR and temperature are again the state variables of interest. In Figure 5.1, these state variables are presented as monthly time series of the median value (for the monthly average state), and the 25^{th} and 75^{th} percentiles for the variability within the month.

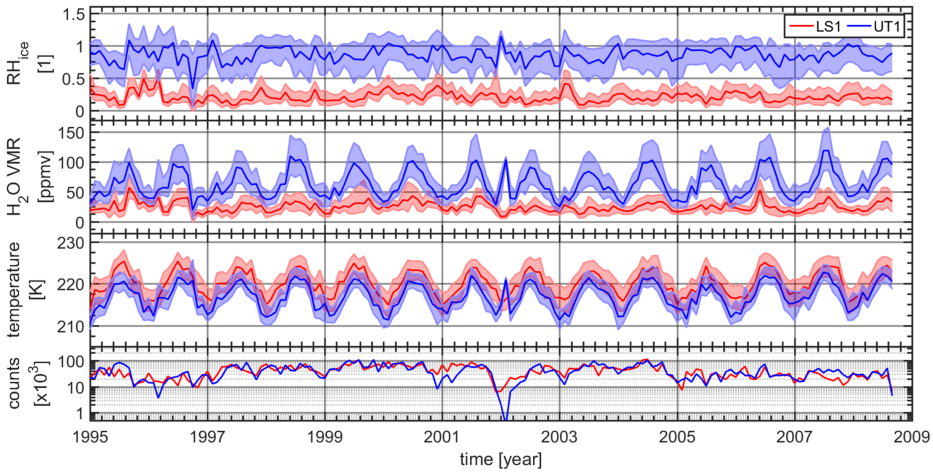

Figure 5.1: Time series of $\mathrm{RH_{ice}}$, $\mathrm{H_2O}$ VMR, temperature, and number of events for the highest upper tropospheric layer (UT1, blue) and the lowest lowermost stratospheric layer (LS1, red).

During the first 15 years of relative humidity and temperature in-situ measurements on passenger aircraft in the North Atlantic flight corridor, a clear separation between the UT and LS is found with clear layer specific water vapour distributions. The upper tropospheric layer time series describes a quasi-saturated layer with high variability over the years. In contrast, the lowermost stratospheric layer describes a subsaturated layer far below the 30% $\mathrm{RH_{ice}}$ level with small variation on the monthly and annual time scale.

The H_2O VMR time series suggests an annual cycle in the UT1 and gives a hint of a much less pronounced annual cycle in the LS1 layer. Also noticeable is the observation, that the annual cycles seem to be in phase for both decoupled atmospheric layers. The maximum water vapour VMR is according the Clausius Clapeyron relation which is controlled by the temperature. Therefore, the in-situ temperature time series is shown in the third row of Figure 5.1. Again, there is a clear annual cycle for both layers and in addition the cycle is clearly synchronised, i.e. in phase. Furthermore, the UT1 layer is slightly ($\sim$3 K) colder than the LS1 layer. It has to be noted, that the upper tropospheric data in the first months of 2002 cannot be taken into account since the number of data of less than 1000 measurements is below representativeness.

To get a first hint, whether there is a change or shift, respectively, in the temporal distribution, the means, i.e. the averages of median monthly values of the three main parameters RH_{ice}, H_2O VMR, and temperature are determined according to Equation 5.1.

$$\hat{s}_j = \frac{1}{n_j} \sum_{k=0}^{n_j-1} x_{k \cdot T+j} \tag{5.1}$$

(j: number of month, n_j: number of available years, T: length of the timescale, i.e. 12 months, x: monthly median in year $k+1$ of the parameter, and $\hat{s}_j$: average of the monthly median)

The results are presented quantitatively in Table 5.1 and graphically in Figure 5.2. The high interannual variability in the relative humidity distributions reduces the possibility to extract a significant annual cycle in both atmospheric layers. Nevertheless, the averaged RH_{ice} is highest in winter months (UT1:$\sim$90% RH_{ice}, LS1:$\sim$25% RH_{ice}) and has its lowermost stratospheric minimum in summer (LS1:$\sim$15% RH_{ice}), while the UT minimum is not well defined.

Table 5.1: Mean and standard deviation of median monthly values of the main parameter RH_{ice}, H_2O VMR, and temperature for the atmospheric layers UT1 and LS1 (see also Figure 5.2).

	RH_{ice} [1]		**H_2O VMR [ppmv]**		**temperature [K]**	
	UT1	LS1	UT1	LS1	UT1	LS1
Jan	0.91±0.13	0.25±0.07	39±9	18±5	213.3±1.5	216.0±1.1
Feb	0.93±0.09	0.25±0.08	44±18	18±5	213.7±2.4	216.5±0.9
Mar	0.88±0.09	0.26±0.10	48±9	23±6	214.7±2.0	217.7±1.2
Apr	0.86±0.10	0.18±0.04	50±8	20±3	215.7±0.8	219.1±0.8
May	0.88±0.09	0.20±0.06	61±9	24±6	216.9±1.0	220.2±1.0
Jun	0.83±0.11	0.17±0.06	85±14	29±10	219.9±1.1	222.9±0.9
Jul	0.79±0.08	0.14±0.05	95±13	28±7	221.1±1.1	224.1±0.7
Aug	0.83±0.09	0.17±0.04	95±13	32±7	220.9±0.7	223.6±1.0
Sep	0.85±0.09	0.18±0.06	82±9	32±10	219.5±1.1	222.9±1.0
Oct	0.79±0.16	0.20±0.08	61±15	26±11	218.3±1.2	221.1±1.4
Nov	0.91±0.07	0.23±0.06	52±7	24±6	215.7±1.3	219.0±0.8
Dec	0.84±0.12	0.25±0.10	39±6	21±6	213.9±1.1	217.6±1.3

s

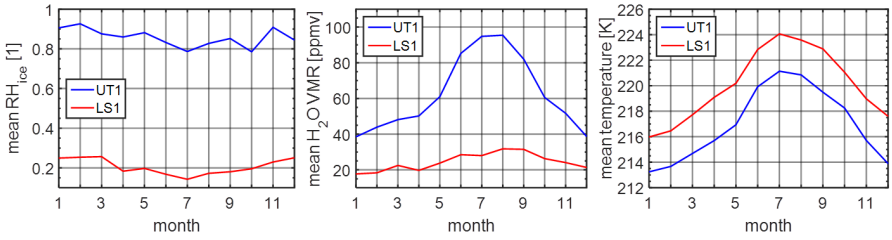

Figure 5.2: Mean of monthly median RH_{ice}, H_2O VMR, and temperature for the upper tropospheric layer UT1 and lowermost stratospheric layer LS1. Values and monthly variabilities can be read in Table 5.1.

Like the time series already suggested, the H_2O VMR is subject to a seasonal cycle in varying degrees. Thus, the January is the month with the smallest value of H_2O VMR in both atmospheric layers (UT1:∼40 ppmv, LS1:∼20 ppmv) and May seems to be the month in which the values start to increase. For the highest upper tropospheric layer, July and August are the months with the highest amount of H_2O VMR (95 ppmv). The lowermost stratospheric layer, by contrast, shows a shift of one month compared to the UT1 to reach its highest values of 32 ppmv in August and September. The distribution of the mean of monthly median temperatures shows an expected behaviour. A strong seasonal cycle in phase has its coldest month in January (UT1:∼213 K, LS1:∼216 K), and its warmest month in July (UT1:∼221 K, LS1:∼224 K).

In the next step, the time series of Figure 5.1 will be deseasonalised by subtracting the gained results of the averaged monthly medians. This application sets the distribution relative to its monthly baseline according to Equation 5.2, to enable an easier analysis of possible temporal drifts or shifts.

$$\hat{x}_{k \cdot T+j} = x_{k \cdot T+j} - \hat{s}_j \tag{5.2}$$

(j: number of month, T: length of the timescale, i.e. 12 months, x: monthly median in year $k+1$ of the parameter, $\hat{s}_j$: average of the monthly median, and $\hat{x}$: deseasonalised month of the parameter)

Figure 5.3 indicates that there is no significant shift or continuous drift observable for all variables and atmospheric layers. Smaller variations in the mean values are superimposed by the high monthly variability. Even though the first few years indicate too strong variabilities in the humidity and H_2O VMR which can not be explained by natural reasons, the approach of investigating the interannual variability could provide further improvements of knowledge.

More in-depth analyses of MOZAIC water vapour time series could prove this result of a non-detectable change, like it is also seen elsewhere [IPCC, 2013]. A necessary requirement for an extended study will be an additional improvement of the MOZAIC data, which is already in a good condition, by the so called In-Flight Calibration method (IFC method by Smit et al. [2008]), and an expansion to more than two-decades data set with the IAGOS data. The application of the IFC method is under development and will basically result in a reduction of the variation by cancellation of the internal instrumentation calibration

offset for every single flight. Nonetheless, due to the fact that the sign of the internal calibration offset drift is stochastically distributed, no changes in the mean results of the climatologies are expected.

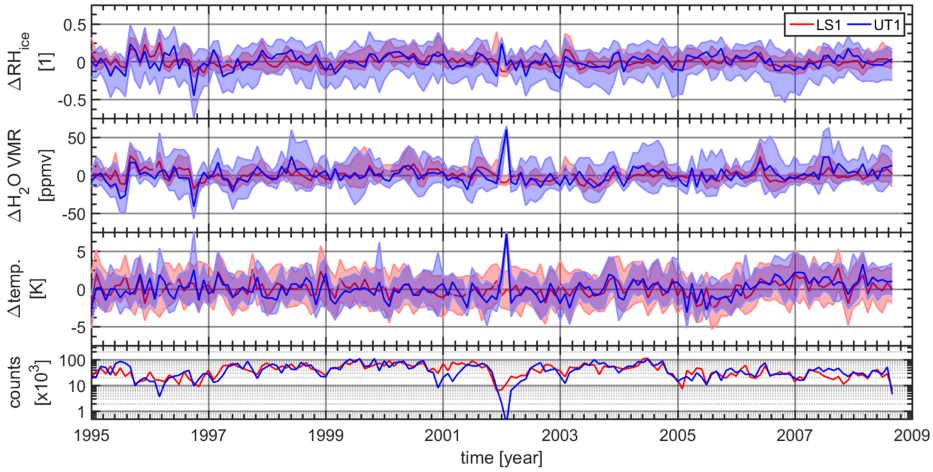

Figure 5.3: Deseasonalised time series of RH_{ice}, H_2O VMR, temperature, and number of events for the highest upper tropospheric layer (UT1, blue) and the lowest lowermost stratospheric layer (LS1, red).

5.3 Transport Processes and Pathways

Previous sections showed seasonal cycles and variations in H_2O VMR in both layers around the tropopause. This raises the question which transport processes and pathways allow especially the transport of H_2O VMR across the natural transport barrier, the tropopause, into the lowermost stratosphere. This question, however, is also the subject of other studies with different approaches. Duhnke et al. [1998] investigated upper tropospheric water vapour in the coordinate system of the north Polar jet stream and found a downward transport of dry stratospheric air through the tropopause on the cyclonic side and an upward transport of high water vapour mixing ratio into the stratosphere on the anticyclonic side of the jet stream. Zahn et al. [2014] subdivided the studies on H_2O budgets in the UTLS which are mainly summarised in Gettelman et al. [2011], into three categories: (1) the process studies which investigate the meteorological conditions and pathways for transfer events (e.g. Pan et al. [2007]); (2) event studies, especially the convective events which are considered as main driver for water vapour injection into the stratosphere (e.g. Anderson et al. [2012]); and (3) background studies which focus on large-scale distributions and budgets (e.g. Hoor et al. [2010], Luo et al. [2008], Ploeger et al. [2013]).

All of the mentioned investigations improved the knowledge on their topic significantly. However, all of them have their very own restrictions, e.g. aircraft campaigns are restricted on periodicity and horizontal resolution, balloon soundings present vertical information only over a certain station, or satellite measure-

ments are limited in the vertical resolution. Also this work started with an investigation on the large-scale distribution and budget analysis. But with the long-term, and high frequency of observations, high spatial resolution, as well as with the knowledge about the restriction to extratropical UTLS and sensor limitations in the deeper lower stratosphere, control processes and locations of pathways are investigated with the MOZAIC data set in the following which result in the determined H_2O distributions and budgets.

To identify the season of interest, where the transport of H_2O VMR into the stratosphere mainly occurs, thousands of MOZAIC flights in the North Atlantic flight corridor are processed to mean monthly median H_2O VMR vertical profiles. Similar to to the study by Zahn et al. [2014], the vertical profiles are scaled relative to the thermal tropopause in the unit of km, where the altitudes of the aircraft and thermal tropopause are calculated according to the barometric height formula [Berberan-Santos et al., 1997]:

$$p(z) \approx p_0 \cdot exp\left(\frac{-z}{H_0}\right) \tag{5.3}$$

with z the actual height, $p(z)$ the current pressure of the aircraft or thermal tropopause, respectively, $p_0 = 1013.25$ hPa the sea surface pressure, and the scale height $H_0 = 8.5$ km.

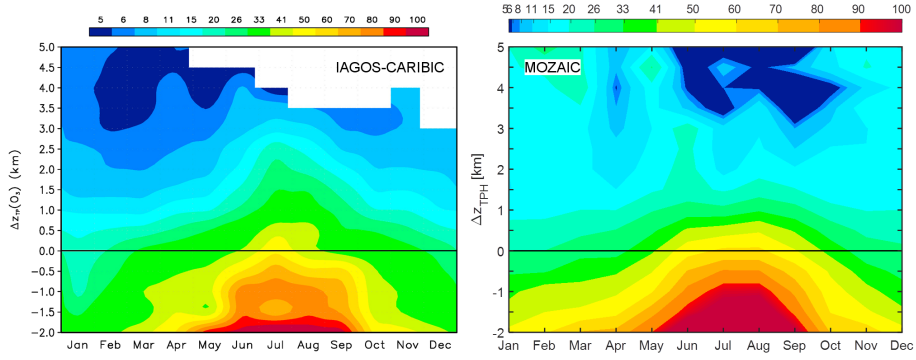

Figure 5.4: Seasonal variation of the mean monthly median H_2O VMR (in ppmv) in distance relative to the thermal tropopause height Δz_{TPH}. On the left (see Zahn et al. [2014], courtesy of American Geophysical Union), all IAGOS-CARIBIC H_2O data are collected north of 35°N and above the 280 hPa pressure level between May 2005 and May 2013. On the right, all MOZAIC H_2O data are collected in the North Atlantic flight corridor, between January 2000 and December 2008, and below the ambient temperature of -40°C to avoid contamination through supercooled liquid droplets. The variation of H_2O VMR over several orders of magnitude requires a nonlinear colour coding.

Figure 5.4 shows the seasonal variation of the mean monthly median H_2O VMR in distance to the thermal tropopause Δz_{TPH} of the IAGOS-CARIBIC data set (309 flights in 8 years in northern mid-latitudes; Zahn et al. [2014]) on the left and of the MOZAIC data set (approx. 10^5 flights in 9 years in the North Atlantic flight corridor) on the right. It is obvious by the high stratospheric values above the ∼5 ppmv background [Hegglin et al., 2009] that the MOZAIC Capacitive Hygrometer has its accuracy limitations when

measuring H_2O VMR at least 2 km above the thermal tropopause. Nevertheless, the long-term, continuous, homogeneous, and dense data set ensures a high statistical representativeness around the tropopause.

In both approaches, IAGOS-CARIBIC and MOZAIC, the upper troposphere is found to be moister during summer months than during winter months, what can be also observed up to the lowermost stratosphere. The amount of H_2O VMR in winter and spring months can be explained by the seasonal cycle of temperature in the UTLS. Thus, it adjusts high relative humidity in the upper troposphere (Figure 5.5 on the left) and a strong vertical gradient in the temperature relative to the layer in the vicinity of the tropopause height (TPH) (Figure 5.5 on the right) for both layers, UT and LS, respectively. It implies a downward regulation of H_2O VMR according to the Clausius Clapeyron relation with additional strong stability (UT: more than 7 K at 3 km to the TPH, and LS: more than 14 K at 4 km to the TPH) to neglect vertical transport into the LS.

Summer and parts of fall months, in contrast, show vertical H_2O VMR profiles which can not be fully explained by the seasonal cycle of the temperature. More or less constant RH_{ice} conditions with 70 - 80% in the upper troposphere between May and October, and a seasonal cycle in the temperature (see Fig. 5.2) with the highest temperature in July suggest an additional process to regulate the H_2O VMR in the UTLS. Reduced stability in the UT (ΔTemp $\approx$ 5 K at 3 km to the TPH) and in the LS (ΔTemp $\approx$ 11 K at 4 km to the TPH) let assume a mixing of humid tropospheric air masses into the lowermost stratosphere with H_2O VMR values of up to 50 ppmv.

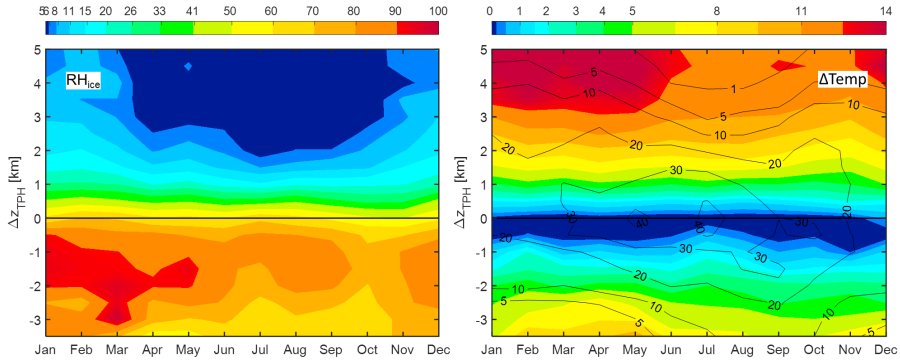

Figure 5.5: Seasonal variation of the mean monthly median RH_{ice} (left; in %) and vertical temperature difference to the tropopause layer temperature ΔTemp (right; in K) in distance relative to the thermal tropopause height Δz_{TPH}. All MOZAIC RH_{ice} and temperature data are collected as it was in Figure 5.4. The different variation range in UT and LS requires a nonlinear colour coding. Thin lines with numbers representing the sample statistics in hours per month, whereas the monthly sum varies between 200 hours in December and 330 hours in July.

It has to be mentioned that a flight more than 3 km above the thermal tropopause is highly dependent on the large-scale dynamics, especially for the increased summer tropopause heights. This behaviour reduces

the sample statistics in the extremes, i.e. the highest lowermost stratospheric heights is less frequently probed in summer with less than 1 hour of measurements per month than in winter with more than 5 hours. Similar is true for the lowest upper tropospheric heights where winter is less frequently probed with less than 5 hours of measurements per month than summer with more than 10 sample hours.

Gettelman et al. [2011] described in the review about extratropical upper troposphere and lower stratosphere, that the North Atlantic is one of the preferred regions for stratosphere-troposphere exchange. The drivers for in-mixing in the first 2 - 3 km above the tropopause are mainly shallow, fast two-way cross-tropopause mixing (active around the year), quasi-isentropic in-mixing from the tropical tropopause layer around the subtropical jet (active in summer and early autumn), and localized sporadic deep convection (active mainly in summer). Thus, the MOZAIC data set also observes seasons of air mass exchange, it is used in the following section to identify and to confirm the UTLS water vapour pathways over the North Atlantic.

5.3.1 Identification of UTLS Water Vapour Transport Pathways

After the preferred seasons for in-mixing of tropospheric water vapour into the lowermost stratosphere have been identified, the locations of pathways for the vertical in-mixing will be determined in this section. To identify the transport pathway for water vapour from the UT into the LS, the potential temperature (Theta) and the potential vorticity (PV)-based Equivalent latitude [Butchart and Remsberg, 1986] are used as a tool for describing the latitudinal distribution of H_2O VMR and RH_{ice} relative to the tropopause.

Before the results are presented, a short introduction of the coordinate transformation is necessary. The vertical motion of gaseous or liquid air parcels can be described in a good approximation by adiabatic changes. Thus, atmospheric air parcels are moving in the first approximation on surfaces with equal potential temperature (Theta). These surfaces are called isentropes.

If we try to investigate UTLS exchange processes in the mid-latitudes with the goal to assign them to distinct geometric regions (i.e. latitude, longitude, and altitude), this would inevitably lead to mixtures of different atmospheric air mass types, e.g. in the vicinity of the jetstream [Duhnke et al., 1998]. This jetstream can be associated with the tropopause on that height. As it is known, the jetstream flows in meanders due to Rossby waves and as consequence, the ”border” between troposphere and stratosphere also shows zonal asymmetries. The sketch in Figure 5.6 by Hegglin et al. [2006] describes the homogenisation of air masses on a given isentrope. The grey area can be assumed as stratospheric air masses and the contour line of this grey area as the jetstream or dynamical tropopause with the potential vorticity PV $= 2$ PVU. The chemical and dynamical fingerprint of the grey, separately circled area, e.g. a cut off low, belongs to the stratospheric surface but would be considered to the analysis as tropospheric air masses on a conventional latitudinal scale.

The new coordinate system shifts all air parcels with the same potential vorticity on the same potential temperature to the same equivalent latitude for all longitudes, i.e. to its origin based on the timescale of adiabatic processes regardless of their meridional displacement. To do that, the total surface area of the grey

stratospheric air masses is calculated and the radius (= Equivalent latitude, red contour line in Figure 5.6) of the idealised circle centred around the pole is determined.

The calculation is conducted according to the formula

$$\phi_e(PV_i, \theta_j) = \sin^{-1}\left(1 - \frac{A(PV_i, \theta_j)}{2\pi R^2}\right), \tag{5.4}$$

where $\phi_e(PV_i, \theta_j)$ is the Equivalent latitude for a given PV-value PV_i on a given isentrope θ_j, and R is the Earth's radius. The surface area A of the idealised circle, which is centred around the pole, is based on the area covered by PV-values greater and equal PV_i on the given isentrope [Pan et al., 2012].

It has to be mentioned that the approximation of fully adiabatic changes is mostly met by the stratosphere, but there are concerns in the representation of the troposphere, e.g. during cloud formation processes. Thus, the potential temperature (Theta) and Equivalent latitude coordinates do not represent UT and LS equally. Nevertheless, changes in the chemical composition for stratospheric air masses can be traced to in-mixing processes.

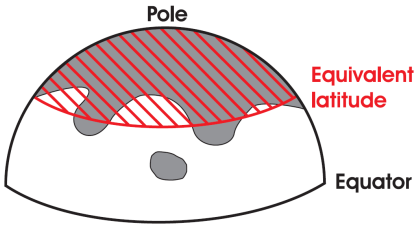

Figure 5.6: Illustration by Hegglin et al. [2006, courtesy of European Geosciences Union] describing the coordinate transformation on a given isentrope. The PV-contour surrounds a grey area with even higher PV-values. The sum of the grey surfaces is transformed to the idealised circle centred around the pole with radius of the Equivalent latitude (red hatched area). All dynamically equal air parcels (PV-contour) on the given isentrope are thereby shifted to the equal latitude, regardless of the longitude.

For this purpose, the available ECMWF ERA-Interim meteorological fields are used. These reanalysis data assimilate measurements, based on the Integrated Forecast System (IFS) in the available release Cy31r2 [Dee et al., 2011, Simmons et al., 2014]. Furthermore, the ERA-Interim data have a time interval of 6 h with a horizontal resolution of 1°x1° in longitude/latitude (T255L60). In a further step, the data are interpolated linearly in latitude, longitude, atmospheric pressure, and time to the aircraft location to obtain amongst other things the potential vorticity. Beforehand determined equivalent latitude lookup tables in a 24 h resolution are further used to obtain the new latitudinal coordinate in dependency of the current potential vorticity and potential temperature.

The results presenting the seasonally grouped measurements of O_3, RH_{ice}, H_2O VMR, and temperature will be plotted in the potential temperature (Theta) − equivalent latitude coordinate system. For all distributions shown below, the mean of the data was calculated, which is restricted to the North Atlantic flight

corridor (30 - 60°N, 5 - 65°W at flight altitudes less than 280 hPa) and further binned on a 2.5° equivalent latitude / 2.5 K potential temperature grid.

As a kind of evaluation of the coordinate transformation and to demonstrate the power of this technique, the MOZAIC ozone distribution will be analysed. Given the fact that ozone is mainly produced in the tropical stratosphere and has a lifetime in the mid-latitudinal lower stratosphere of about 1 year [Solomon et al., 1985], ozone can be considered as a passive tracer in the lowermost stratosphere. Figure 5.7 shows that the ozone isopleths (colour bar) follow the PV contour lines (black lines) all year round. This coherence is pronounced strongly in spring and fall seasons, when the ozone isopleth still follows the PV contour of 1 PVU.

The highest LS ozone values of more than 600 ppbv are observed in the higher latitudes (above 40°N) and upper part (above 345 K) of the lowermost stratosphere in spring which confirms and extends the results of Engel et al. [2006]. A reasonable explanation is given by the increased diabatic downward transport of an enhanced Brewer-Dobson circulation [Sprenger and Wernli, 2003] beginning in late winter, strengthen in spring, and finally weakening in summer. Strongest impact of tropospheric ozone (isopleths below 120 ppbv; Thouret et al. [2006]) is visible between 50° and 60°N, and at about 325 K in summer and fall. Sawa et al. [2008] explained the tropospheric ozone in the lower stratosphere with fast meridional transport on isentropic surfaces around the subtropical tropopause in summer, while Grise et al. [2010] supports that assumption by finding a poorly defined static stability, i.e. poorly defined tropopause inversion layer, near the southern edge of the North Atlantic flight corridor.

The highest upper tropospheric ozone values are observed in summer when the increased photochemistry and frequent stratosphere-troposphere exchanges processes occur [Cooper et al., 2005], such as Rossby wave breaking.

Winter season in contrast, shows a significantly stronger PV-gradient in the stratosphere due to the influence of the Brewer-Dobson circulation [Sawa et al., 2008] which leads to suppression of stratosphere-troposphere exchange with resulting ozone values below 60 ppbv.

After describing the principle motion of air parcels with the tracer ozone, the focus is on the distributions of the short-living variables H_2O VMR and RH_{ice}. The later one is shown in Figure 5.8(a) with a principle behaviour for all seasons: RH_{ice} isopleths are following the isentropes in the UT and above 350 K in both spheres. But by entering the lowermost stratosphere the relative humidity distribution is tilted and follows the PV contour lines with exception of summer when a quasi isentropic transport can be seen in the area of 50°N and below 350 K.

As previously shown in Figure 5.5(a) the upper troposphere has no significant minimum and its seasonal maximum relative humidity in winter when saturation is most likely in the complete UT pattern. The region where RH_{ice} close to saturation enters the stratosphere is located between 30° and 40°N. Moreover, upper tropospheric humidity in the tropical tropopause layer (TTL; Fueglistaler et al. [2009]), i.e. above 350 K and below 25°N, is very dry with RH_{ice} below 0.3. Here, diabatic effects seem to be the regulating mechanisms since ozone VMR stays in tropospheric dimensions.

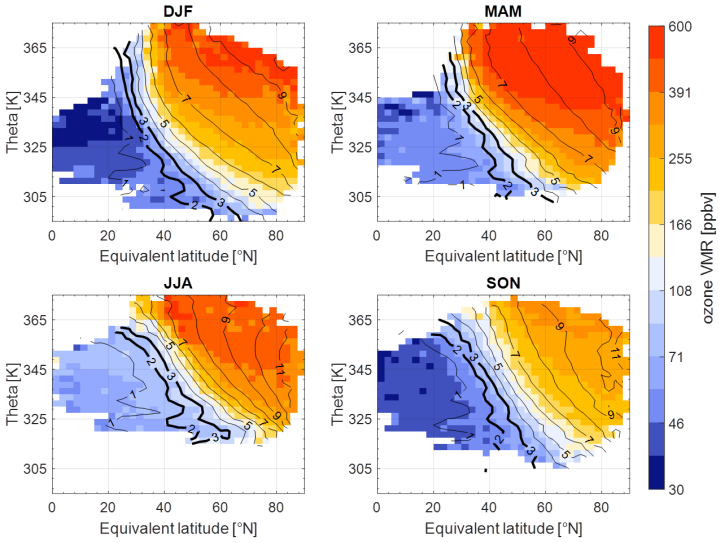

Figure 5.7: Potential temperature (Theta) − Equivalent latitude plot of all data collected above the 280 hPa pressure level and polewards from 30°N over the North Atlantic, differentiated by season. Colour coding: median of seasonal median ozone VMR (colour bar). Black lines with numbers: mean potential vorticity (PV in PVU) isocontour lines (isopleths) during sampling. The dynamical tropopause PV threshold values (2 and 3 PVU) are highlighted by the bold black lines.

The amount of H_2O VMR (see Fig. 5.8(b)) above the dynamical tropopause (2 - 3 PVU) is dependent on the influence by the Brewer-Dobson circulation. With increasing influence in winter and during its maximum expression in spring, tropospheric-stratospheric exchange is suppressed and the amount of water vapour is restricted by the dehydration at the Lagrangian Dry Point in the TTL [Fueglistaler et al., 2005, Liu et al., 2010]. However, in principle the LS water vapour follows the PV isopleths with weak in-mixing detected in the nearest environment of the tropopause region with strongest effect at 320 K and 40 - 60°N throughout the year (see also Zahn et al. [2014]).

Especially noticeable is the transport pattern in summer when the moister UT air masses perform a quasi isentropic transport towards the pole into the deeper LS (PV ∼7 PVU) by reaching up to 60 ppmv H_2O VMR at 325 K and 80°N. This summer troposphere-stratosphere-transport confirms the result by, e.g. Spang et al. [2015] who analysed water vapour observations of the Cryogenic Infrared Spectrometers and Telescopes for the Atmosphere (CRISTA) satellite instrument. Therein they found indications for considerable isentropic flux of moister air at approx. 350 K from the UT into the extratropical lowermost stratosphere. They also concluded that the process is triggered by Rossby wave breaking events in the northern hemispheric subtropical jet region.

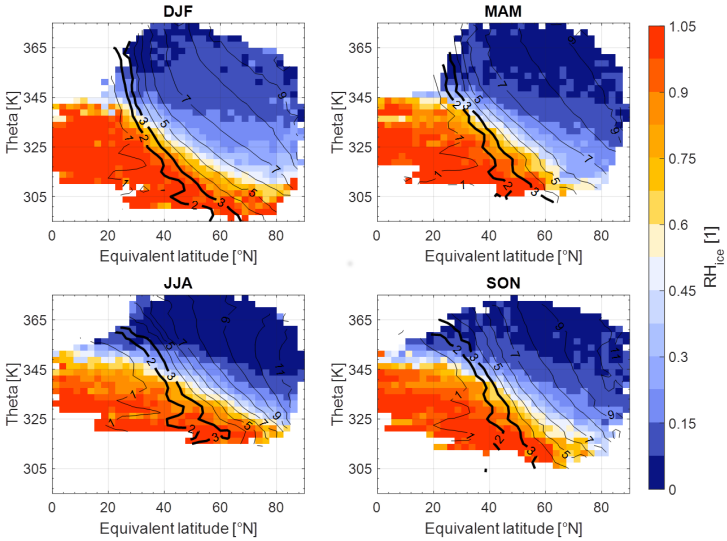

(a) RH_{ice}

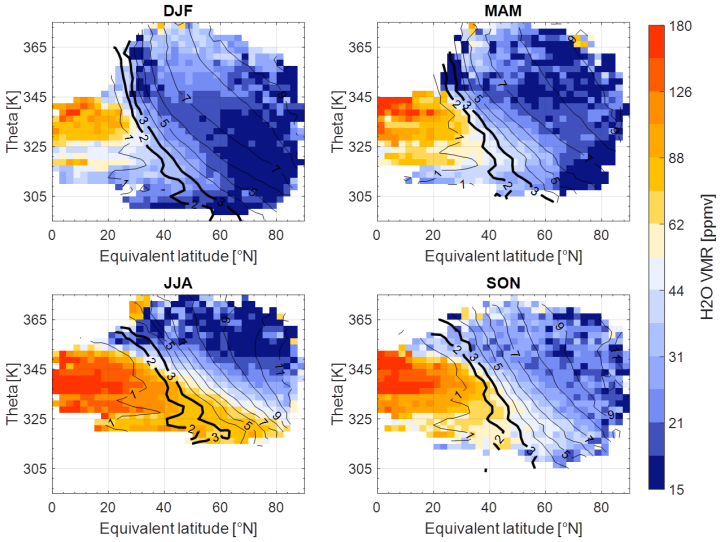

(b) H_2O VMR

Figure 5.8: Potential temperature (Theta) – Equivalent latitude plot as in Figure 5.7. Colour coding: median of seasonal median (a) RH_{ice} and (b) H_2O VMR (colour bar).

Through the fact that with assuming local transport of saturated air mass into the extratropical lowermost stratosphere, the dehydration approach with the significant warmer tropopause region (see Fig. 5.9) yields the observed amount of H_2O VMR.

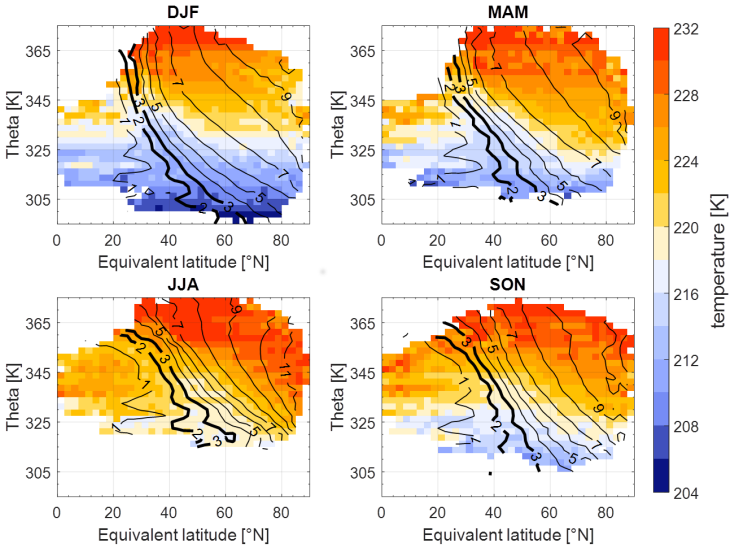

Figure 5.9: Similar to Figure 5.7, but with median of seasonal median temperature (colour bar) as colour coding.

5.4 Conclusions

The previous Chapter 4 presented the average state of seven atmospheric layers centred around the tropopause in the North Atlantic flight corridor for the three humidity dependent variables temperature, water vapour VMR, and relative humidity in the timescales of mean seasons and overall mean. In this chapter the time resolution is increased to monthly distributions for the first layer above and below the tropopause layer to analyse the evolution of the distributions.

After the time series of RH_{ice} revealed a stochastic variability in the median monthly distribution without any dependence to the annual cycle for both layers, temperature and H_2O VMR distribution showed a clear seasonal cycle which is in phase for both layers. To deseasonalyse the time series the monthly mean values over the 15 years have been extracted. The relative humidity monthly distribution confirmed the observation of a more or less constant state ($RH_{ice} \approx 90\%$ in the UT, $RH_{ice} \approx 20\%$ in the LS) with high variability ($\Delta RH_{ice} \approx 10\%$ in the UT, $\Delta RH_{ice} \approx 8\%$ in the LS). Monthly temperature and moister distributions also confirm the annual cycle with the warmest month in July with the highest H_2O VMR in August, and the

coldest month with the fewest H_2O VMR in January. It appears that the applied deseasonalisation could not offer any trend which is enhanced by the high monthly variabilities of, e.g. up to 50% in RH_{ice}. This high variability in the stratosphere will be slightly reduced in the future, when the adapted In-Flight Correction based on Smit et al. [2008] is applied, but nevertheless, the vertical transport in the troposphere is the main driver for the discontinuity.

These transport processes and pathways in the upper troposphere and between troposphere and stratosphere were in the focus of the following studies. In the winter months, a regulation of the humidity and moister by the temperature is expected according to the Clausius Clapeyron equation because the strong vertical temperature gradients in the UT implies a high stability and with that a reduced possibility of vertical motion. This assumption is supported by the lowest upper tropospheric H_2O VMR values and RH_{ice} values around saturation.

Weakened vertical temperature gradient in summer in the UT in addition with highest H_2O VMR which also intrusions the lowermost stratosphere let assume strong vertical transport with overshooting into the stratosphere. Due to RH_{ice} values clearly below saturation neglects the assumption of convective intrusion into the stratosphere and needs further investigations to describe the observed troposphere-stratosphere exchange.

To do so, a coordinate transformation is conducted from geographic to equivalent latitude according to Butchart and Remsberg [1986]. The possibility of the equivalent latitude and potential temperature coordinate system is that it can be regarded as tropopause-following since it follows the meridional excursions of PV-contours induced by Rossby and smaller scale waves. Trace gas mixing ratios, which are displayed in this coordinate system, therefore appear according to their distance to the local tropopause on a given isentropic surface, which therefore reduces the scatter obtained in a geometric non-tropopause-following coordinate system.

Results for RH_{ice} show a principle behaviour for all four seasons. RH_{ice} isopleths are following the isentropes in the UT and above 350 K in the UTLS. By entering the lowermost stratosphere the relative humidity distribution is tilted and follows the PV contour lines with the exception of summer (JJA) when a quasi isentropic transport can be seen near 50°N and below 350 K.

While ozone and H_2O VMR distributions in winter (DJF) indicate a strict separation of troposphere and stratosphere due to the greatest influence of the Brewer-Dobson circulation which suppresses exchanges with subsided deep stratospheric air masses (ozone VMR above 600 ppbv), this separation weakens with weakened influence of the Brewer-Dobson circulation. In principle, shallow mixing of air masses is recognised throughout the year in the surrounding of the tropopause. Especially noticeable is the summer season when moister UT air masses perform isentropic transport towards the pole into the LS which might be triggered by Rossby wave breaking events in the northern hemispheric subtropical jet region.

CHAPTER 6

ICE SUPERSATURATED REGIONS AND CIRRUS CLOUDS

6.1 Introduction

The IPCC Report 2013 stated that the radiative impact of cirrus clouds is one of the largest sources of uncertainty in the Earths energy balance, and even fundamental details of ice cloud processes are still poorly understood. Model studies demonstrate that the magnitude of the net effect depend significant on microphysical properties of ice crystals [Wendisch et al., 2005, 2007], and ice supersaturation in clouds [Fusina et al., 2007, Gettelman et al., 2012, IPCC, 2013]. Even the sign of the net effect of natural cirrus is uncertain, although Chen et al. [2000] assume a net warming effect. Besides its close link to cirrus formation and lifecycle, understanding the processes which control the distribution of water vapour is of high relevance for predicting future climate [Müller et al., 2016, Riese et al., 2012]. Upper tropospheric humidity is also relevant for the formation of aviation-induced cirrus, which form in ice supersaturated regions [Irvine and Shine, 2015].

One particular focus of current research on cirrus concerns the distribution of relative humidity with respect to ice (RH_{ice}) in clear sky and in cirrus clouds since ice supersaturation ($RH_{ice} > 100\%$) is the relevant requirement for ice nucleation (homogeneous, heterogeneous; Koop et al. [2000], Krämer et al. [2016]) and further cloud evolution.

6.2 Ice Supersaturated Regions

As measurements in the UTLS show, air masses with RH_{ice} exceeding 100%, so-called ice supersaturated regions (ISSR, see, e.g. Gierens et al. [1999]), occur quite frequently in the tropopause region (e.g. Helten et al. [1998], Lamquin et al. [2012], Zöger et al. [1999]) with sharp temperature changes [Birner et al., 2002], and preferably in regions with upwind and divergent airflow [Gierens and Brinkop, 2012]. Spichtinger et al. [2003b] used satellite measurements from the Microwave Limb Sounder (MLS) and showed very low ISSR occurrence frequencies with 2 - 3% at 215 hPa. However, with the reduced detection sensitivity by a factor of 0.2, explained with the limited vertical resolution ($\sim$3 km) and the integration along the line of sight ($\sim$200 km), the results matched the occurrence frequency of 11 - 15% in northern mid-latitudes by Gierens et al. [2000]. More recent research by Lamquin et al. [2012] used data from the newer satellite instrument AIRS (Atmospheric Infrared Sounder) and obtained significantly larger frequencies near the mid-latitude tropopause region of 20 - 30%. They also found indications for ISSR in the mid-latitudes zonal mean tropopause region itself and above with occurrence frequencies of 10 - 20%.

Spichtinger and Leschner [2016] determined the properties of ISSRs by evaluating global MOZAIC data between 1995 to 1999 and found a typical ISSR pathlength of 150 km with smaller ISSRs in the tropics. They also stated a strong seasonal cycle with most extratropical ISSRs in summer, and a shift in the seasonal cycle between troposphere and the tropopause region. The reported high variability of RH_{ice} could be explained by simulating vertical upward motion and adiabatic processes.

In the following, the extension of the MOZAIC data set to the years 1995 to 2009 improves the robustness of the evaluation of the ISSRs in the North Atlantic flight corridor with the restrictions introduced in Section 5.2. During this evaluation, a similar but, nevertheless, quantitative difference in the vertical distribution of the seasonal fraction of ISSR develops depending on the tropopause definition (Figure 6.1 and Table 6.2). The median seasonal fraction of ISSR in the upper troposphere increases with height from 29 to 34% for the thermal tropopause criteria. Using the dynamical tropopause approach results in a enhancement of 6% in each layer. Also the high seasonal variability of about 10% in the troposphere is covered by both approaches and is highest (12 and 14%, respectively) in the lowest tropospheric layer. With a deviation of 11% in the seasonal fraction, the tropopause layer shows the largest difference between the thermal (20%) and dynamical (31%) tropopause.

Table 6.1: Mean and standard deviation of seasonal fraction of ice supersaturated regions (ISSR) for the seven vertical layers distributed around the thermal (top row) and dynamical (bottom row) tropopause.

p - p(TPH) [hPa]	**-90**	**-60**	**-30**	**0**	**30**	**60**	**90**
fraction of ISSR (therm. TPH) [%]	0.0±0.1	0.1±0.3	1.5±1.1	20.0±6.5	33.9±9.0	31.4±9.2	29.1±12.1
fraction of ISSR (dyn. TPH) [%]	0.2±0.5	0.7±1.1	8.4±4.4	30.7±9.4	39.9±10.0	37.7±10.7	35.5±14.2

Whereas the lowermost stratospheric fractions of ISSR are statistically insignificant (less than 2% with a maximum variability of 1%) for the thermal tropopause, the dynamical approach shows the most prominent deviation with a significant seasonal fraction of 8% ISSR in the first LS layer (30 $\pm$ 15 hPa above the dynamical tropopause). Both results are comparable with those from regular balloon launches over Lindenberg, Germany (52.22°N, 14.12°E) with 6.2% relative occurrence [Spichtinger et al., 2003a] and 2% relative occurrence for northern mid-latitudes from an earlier part MOZAIC measurements by Gierens et al. [1999].

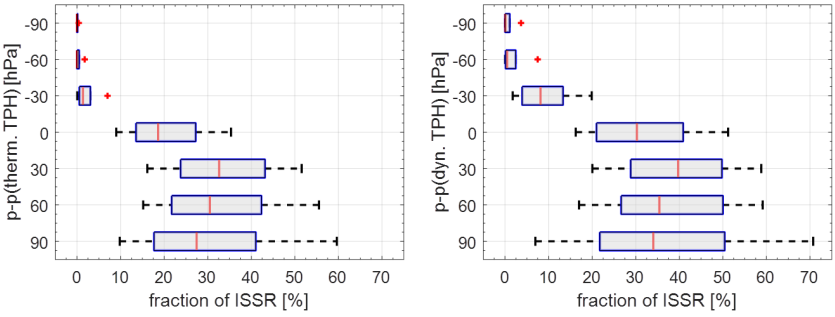

Figure 6.1: Box and whisker plot [1, 25, 50, 75, and 99 percentile] for seasonal fraction of ice supersaturated regions (ISSR) for the seven vertical layers distributed around the thermal (left panel) and dynamical (right panel) tropopause in the North Atlantic flight corridor. Statistical values can be read in Table 6.2.

The properties of ISSRs, the comparison between ISSR (box and whisker plots) and non-ISSR (thin red lines) air masses as well as the comparison between the results received with the thermal (left panel) and dynamical (right panel) tropopause definitions are presented in Figure 6.2. In general, ice supersaturated regions are colder than their subsaturated counterparts. The difference is low in the UT with approx. 1 - 2 K what is comparable with the 2 K at 215 hPa by MLS satellite measurements [Spichtinger et al., 2003b], and increases in the stratosphere to $\sim$5 K. The 3 - 4 K colder tropospheric ISSRs reported by Gierens et al. [1999] are comparable with the temperature difference in the 30 hPa thick tropopause layer.

The vertical ozone VMR distribution reveals a major discrepancy between both tropopause definitions. While the vertical distributions show similar behaviour in the troposphere and the tropopause layer with less than 20 ppbv fewer ozone VMR in ISSR than in the non-ISSR, the stratospheric ozone VMR increases to stratospheric values (>300 ppbv) for the thermal tropopause criteria which is in contrast to the rather tropospheric ozone VMR of about 120 ppbv for the dynamical approach.

Figure 6.2 also shows a similar behaviour for the H_2O VMR vertical distribution for ISSR and non-ISSR data with exponentially decreasing humidity until the tropopause layer. However, while it further decreases for the non-ISSRs, the water vapour VMR increases with height to tropospheric values of about 10 ppmv in ISSRs. The increase of H_2O VMR in the upper tropospheric ISSR is comparable with the results of the

MLS measurements by the factor of 3, while Gierens et al. [1999] reported of only 50% more moister in their ISSRs compared to non-ISSRs.

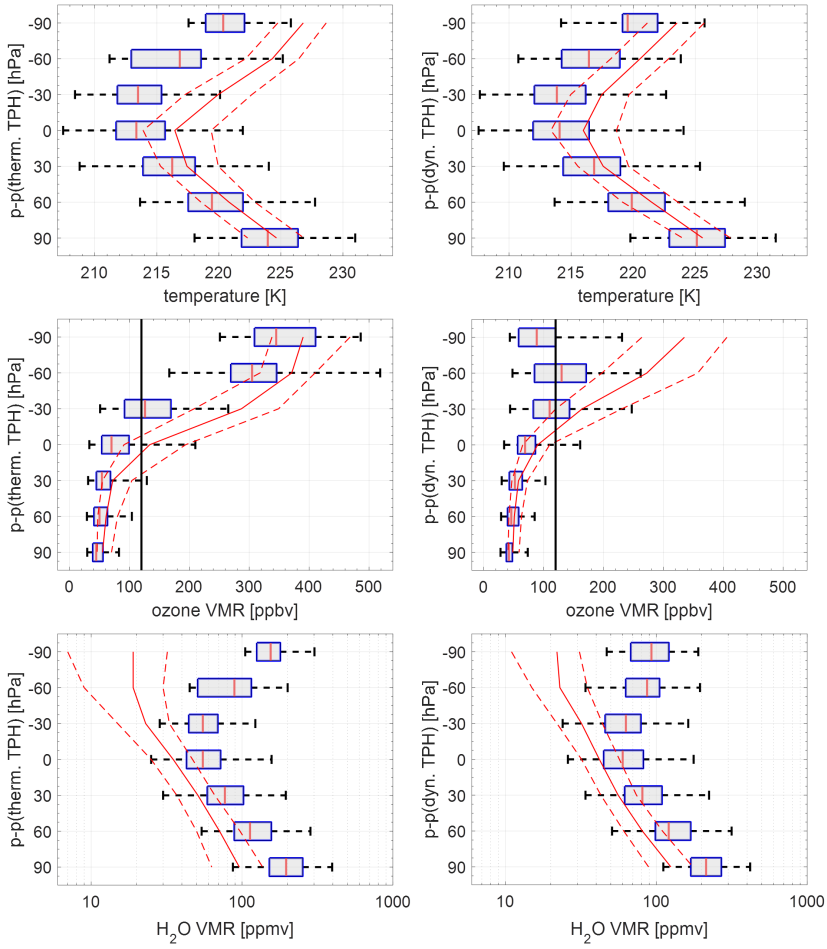

Figure 6.2: Vertical distribution of temperature, ozone VMR, and H_2O VMR (top-down) for ice supersaturated regions (ISSR) relative to the thermal (left panel) or dynamical (right panel) tropopause, respectively. The box and whisker plots represent the median of seasonal percentiles [1, 25, 50, 75, and 99]. For direct comparison to the non-ISSR distributions, the red lines show the according median (solid line) and 25^{th} / 75^{th} percentiles (dashed lines) of the non-ISSR data. The black vertical line in the ozone distributions represents the 120 ppbv threshold value for the chemical tropopause by Thouret et al. [2006].

The result of colder, moister ISSR air masses with less ozone VMR indicates that uplifting is an important source for supersaturation in the upper troposphere. Nevertheless, the cold temperatures for ISSR could also be explained with an increased probability to measure ISSR in winter where the coldest temperatures are observed (Figure 5.2 in Chapter 5).

Besides the different properties of ISSR and non-ISSR air masses, the interannual variation of ISSR occurrence is of scientific interest to assume the amount of cirrus cloud coverage. It has to be mentioned, that there is no direct measurement for a cloud index in the MOZAIC data set, which yields in humidity statistics containing signatures of cloudy and clear sky air masses. However, since ice supersaturation can be assumed as an indicator for cirrus cloud occurrence [Ovarlez et al., 2002, Spichtinger et al., 2004], Figure 6.3 is used to present the monthly probability of upper tropospheric ISSR and cirrus occurrence in the North Atlantic flight corridor, respectively. When following the black and bold ice saturation contour line (RH_{ice} = 100%), the high monthly variability in the RH_{ice} distribution (Figure 6.3) suggests a seasonal cycle with an increased ISSR probability, i.e. lower cumulated probability of subsaturated air masses, in the winter months. The bulge of the months show a probability for non-ISSR of 50 - 80% and thus, a monthly probability for cirrus clouds of 20 - 50%. These values for possible cirrus cloud occurrence are in accordance to the climatologies of high cloud amounts offered by satellite records [Sassen et al., 2008, Stubenrauch et al., 2010].

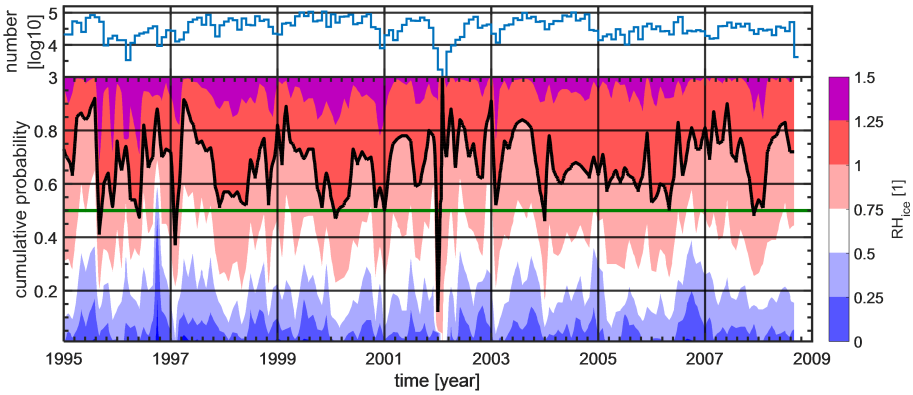

Figure 6.3: Time series of RH_{ice} cumulative probability for the highest upper tropospheric layer (UT1) in the North Atlantic flight corridor. The green line serves as a guide for the monthly median (cumulative probability = 0.5) and the black line is the RH_{ice} saturation contour. The noticeable peak in winter 2002 is due to too few measurements which is represented with the number of data time series in the top panel.

A completely new approach to separate the observed humidity measurements into in-cloud and clear sky data is possible in the MOZAIC successor IAGOS with the first installation of a cloud index measurement instrument in 2011. The following section serves as example for the power of such additional information

for humidity studies in the UTLS with a case study based on the first available 15 months of a combined data set with humidity and ice crystal number concentrations.

6.3 Humidity Distribution inside and outside of Cirrus Clouds

This section is partly based on the manuscript "Upper tropospheric water vapour and its interaction with cirrus clouds as seen from IAGOS long-term routine in-situ observations" by A. Petzold, M. Krämer, P. Neis, C. Rolf, S. Rohs, F. Berkes, H. G. J. Smit, M. Gallagher, K. Beswick, G. Lloyd, D. Baumgardner, P. Spichtinger, P. Nédélec, V. Ebert, B. Buchholz, M. Riese, and A. Wahner, published in Faraday Discussions as Petzold et al. [2017].

The link between ice supersaturation and cirrus clouds is an important topic in the research to understand and to simulate the lifecycle and properties of ice water clouds. Lamquin et al. [2012] postulated, for example, that cirrus clouds form where ice supersaturation takes place by evaluating a combined data set of humidity measurements, i.e. MOZAIC in-situ and AIRS remote sensing measurements, and CALIOP satellite cirrus cloud measurements. Spichtinger et al. [2004] analysed on a statistically basis the relative humidity distributions in clear sky and in-cloud with the result of nearly symmetric humidity distributions in relatively warm cirrus (warmer than -40°C) and skewed to higher humidities in colder clouds.

With the integration of the Backscatter Cloud Probe (BCP; Beswick et al. [2014, 2015]) into the IAGOS instrumentation in 2011 and the in-depth evaluation of the IAGOS Capacitive Hygrometer (ICH; see Chapter 3), a unique global-scale data set of distinguishable observations between in-cloud and clear sky measurements is developing.

In extension to the previously conducted analysis which used MOZAIC measurements in the North Atlantic flight corridor between 1995 and 2009, the analysis of the RH_{ice} - N_{ice} (ice crystal number concentration) observations uses the first available 15 months of IAGOS-CORE measurements from July 2014 to October 2015.

Both sensors measure directly in the air passing by outside the aircraft skin. The optical particle spectrometer BCP detects the light scattered in a backward cone by individual hydrometeors of particle sizse ranging from 5 to 75 μm in diameter that pass through the centre of focus of a 650 nm wavelength beam generated by a diode laser. The fraction of light that is scattered backward is collected by a set of lenses, whereas the detected light pulses serve as count signals for cloud particles passing through the laser sampling area. With the true air speed of the aircraft the cloud particle number concentration is then calculated. Samples with $N_{ice} \geq 0.015$ cm^{-3} are categorised as "in-cloud" or cirrus, respectively, whereas samples below 0.01 cm^{-3} are categorised as cloud-free observations. The samples within these categories are indeterminate events and can not be clearly assigned to a category because of their high sampling uncertainty of more than 50% [Beswick et al., 2015].

The data, which are selected for this study data are based on a set of criteria which ensure the focus of possible cirrus cloud analysis in the upper troposphere. For that, the pressure is limited to (1) $p < 350$ hPa

to limit data to cruise altitude above 8.1 km at standard atmosphere conditions; (2) the maximum ambient temperature is 233 K due to the temperature threshold for spontaneous freezing of water droplets to exclude data during coexistence of supercooled liquid water droplets; and (3) the minimum sensor temperature is 233 K according to the minimum ICH sensor calibration temperature (see Chapter 2). To restrict the data to the upper troposphere, the thermal tropopause pressure based on the WMO definition [WMO, 1957] is extracted for the flight track from the 6-hourly output from the ECMWF ERA-Interim Reanalysis according to Kunz et al. [2014].

Since humidity sensors were partially operated significantly longer than the planned exchange after two months, a baseline shift in the sensors offset was observed. The humidity measurements have been corrected with a modified In-Flight Calibration (IFC) method based on the published method by Smit et al. [2008]. A detailed description of the applied method to correct the humidity data can be read in Chapter 1.4.

Applying this IFC method on the 2014/2015 data, however, requires an evaluation against the MOZAIC data set from 2000 to 2009 (Figure 6.4). This comparison of the RH_{ice} probability distribution functions (PDF) shows that the two years of IAGOS data fit well into the range of the MOZAIC data set from 2000 to 2009. Deviations and the spread in the MOZAIC envelope can be explained with the variable annual amount of stratospheric flights. Nevertheless, the dry peak at 5% RH_{ice} and the turning point at about 105 - 110% RH_{ice} is detectable in all distributions which indicates the successful offset correction.

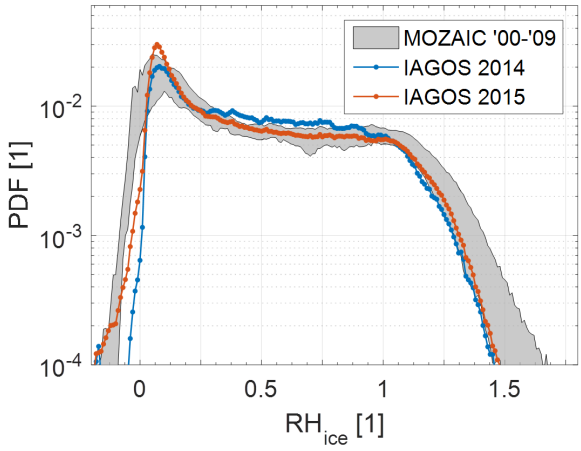

Figure 6.4: Probability density function of RH_{ice} values for the IAGOS data sets collected in 2014 and 2015. The grey shaded area represents the value range covered by the MOZAIC data between 2000 and 2009.

The global set of IAGOS RH_{ice} - N_{ice} data obtained in the upper troposphere between July 2014 and October 2015 is shown in Figure 6.5(a) as PDF of observations, normalised to the complete data set of 6939 hours of sampling at $p < 350$ hPa in clear sky and in-cloud.

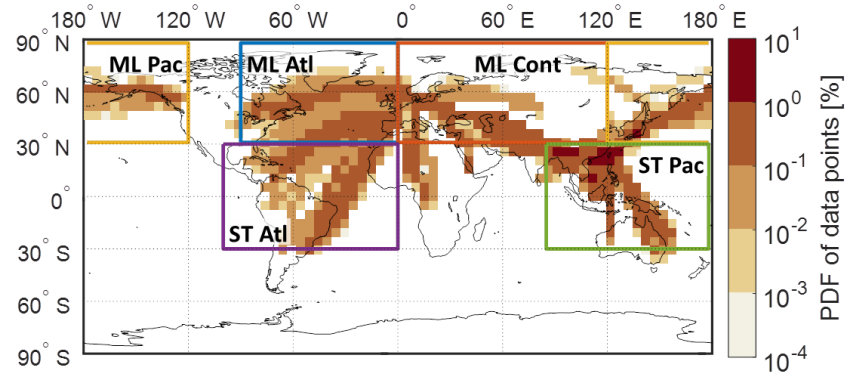

(a)

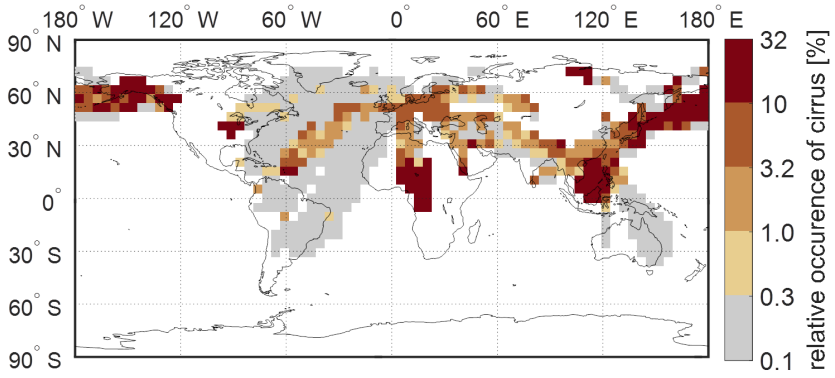

(b)

Figure 6.5: (a) Data collected with ICH and BCP; the data set of 6939 hours of sampling is limited to the upper troposphere; boxes indicate regions with sufficient data coverage for detailed analyses. (b) Annual mean of global-scale cirrus cloud coverage as observed by IAGOS aircraft.

The main flight routes of the IAGOS fleet are clearly visible. For detailed analysis, five regions were identified with sufficient data coverage (Table 6.2), whereas the latitudinal bounds of mid-latitudes (abbreviated ML) and sub-tropical to tropical latitudes (abbreviated ST) are 30 to 60°N and 30°N to 30°S, similar to former studies, e.g. Beswick et al. [2015], Spichtinger et al. [2003b].

The annually averaged global distribution of cirrus cloud observations by IAGOS aircraft is presented in Figure 6.5(b), where the global patterns correspond to features reported from annually averaged cirrus cloud coverage data from CloudSat and CALIPSO satellites [Sassen et al., 2008]. Relating the vertical distribution of cirrus cloud occurrence from CloudSat/CALIPSO observations to the aircraft cruise altitude

Table 6.2: List of five regions with sufficient data coverage.

	ML Atl	ML Cont	ML Pac	ST Atl	ST Pac
Latitude	30-60°N			30°N-30°S	
Longitude	90-0°W	0-120°E	120-180°E 180-120°W	100-0°W	85-180°E

band between 8 km and 13 km, IAGOS observations cover all cirrus occurrences at mid-latitudes, while the hot spot of cirrus occurrence over the tropics between 12 and 18 km (Figure 6.6) is mostly outside of the aircraft cruise altitude band. Nevertheless, the cirrus hotspots over the subtropical and tropical regions are both reported from space-borne observations and from IAGOS in-situ observations.

The regional distribution patterns of cirrus occurrence at mid-latitudes, where altitude bands of cirrus observations from satellites and from in-situ observations by passenger aircraft coincide, are found over the North Atlantic between Europe and Central America and over the Northern Pacific in both data sets. Beswick et al. [2015] showed similar global distributions in their study focused on IAGOS cloud observations.

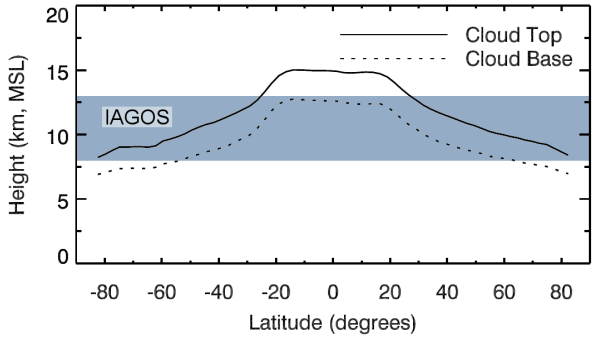

Figure 6.6: Annual average latitudinal dependence of identified cirrus cloud top and base heights (black lines) determined with CloudSat/CALIPSO by Sassen et al. [2008, courtesy of American Geosciences Union] with additional IAGOS aircraft cruise altitude pattern (blue shaded area) between 8 and 13 km.

To improve our knowledge about cirrus, the RH_{ice} distributions for in-clouds and clear sky are investigated. The resulting probability distributions (PDF) for the five different regions (Mid-latitudes: Atlantic Ocean, Eurasian Continent, and Pacific Ocean; Subtropics and Tropics: Atlantic Ocean and Pacific Ocean) are shown in Figure 6.7(a), where for all studied regions the most probable values of RH_{ice} in cirrus cloud is at ice supersaturations of 105 - 110%. Even though the ICH measurement uncertainty is 5% RH_{liquid}, the observations indicate a small amount of ice supersaturation in cirrus. The shape of the cirrus distributions

is remarkably similar for all studied regions with only a slight deviation towards drier conditions in the mid-latitudes continental region (Figure 6.7(c)).

Between 85% and 95% of all measurements in clear sky (Fig. 6.7(b and d)) are in the state of ice subsaturation which is in agreement with other studies on the distribution of relative humidity in the upper troposphere and tropopause region [Ovarlez et al., 2002, Spichtinger et al., 2002]. The shape of the clear sky distributions is again similar for all studied regions with an exponential decay in probability for high supersaturations, whereas there is a tendency of slightly increased probability of air masses in the mixing state ($\sim$50% RH_{ice}) in the ML Atlantic region. The joint behaviour of all clear sky regions is in accordance with the results by, e.g. Gettelman et al. [2006], Gierens et al. [1999] and Spichtinger et al. [2003b].

The observed affinity for ice supersaturation in cirrus clouds, however, conflicts the reported results of several field studies on cirrus clouds which formed the common understanding of a thermodynamic equilibrium in cirrus clouds with the modal value of $RH_{ice} = 100\%$ [Diao et al., 2014, Krämer et al., 2009, Ovarlez et al., 2002]. Nevertheless, there are also other studies which found slight supersaturations with $RH_{ice} \approx$100 - 110%, [e.g. Diao et al., 2015], similar to our observations.

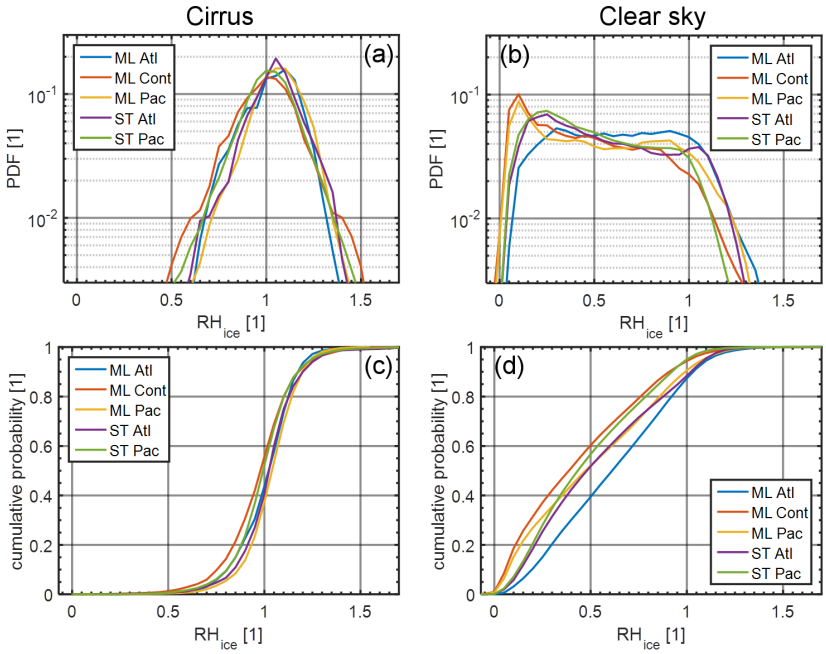

Figure 6.7: Probability distribution functions of RH_{ice} (a, b) and cumulative probability distribution of RH_{ice} (c, d) for the identified regions in cirrus and in clear sky.

Table 6.3: Fraction of cirrus observations for different regimes of maximum ice cloud density $N_{ice,max}$.

Ice cloud density	**Fraction of cirrus observations**				
	ML Atl	**ML Cont**	**ML Pac**	**ST Atl**	**ST Pac**
$N_{ice,max}$ **= 0.015 cm^{-3}**	54%	61%	44%	41%	40%
$N_{ice,max}$ **= 0.10 cm^{-3}**	87%	90%	81%	74%	67%
$N_{ice,max}$ **= 1.0 cm^{-3}**	99.4%	99.4%	98.0%	97.0%	95.0%

A possible explanation for the supersaturation in cirrus clouds is the process of continuous uplifting of already formed clouds which results in higher dynamical equilibrium supersaturations and higher N_{ice} depending on the uplift velocity [Krämer et al., 2009]. The behaviour that a persistent upward motion in open thermodynamic systems, like it is the case for ice clouds, acts as an external forcing that causes supersaturation, is also found from model simulations [Spichtinger and Gierens, 2009, Spichtinger, 2014]. These model simulations also see that ice clouds can stay at slight supersaturations of $RH_{ice} \approx$ 105 - 110%.

The RH_{ice} in-situ measurements in this study could be conducted before the dynamic equilibrium is reached, which results in relative humidity significantly higher than 105 - 110%. Heymsfield et al. [1998] explained these events by the continuous lowering of the water vapour saturation value $e_{sat,ice}(\mathrm{T})$ by cooling of the air during uplifting which is faster than the depletion of the ambient gas phase water e by ice crystal growth. As a result, high $RH_{ice} = e/e_{sat,ice}$ can be observed (compare to Equation 1.1 in Chapter 1).

Despite the overall similar RH_{ice} distributions for the five regions, Table 6.3 demonstrates the differences in the properties of cirrus clouds. It has to be noted that the threshold value of N_{ice} =0.015 cm^{-3} results in a fraction between 40% (ST Pac) and 61% (ML Cont) of the observations to fall into the category of indeterminate events and might be very thin cirrus. Besides that, thin cirrus with N_{ice} <0.1 cm^{-3} make up the majority of observed cirrus with respective fractions of all detected ice particle number concentrations between 90% over the mid-latitudes continent and 67% over the Pacific in the subtropics and tropics. Dense clouds, on the other hand, are rarely observed with less than 1% in the mid-latitudes and up to 5% over the Pacific Ocean.

In a last step, the RH_{ice} - N_{ice} data set is explored for the expected relationship between higher supersaturations at higher uplift velocities and the resulting higher N_{ice} values in cirrus clouds. To ensure a higher statistical robustness when separating into different ice crystal number regimes the following analysis is limited to mid-latitude, subtropics and tropics observations. Thus, Figure 6.8 (respective percentiles in Table 6.4) shows the RH_{ice} distributions in cirrus as a function of N_{ice} for both mid-latitude and subtropical to tropical cirrus, in which the ice crystal number concentration regimes are divided into $N_{ice} \leq 0.1$ cm^{-3}, N_{ice} between 0.1 cm^{-3} and 1.0 cm^{-3}, and $N_{ice} > 1.0$ cm^{-3}.

Cirrus clouds in the lowest N_{ice} regime have their relative humidity with respect to ice distributed equally around saturation, independent of the geographic regime. RH_{ice} in the medium N_{ice} regime starts to be asymmetrically distributed and is slightly supersaturated with $RH_{ice} \approx$ 105 - 110%, and finally the

$N_{ice} > 1.0$ cm^{-3} regime show significant amounts of high ice supersaturation with values above 140% which are not observed in the other clouds. Even the median RH_{ice} values differ and increase with higher N_{ice} regimes; see Table 6.4.

As discussed previously, RH_{ice} in cirrus with continuous uplifting tends to supersaturation, whereas the quantity depends on the vertical velocity. For both geographic regions increased N_{ice} values are associated with enhanced RH_{ice} values, which highlights the strong connection between ice crystal number concentration and the respective RH_{ice} distribution. However, the N_{ice} values above 1 cm^{-3} are found more frequently in the subtropics to tropics compared to the mid-latitudes. Also the shape of the distribution functions of RH_{ice} for this densest type of cirrus differ significantly between mid-latitudes and the subtropics and tropics. While dense ice clouds at mid-latitudes (Fig. 6.8(a)) show regions of uplifts (bulge in the black line when $RH_{ice} > 100\%$) as well as downdrafts (bulge in the black line when $RH_{ice} < 100\%$), the same type of cirrus in the tropics and subtropics (Fig. 6.8(b)) is dominated by strong uplifts, which may explain the observation of high N_{ice} values. Since this kind of study requires a data set of sufficient size to ensure statistical robustness, there are no other studies to compare with.

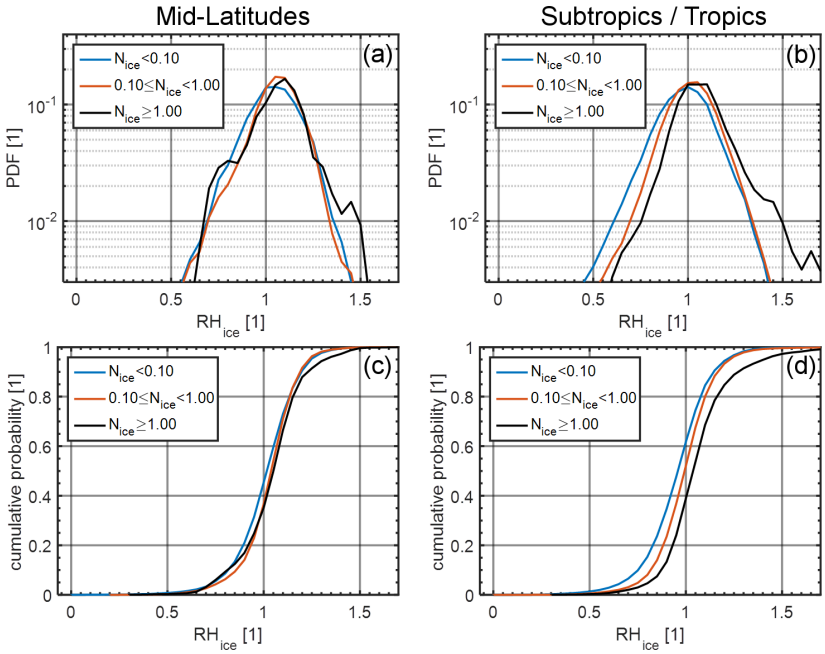

Figure 6.8: Probability distribution function of RH_{ice} for the different N_{ice} regimes (unit is cm^{-3}) at mid-latitudes (a) and subtropics to tropics (b); same for the cumulative distribution functions in (c) and (d).

Table 6.4: Percentiles of the RH_{ice} distributions for the different regimes of cloud density.

	Mid-latitudes				Subtropics / Tropics			
N_{ice} [cm^{-3}]	No. of data	45 perc. [% RH_{ice}]	Median [% RH_{ice}]	55 perc. [% RH_{ice}]	No. of data	45 perc. [% RH_{ice}]	Median [% RH_{ice}]	55 perc. [% RH_{ice}]
< 0.1	65616	102.4	104.1	105.9	83812	96.6	98.3	100.1
0.1 - 1.0	33529	104.9	106.3	107.8	83721	100.2	101.8	103.4
> 1.0	3555	106.0	107.5	109.0	17175	104.6	106.3	107.9

The possible contamination of the RH_{ice} distribution by contrails especially in the highly frequented flight routes over the North Atlantic can neither be validated nor invalidated with the available data.

6.4 Conclusions

Understanding the distribution and occurrence of ice supersaturated regions (ISSR) in the UTLS is of high relevance due to its close link to cirrus formation and lifecycle. While ice supersaturation is the relevant requirement for ice nucleation, the humidity distribution in cirrus clouds controls the further evolution. Increasing our knowledge about humidity distribution in clear sky and in cirrus would therefore decrease one of the largest uncertainties in the Earths energy balance: the radiative impact of cirrus clouds.

In this chapter the fraction of ISSR in seven vertical layers centred around the tropopause from observations gained with in-situ aircraft measurements in the MOZAIC programme in the North Atlantic flight corridor is studied. Within 15 years a representative distribution of this fraction is presented in detail, whereas the absolute quantity is dependent of the chosen tropopause criteria, and thus, the dynamical tropopause definition turned out to include 20% more ISSR in the UT than the thermal definition, which has an increasing seasonal mean fraction of ISSR with height up to 34%. While the thermal tropopause criteria neglects ISSR in the lowermost stratosphere by an insignificant seasonal fraction, the dynamical approach reveals a significant median seasonal fraction of approx. 8%.

A deeper analysis of the air mass properties in ISSR showed, that ISSRs determined with the thermal tropopause definition are colder, drier, and with less ozone than its corresponding non-ISSR measurements which could be explained with the potential increased probability of ISSR in the North Atlantic flight corridor in winter. The difference in the dynamical tropopause analysis is that ISSR in the lowermost stratosphere have clear tropospheric air mass fingerprints due to ozone VMR values below the threshold of 120 ppbv [Thouret et al., 2006]. A further extended analysis in the future is necessary to state a final conclusion.

What will be possible in the future when analysing IAGOS data is demonstrated with the emerging global-scale data set on relative humidity with respect to ice (RH_{ice}) and cirrus cloud particle number concentration (N_{ice}) from the first available 15 months of combined measurements. This data set has been

analysed for the distribution of RH_{ice} in cirrus and in clear sky and for the potential connections between RH_{ice} and N_{ice}.

Cirrus cloud observations are split into sub-sets of mid-latitude and subtropical to tropical observations and further divided into observations over the Atlantic Ocean, the Eurasian continent and the Pacific Ocean. Since seasons are not equally represented, the data is analysed as a whole.

One of the key findings discovered in the IAGOS data set is that the distribution of RH_{ice} inside clouds shows a strong correlation to N_{ice}, i.e. higher N_{ice} values are associated with higher dynamic equilibrium RH_{ice} values. It was also shown that the in-cloud distributions of RH_{ice} do not depend on the geographical regions of sampling.

Combining the global frequency of occurrence of cirrus clouds (Figure 6.5(b)) with the RH_{ice} distribution in clouds for three regimes of N_{ice} values (Figure 6.8) and the respective probability of occurrence in Table 6.3, a sketch of cirrus types can be drawn:

For thin clouds with $N_{ice} \leq 0.1$ cm^{-3} in the subtropics and tropics, the RH_{ice} distribution is centred at 100% as expected for cirrus in thermodynamic equilibrium. For the same cloud type at mid-latitudes, however, the modal RH_{ice} value is shifted to approx. 105% which indicates considerable uplifts in cirrus. This indication is confirmed by model studies with continuous uplifts [Spichtinger and Gierens, 2009, Spichtinger, 2014].

For cirrus with 0.1 cm^{-3} $\leq N_{ice} \leq$ 1.0 cm^{-3} the distribution of RH_{ice} becomes asymmetric and is centred at 105 - 110% with its larger part in ice supersaturation. Higher uplifts than in the previous type seem to be the driving force in the cloud formation and maintain during the cirrus evolution.

For cirrus with $N_{ice} > 1.0$ cm^{-3} highest ice supersaturations are observed with values as high as 170% RH_{ice} in the subtropical to tropical cirrus. To reach that high ice supersaturation and ice particle number concentrations quite strong uplifts due to convection have to be involved in the evolution of the cirrus.

In the future the continuously growing IAGOS data set allows amongst others the investigation of seasonal aspects of cirrus formation and properties.

CHAPTER 7

CONCLUSIONS AND OUTLOOK

7.1 Conclusions

Within the framework of this thesis, a broad spectrum of objectives have been worked on to increase knowledge of water vapour distribution in the upper troposphere and lower stratosphere (UTLS) which is essential for understanding cloud formation processes and the Earth's radiation budget. For this purpose, the first 15 years of ongoing relative humidity and temperature in-situ measurements by the European infrastructure MOZAIC (since 2011 IAGOS) were examined. Moreover, automatic analysis routines have been developed based on the existing manual routines to assure a homogeneous and traceable reanalysed MOZAIC data set. The most important are the automatic calibration analysis routine for the used capacitive hygrometer as well as the automatic flight data analysis routine for the daily incoming observations gathered by the participating commercial passenger aircraft fleet.

In order to be able to better assess the upcoming findings, the MOZAIC Capacitive Hygrometer (MCH) was flown during the CIRRUS-III (2006) aircraft campaign to undergo a blind intercomparison with high performance water vapour instruments based on tunable diode laser absorption spectrometry (in-cloud reference) and Lyman-α fluorescence detection (clear sky reference). When restricting the data to MOZAIC relevant conditions, the analysis of the flights have revealed an overall good agreement with no significant offset and a mean measurement uncertainty of 5% relative humidity with respect to liquid water ($\mathrm{RH_{liquid}}$). Furthermore, the analysis showed no contamination of humidity measurements when flying through cir-

rus clouds. In summary, it is concluded that the MCH is highly suitable for climatology analyses in the MOZAIC programme even if the sensor is not applicable to high time resolution measurements.

The application of a new capacitive hygrometer in 2011 let arise the question, if the modified IAGOS Capacitive Hygrometer (ICH) can confirm the performance and data quality of the former hygrometer. By participating the AIRTOSS-ICE (2013) aircraft campaign, the ICH was evaluated in a blind intercomparison against reference techniques similar to the MCH evaluation. The analysis demonstrated again a very well agreement in cross correlations for ICH and the reference instruments over the entire cloud-free range and for the most of the cirrus clouds sequences and confirmed the uncertainty of 5% RH_{liquid}.

Since both capacitive hygrometer showed similar behaviour of increased deviations to the reference RH_{liquid} data with decreasing sensor temperatures, both field campaigns have been combined and the temperature-dependence of the sensor's response time was determined. With the application of the resulting exponential filter function to the measured reference RH_{liquid} data, the MCH and ICH RH_{liquid} data could be reproduced with significantly decreased deviations. In summary, the quality of the upper tropospheric humidity data is preserved during the transition from the MCH to the modified ICH, and a long-time data set for upper tropospheric and lower stratospheric water vapour climatology and trend analyses is ensured, when combining MOZAIC and IAGOS humidity data sets.

In the following part of the thesis, water vapour in-situ measurements in the North Atlantic flight corridor have been analysed for the first time with such a high vertical resolution, for such a long period, and with such a statistical robustness like it is possible within the MOZAIC programme. Starting with a comprehensive analyses of 15 years of MOZAIC relative humidity measurements the questions about water vapour background climatologies was processed in Chapter 4. Considering the variation of atmospheric stratification with space and time, the humidity data was therefore separated into seven vertical layers around the extratropical thermal tropopause height. The three stratospheric layers are characterized by a monomodal distribution in the dry mode down to 5% RH_{ice} and a development of an increased skewness rightward down to the tropopause layer. The upper tropospheric layers are most probable supersaturated and develop a dry mode with increased distance to the tropopause which might be explained by subsided air masses. The tropopause layer, in contrast, is defined by a broad distribution which underlines the assumption of a mixing layer. Besides the relative humidity also the temperature and water vapour volume mixing ratio (H_2O VMR) distributions were determined in the seven vertical layers. While temperatures follow linear Gaussian distributions with coldest layer in the tropopause, the H_2O VMR showed an exponential Gaussian distribution with stepwise decrease with height. Irregularities in the H_2O VMR distribution indicate the lower limit of MCHs accuracy ($\sim$10 ppmv). Finally, the results were compared with model statistics gained from ECMWF ERA-Interim reanalysis data. The general features of the humidity distribution were confirmed by the model, whereas MCH data scatter statistically in the dry values and the model cuts off ice supersaturation when ice is present. Also the seasonal distributions agreed well in the variables of temperature, RH_{ice} and H_2O VMR, however temperatures in the tropopause layer showed a significant signal to warmer temperatures in the model which also missed an ice supersaturation fraction of about 10-15% probability in the upper troposphere.

The upcoming analyses in Chapter 5 was addressed to the questions if there is any trend observed in the measurements and if there are any stratosphere-troposphere exchange processes detected and in such a case their related transport pathways had to be identified. To do so, the time resolution was increased to monthly distributions for the closest layer above and below the tropopause layer. The monthly RH_{ice} distribution revealed a more or less constant state with high variability, while monthly temperature and H_2O VMR distributions presented an annual cycle with the warmest month in July with the highest H_2O VMR in August, and the coldest month with the fewest H_2O VMR in January. The evaluation of the deseasonalised time series could not offer any trend in the variables which is enhanced by the high monthly variabilities. These variabilities were explained with two approaches. The humidity and moister in the winter months seemed to be regulated by the temperature according to the Clausius Clapeyron equation because the strong vertical temperature gradients in the UT implied a high stability and with that a reduced possibility of vertical motion. This assumption is supported by the lowest upper tropospheric H_2O VMR values and RH_{ice} values around saturation. In addition, ozone distributions in winter indicated a strict separation of troposphere and stratosphere due to the greatest influence of the Brewer-Dobson circulation which suppresses exchanges with subsided deep stratospheric air masses. While this separation weakened until summer, the influence of the Brewer-Dobson circulation weakened and a quasi isentropic transport was seen near the northern hemispheric subtropical jet. Furthermore, shallow mixing of air masses was recognised throughout the year in the surrounding of the tropopause.

Because of the close link of ice supersaturated regions (ISSR) to cirrus cloud formation and lifecycle, the vertical distribution of ISSR fraction in the vicinity of the tropopause was studied in Chapter 6. With the 15 years comprehensive MOZAIC data set a representative vertical distribution of this fraction was presented in detail, whereas the absolute quantity was dependent of the chosen tropopause criteria. In the main, the dynamical tropopause definition turned out to include significantly more ISSR than the thermal definition which offered a seasonal mean fraction of ISSR up to 34% in the UT. While the thermal tropopause criteria neglected ISSR in the lowermost stratosphere, the dynamical approach revealed a significant median seasonal fraction of approx. 8%. Nevertheless, these stratospheric ISSR had clear tropospheric air mass fingerprints with ozone VMR values below the threshold of 120 ppbv [Thouret et al., 2006]. In principle, the air mass properties of non-ISSR measurements differed clearly from the ISSR measurements which were colder, drier, and with less ozone values.

In a final consideration, the first available 15 months of combined measurements by RH_{ice} and the new cloud index measurements in IAGOS were used in a case study to investigate the connection of ice supersaturation and cirrus cloud formation for different global regions. The distribution of RH_{ice} inside clouds showed a strong correlation to the ice particle number concentration (N_{ice}), i.e. higher N_{ice} values were associated with higher dynamic equilibrium RH_{ice} values. It was also shown that the in-cloud distributions of RH_{ice} do not depend on the geographical regions of sampling. A further separation of cirrus cloud types has been conducted and for thin clouds in the subtropics and tropics, the RH_{ice} distribution was centred at saturation as expected for cirrus in thermodynamic equilibrium. For the same cloud type at mid-latitudes, however, the modal RH_{ice} value was shifted to supersaturation which indicated considerable uplifts in cir-

rus which was confirmed by model studies with continuous uplifts. Higher uplifts seemed to be the driving force in the cloud formation and maintain during medium dense cirrus evolution when the distribution became asymmetric with its larger part in ice supersaturation. Cirrus with the highest number concentrations let us observe the highest ice supersaturations with values as high as 170% RH_{ice} in the subtropical to tropical cirrus. To reach that high ice supersaturation and ice particle number concentrations quite strong uplifts due to convection have to be involved in the evolution of the cirrus.

7.2 Outlook

This study on water vapour distributions in the upper troposphere and lower stratosphere demonstrated the power of the MOZAIC/IAGOS data set by addressing different aspects of atmospheric research fields. In order to advance our understanding of e.g. water vapour distributions, transport pathways or the interaction between ice supersaturation and cirrus cloud, further investigations are necessary to answer a number of open questions.

As already mentioned in Chapter 5 the In-Flight Calibration method is in its evaluation process and will be properly applied to the entire more than two decades of in-situ measurement data set to improve the quality until the lower stratosphere. This improved and extended humidity data set will enable the determination of climatologies for different global regions and furthermore trend analyses will investigate the evolution of atmospheric water vapour distribution in a more robust approach.

By means of on-going simultaneous measurements of relative humidity and ice cloud number concentration, the understanding of cloud formation and cloud lifecycle processes will be enhanced by separating the measurements with a seasonal approach. Besides the analyses on the average connection, an increased data set enables also the atmospheric transport mechanisms to be involved into the cloud development. One of the most important impacts of this simultaneous measurement on passenger aircraft is the ability to be part of current studies about satellite-based thunderstorm nowcasting for strategic flight planning en-route [Forster et al., 2016]. There, IAGOS in-situ measurements are used to evaluate the predicted thunderstorm motion and nowcasting system with respect to flight safety and efficiency.

In order to provide the best quality of humidity and temperature data by the IAGOS programme, a comprehensive study about measured ascent and descent profiles has to be conducted with respect to fast changing atmospheric conditions and with respect to flight sequences flying through warm clouds. It might be reasonably assumed, that measurements could be perturbed by potentially sampled liquid water droplets which further causes a contamination of following flight sequences. These warm cloud events have to be detected and potential hysteresis effects determined, calculated and considered in the quality control. By providing this quality check on the data, especially on the automated near real time data, the IAGOS humidity and temperature profiles are highly suitable to be used as evaluation data set for model simulations and satellite measurements or to be assimilated directly in the calculation of weather model simulation.

References

Alteköster, L.: Analysis of coverage of global upper troposphere and lowermost stratosphere data by MOZAIC observations, Bachelor's thesis, Rheinisch-Westfälische Technische Hochschule Aachen, in cooperation with the Institute for Energy and Climate, IEK-8: Troposphere, 2014.

Anderson, J. G., Wilmouth, D. M., Smith, J. B., and Sayres, D. S.: UV dosage levels in summer: Increased risk of ozone loss from convectively injected water vapor, Science, 337, 835–839, doi:10.1126/science.1222978, 2012.

Bange, J., Esposito, M., Lenschow, D. H., Brown, P. R. A., Dreiling, V., Giez, A., Mahrt, L., Malinowski, S. P., Rodi, A. R., Shaw, R. A., Siebert, H., Smit, H. G. J. and Zöger, M.: Measurement of Aircraft State and Thermodynamic and Dynamic Variables, in: Airborne Measurements for Environmental Research: Methods and Instruments, edited by: Wendisch, M., and Brenguier, J.-L., Wiley Online Library, doi:10.1002/9783527653218.ch2, 2013.

Berberan-Santos, M. N., Bodunov, E. N., Pogliani, L.: On the barometric formula, American Journal of Physics, 65(5), 404–412, doi:10.1119/1.18555, 1997.

Berkes, F., Neis, P., Rohs, S., Smit, H. G. J., Schulz, M., Konopka, P., Nédélec, P., Boulanger, D., and Petzold, A.: Long-term Temperature Measurements of the Upper Troposphere and Lowermost Stratosphere with MOZAIC and IAGOS, Geophys. Res. Abs., Vol. 18, EGU2016-6479, 2016.

Beswick, K., Baumgardner, D., Gallagher, M., Volz-Thomas, A., Nédélec, P., Wang, K.-Y., and Lance, S.: The backscatter cloud probe – a compact low-profile autonomous optical spectrometer, Atmos. Meas. Tech., 7, 1443-1457, doi:10.5194/amt-7-1443-2014, 2014.

Beswick, K., Baumgardner, D., Gallagher, M., Raga, G. B., Minnis, P., Spangenberg, D. A., Volz-Thomas, A., Nédéle, P., and Wang, K. Y.: Properties of small cirrus ice crystals from commercial aircraft measurements and implications for flight operations, Tellus B, 67, 27876, doi:10.3402/tellusb.v67.27876, 2015.

Bethan, S., Vaughan, G., and Reid, S. J.: A comparison of ozone and thermal tropopause heights and the impact of tropopause definition on quantifying the ozone content of the troposphere, Q. J. R. Meteorol. Soc., 122, 929-944, doi:10.1002/qj.49712253207, 1996.

Birner, T., Dörnbrack, A., and Schumann, U.: How sharp is the tropopause at midlatitudes? Geophys. Res. Lett., 29, 45-1 – 45-4, doi:10.1029/2002gl015142, 2002.

Bönisch, H., Engel, A., Birner, T., Hoor, P., Tarasick, D. W., and Ray, E. A.: On the structural changes in the Brewer-Dobson circulation after 2000, Atmos. Chem. Phys., 11, 3937–3948, doi:10.5194/acp-11-3937-2011, 2011.

Brenninkmeijer, C. A. M., Crutzen, P. J., Fischer, H., Gusten, H., Hans, W. Heinrich, G., Heintzenberg, J., Hermann, M., Immelmann, T., Kersting, D., Maiss, M., Nolle, M., Pitscheider, A., Pohlkamp, H., Scharffe, D., Specht, K., and Wiedensohler, A.: CARIBIC - civil aircraft for global measurement of trace gases and aerosols in the tropopause region. J. Ocean. Atmos. Technol. 16, 1373–1383. doi:10.1175/1520-0426(1999)016¡1373:CCAFGM¿2.0.CO;2, 1999.

Brogniez, H., Clain, G., and Roca, R.: Validation of upper-tropospheric humidity from SAPHIR on board Megha-Tropiques using tropical soundings, J. Appl. Meteorol. Climatol., 54, 896–908, doi:10.1175/JAMC-D-14-0096.1, 2015.

Brunner, D., Staehelin, J., Jeker, D., Wernli, H., and Schumann, U.: Nitrogen oxides and ozone in the tropopause region of the Northern Hemisphere: Measurements from commercial aircraft in 1995/1996 and 1997, J. Geophys. Res. Atmos., 106, 27673–27699, doi:10.1029/2001JD900239, 2001.

Buchholz, B., Kühnreich, B., Smit, H. G. J. and Ebert, V.: Validation of an extractive, airborne, compact TDL spectrometer for atmospheric humidity sensing by blind intercomparison, Appl. Phys. B., 110, 249-262, doi:10.1007/s00340-012-5143-1, 2013.

Buchholz, B., Böse, N., and Ebert, V.: Absolute validation of a diode laser hygrometer via intercomparison with the German national primary water vapor standard, Appl. Phys. B., 116, 883-899, doi:10.1007/s00340-014-5775-4, 2014.

Bundke, U., Berg, M., Houben, N., Ibrahim, A., Fiebig, M., Tettich, F., Klaus, C., Franke, H., and Petzold, A.: The IAGOS-CORE aerosol package: instrument design, operation and performance for continuous measurement aboard in-service aircraft, Tellus B, 67, 28339, doi:10.3402/tellusb.v67.28339, 2015.

Butchart, N. and Remsberg, E. E.: The area of the stratospheric polar vortex as a diagnostic tracer for transport on an isentropic surface, J. Atmos. Sci., 45, 1319-1339, doi:10.1175/1520-0469(1986)043¡1319:TAOTSP¿2.0.CO;2, 1986.

Butchart, N.: The Brewer-Dobson circulation, Rev. Geophys., 52, 157–184, doi:10.1002/2013RG000448, 2014.

Chen, T., Rossow, W. B. and Zhang, Y.: Radiative effects of cloud-type variations, J. Clim. 13, 264–286, doi:10.1175/1520-0442(2000)013¡0264:REOCTV¿2.0.CO;2, 2000.

Clark, H., Sauvage, B., Thouret, V., Nédélec, P., Blot, R., Wang, K. Y., Smit, H. G. J., Neis, P., Petzold, A., Athier, G., Boulanger, D., Cousin, J.-M., Beswick, K., Gallagher, M., Baumgardner, D., Kaiser, J., Flaud, J.-M., Wahner, A., Volz-Thomas, A., and Cammas, J.-P.: The first regular measurements of ozone, carbon monoxide and water vapour in the Pacific UTLS by IAGOS, Tellus B, 67, 28385, doi:10.3402/tellusb.v67.28385, 2015.

Cooper, O. R., Stohl, A., Eckhardt, S., Parrish, D. D., Oltmans, S. J., Johnson, B. J., Nédélec, P., Schmidlin, F. J., Newchurch, M. J., Kondo, Y., and Kita, K.: A springtime comparison of tropospheric ozone and transport pathways on the east and west coasts of the United States, J. Geophys. Res., 110, D05S90, doi:10.1029/2004JD005183, 2005.

Cox, S.: Cirrus clouds and climate, J. Atmos. Sci., 28, 1513–1515, doi:10.1175/1520-0469(1971)028¡1513:CCATC¿2.0.CO;2, 1971.

Dessler, A. E., and Sherwood, S. C.: A matter of humidity, Science, 323(5917), 1020–1021, doi:10.1126/science.1171264, 2009.

Dessler, A. E., Schoeberl, M. R., Wang, T., Davis, S. M., and Rosenlof, K. H.: Stratospheric water vapor feedback, Proc. Natl. Acad. Sci. U. S. A., 110(45), 18087–18091, doi:10.1073/pnas.1310344110, 2013.

Diao, M., Zondlo, M. A., Heymsfield, A. J., Avallone, L. M., Paige, M. E., Beaton, S. P., Campos, T., Rogers, D. C.:Cloud-scale ice-supersaturated regions spatially correlate with high water vapor heterogeneities, Atmos. Chem. Phys., 14(5), 2639-2656, doi:10.5194/acp-14-2639-2014, 2014.

Diao, M., Jensen, J. B., Pan, L. L., Homeyer, C. R., Honomichl, S., Bresch, J. F., and Bansemer, A.: Distributions of ice supersaturation and ice crystals from airborne observations in relation to upper tropospheric dynamical boundaries, J. Geophys. Res. Atmos., 120(10), 5101–5121, doi:10.1002/2015JD023139, 2015.

Engel, A., Bönisch, H., Brunner, D., Fischer, H., Franke, H., Gnther, G., Gurk, C., Hegglin, M., Hoor, P., Königstedt, R., Krebsbach, M., Maser, R., Parchatka, U., Peter, T., Schell, D., Schiller, C., Schmidt, U., Spelten, N., Szabo, T., Weers, U., Wernli, H., Wetter, T., and Wirth, V.: Highly resolved observations of trace gases in the lowermost stratosphere and upper troposphere from the Spurt project: an overview, Atmos. Chem. Phys., 6, 283-301, doi:10.5194/acp-6-283-2006, 2006.

Dee, D. P., Uppala, S. M., Simmons, A. J., Berrisford, P., Poli, P., Kobayashi, S., Andrae, U., Balmaseda, M. A., Balsamoa, G., Bauer, P., Bechtold, P., Beljaars, A. C. M., van de Berg, L., Bidlot, J., Bormann, N., Delsol, C., Dragani, R., Fuentes, M., Geer, A. J., Haimberger, L., Healy, S. B., Hersbach, H., Holm, E. V., Isaksen, L., Kallberg, P., Köhler, M., Matricardi, M., McNally, A. P., Monge-Sanz, B. M., Morcrette, J.-J., Park, B.-K., Peubey, C., de Rosnay, P., Tavolato, C., Thepaut, J.-N., and Vitart, F.: The ERA-Interim reanalysis: configuration and performance of the data assimilation system, Q. J. R. Meteorol. Soc., 137: 553-597, doi:10.1002/qj.828, 2011.

Duhnke, K., Smit, H. G. J., Kley, D., Marenco, A., Speth, P.,and Wefers, J.: Untersuchung der in MOZAIC gemessenen Ozon-und Wasserdampfverteilung im polaren Strahlstrom ber dem Nordatlantik, Jül. Ber., 3593, Jülich, Germany, 1998.

Elliott, W. P., and Gaffen, D. J.: On the utility of radiosonde humidity archives for climate studies. Bull. Amer. Meteor. Soc., 72, 1507–1520, doi:10.1175/1520-0477(1991)072¡1507:OTUORH¿2.0.CO;2, 1991.

Eyre, J. and Reid, R.: Cost-Benefit Studies for Observing Systems, Met Office Forecasting Research Tech. Rep. 593, 11 pp, 2014.

Fahey, D. W., Gao, R.-S., Möhler, O., Saathoff, H., Schiller, C., Ebert,V., Krämer, M., Peter, T., Amarouche, N., Avallone, L. M., Bauer, R., Bozoki, Z., Christensen, L. E., Davis, S. M., Durry, G., Dyroff, C., Herman, R. L., Hunsmann, S., Khaykin, S. M., Mackrodt, P., Meyer, J., Smith, J. B., Spelten, N., Troy, R. F., Vömel, H., Wagner, S., and Wienhold, F. G.: The AquaVIT-1 intercomparison of atmospheric water vapor measurement techniques, Atmos. Meas. Tech., 7, 3177–3213, doi:10.5194/amt-7-3177-2014, 2014.

Filges, A., Gerbig, C., Chen, H., Franke, H., Klaus, C., and Jordan, A.: The IAGOS-CORE Greenhouse Gas (GHG) package: a measurement system for continuous airborne observations of CO_2, CH_4, H_2O and CO, Tellus B. 67, 27989, doi:10.3402/tellusb.v67.27989, 2015.

Forster, P. and Shine, K.: Assessing the climate impact of trends in stratospheric water vapor, Geophys. Res. Lett., 29(6), 1086,doi:10.1029/2001GL013909, 2002.

Forster, C., Ritter, A., Gemsa, S., Tafferner, A., and Stich, D.: Satellite-Based Real-Time Thunderstorm Nowcasting for Strategic Flight Planning En Route, Journal of Air Transportation, Vol. 24, No. 4, pp. 113-124, doi:http://dx.doi.org/10.2514/1.D0055, 2016.

Frey, W., Eichler, H., de Reus, M., Maser, R., Wendisch, M., and Borrmann, S.: A new airborne tandem platform for collocated measurements of microphysical cloud and radiation properties, Atmos. Meas. Tech., 2, 147-158, doi:10.5194/amt-2-147-2009, 2009.

Fueglistaler, S., Bonazzola, M., Haynes, P. H., and Peter, T.: Stratospheric water vapor predicted from the Lagrangian temperature history of air entering the stratosphere in the tropics, J. Geophys. Res., 110(D8), doi:10.1029/2004JD005516, 2005.

Fueglistaler, S., Dessler, A. E., Dunkerton, T. J., Folkins, I., Fu, Q., and Mote, P. W.: Tropical tropopause layer, Reviews of Geophysics, 47(1), doi:10.1029/2008RG000267, 2009.

Fusina, F., Spichtinger, P., and Lohmann, U.: Impact of ice supersaturated regions and thin cirrus on radiation in the midlatitudes, J. Geophys. Res. 112(D24), doi:10.1029/2007JD008449, 2007.

Gaffen, D. J.: Historical changes in radiosonde instruments and practices, WMO Final Rep., Instruments and Observation Methods Rep. 50, WMO/TD 541, 123 pp, 1993.

GCOS 2010: Implementation Plan for the Global Observing System for Climate in Support of the UNFCCC(ed. (WMO), W. M. O.). WMO, Geneva, Switzerland, 186.

Gettelman, A., Fetzer, E. J., Eldering, A., and Irion, F. W.: The Global Distribution of Supersaturation in the Upper Troposphere from the Atmospheric Infrared Sounder, Journal of climate, 19(23), 6089–6103 doi:10.1175/JCLI3955.1, 2006.

Gettelman, A. and Kinnison, D. E.: The global impact of supersaturation in a coupled chemistry-climate model, Atmos. Chem. Phys., 7, 1629-1643, doi:10.5194/acp-7-1629-2007, 2007.

Gettelman, A., Hoor, P., Pan, L. L., Randel, W. J., Hegglin, M. I. and co-authors: The extratropical upper troposphere and lower stratosphere, Rev. Geophys. 49, RG3003, 2011.

Gettelman, A., Liu, X., Barahona, D., Lohmann, U., and Chen, C.: Climate impacts of ice nucleation, J. Geophys. Res. Atmos., 117(D20), doi:10.1029/2012JD017950, 2012.

Gierens, K. M., Schumann, U., Smit, H. G. J., Helten, M., and Zängl, G.: Determination of humidity and temperature fluctuations based on MOZAIC data and parametrisation of persistent contrail coverage for general circulation models, Ann. Geophys., 15, 1057–1066, doi:10.1007/s00585-997-1057-3, 1997.

Gierens, K., Schumann, U., Helten, M., Smit, H., and Marenco, A.: A distribution law for relative humidity in the upper troposphere and lower stratosphere derived from three years of MOZAIC measurements, Ann. Geophys., 17, 1218–1226, doi:10.1007/s00585-999-1218-7, 1999.

Gierens, K., Schumann, U., Helten, M., Smit, H., and Wang, P.: Ice-supersaturated regions and subvisible cirrus in the northern midlatitude upper troposphere, J. Geophys. Res. Atmos, 105, 22743–22753, doi:10.1029/2000JD900341, 2000.

Gierens, K., and Brinkop, S.: Dynamical characteristics of ice supersaturated regions. Atmos. Chem. Phys., 12, 11933–11942, doi:10.5194/acp-12-11933-2012, 2012.

Gilbert, R. O.: Statistical methods for environmental pollution monitoring, John Wiley & Sons, 1987.

Goff, J. A. and Gratch, S.: Low-pressure properties of water from-160 to 212 F, Trans. Amer. Soc. Heat. Vent. Eng, 52, 95–121, 1946.

Grise, K. M., Thompson, D. W. J., and Birner, T.: A global survey of static stability in the stratosphere and upper troposphere, J. Climate, 23, 2275-2292, doi:10.1175/2009JCLI3369.1, 2010.

Harries, J.E.: Atmospheric radiation and atmospheric humidity. Q. J. Roy. Met. Soc., 123, 2173–2186, doi:10.1002/qj.49712354402, 1997.

Hegglin, M. I., Brunner, D., Peter, T., Hoor, P., Fischer, H., Staehelin, J., Krebsbach, M., Schiller, C., Parchatka, U., and Weers, U.: Measurements of NO, NO_y, N_2O, and O_3 during SPURT: Implications for transport and chemistry in the lowermost stratosphere, Atmos. Chem. Phys., 6(5), 1331-1350, 2006.

Hegglin, M. I., C. D. Boone, G. L. Manney, and K. A. Walker: A global view of the extratropical tropopause transition layer from Atmospheric Chemistry Experiment Fourier Transform Spectrometer O_3, H_2O, and CO, J. Geophys. Res., 114, D00B11, doi:10.1029/2008JD009984, 2009.

Hegglin, M. I., Plummer, D. A., Shepherd, T. G., Scinocca, J. F., Anderson, J., Froidevaux, L., Funke, B., Hurst, D., Rozanov, A., Urban, J., von Clarmann, T., Walker, K. A., Wang, H. J., Tegtmeier, S., and Weigel, K.: Vertical structure of stratospheric water vapour trends derived from merged satellite data, Nat. Geosci., 7, 768–776, doi:10.1038/ngeo2236, 2014.

Held, I. M., and B. J. Soden: Water vapor feedback and global warming, Annu. Rev. Energy Environ., 25, 441–475, doi:10.1146/annurev.energy.25.1.441, 2000.

Helten, M., Smit, H., Sträter, W., Kley, D., Nédélec, P., Zöger, M., and Busen, R.: Calibration and performance of automatic compact instrumentation for the measurement of relative humidity from passenger aircraft, J. Geophys. Res. Atmos., 103, 25643–25652, doi:10.1029/98JD00536, 1998.

Helten, M., Smit, H., Kley, D., Ovarlez, J., Schlager, H., Baumann, R., Schumann, U., Nédélec, P., and Marenco, A.: In-flight comparison of MOZAIC and POLINAT water vapor measurements, J. Geophys. Res. Atmos, 104, 26087–26096, doi:10.1029/1999JD900315, 1999.

Heymsfield, A., Miloshevich, L. M., Twohy, C., Sachse, G., and Oltmans, S.: Upper-tropospheric relative humidity observations and implications for cirrus ice nucleation, Geophys. Res. Lett., 25(9), 1343–1346, doi:10.1029/98GL01089, 1998.

Hoerling, M. P., Schaack, T. K., and Lenzen, A. J.: Global objective tropopause analysis, Monthly Weather Review, 119(8), 1816-1831, doi:10.1175/1520-0493(1991)119¡1816:GOTA¿2.0.CO;2, 1991.

Hoinka, Klaus P.: Statistics of the Global Tropopause Pressure, Monthly Weather Review, 126 (12), 3303–25, doi:10.1175/1520-0493(1998)126¡3303:SOTGTP¿2.0.CO;2, 1998.

Holton, J. R., Haynes, P. H., McIntyre, M. E., Douglass, A. R., Rood, R. B., and Pfister, L.: Stratosphere-troposphere exchange, Rev. Geophys. 33, RG02097,doi:10.1029/95RG02097, 1995.

Hoor, P., Fischer, H., Lange, L., Lelieveld, J., Brunner, D.: Seasonal variations of a mixing layer in the lowermost stratosphere as identified by the CO-O3 correlation from in situ measurements, J. Geophys. Res. Atmos., 107, ACL 1-11, doi:10.1029/2000JD000289, 2002.

Hoor, P. and Gurk, C. and Brunner, D. and Hegglin, M. I. and Wernli, H., and Fischer, H.: Seasonality and extent of extratropical TST derived from in-situ CO measurements during SPURT, Atmos. Chem. Phys., 4, 1427–1442, doi:10.5194/acp-4-1427-2004, 2004.

Hoor, P., Wernli, H., Hegglin, M. I., and Bnisch, H.: Transport timescales and tracer properties in the extratropical UTLS, Atmos. Chem. Phys., 10, 7929–7944, doi:10.5194/acp-10-7929-2010, 2010.

IPCC: Climate Change 2013: The Physical Science Basis. Contribution of Working Group I to the Fifth Assessment Report of the Intergovernmental Panel on Climate Change, edited by: Stocker, T. F., Qin, D., Plattner, G.-K., Tignor, M., Allen, S. K., Boschung, J., Nauels, A., Xia, Y., Bex, V., and Midgley, P. M., Cambridge University Press, Cambridge, United Kingdom and New York, NY, USA, 1535 pp., doi:10.1017/CBO9781107415324, 2013.

Irvine, E. A. and Shine, K. P.: Ice supersaturation and the potential for contrail formation in a changing climate, Earth Syst. Dynam., 6, 555-568, doi:10.5194/esd-6-555-2015, 2015.

Ivanova, A. R.: The tropopause: Variety of definitions and modern approaches to identification, Russ. Meteorol. Hydrol., 38, 808–817, doi:10.3103/S1068373913120029, 2013.

Kley, D. and Stone, E.: Measurement of water-vapor in the stratosphere by photo-dissociation with Ly-alpha (1216 A) light, Rev. Sci. Instrum., 49, 691–697, doi:10.1063/1.1135596, 1978.

Kley, D., Russell III, J. M., and Phillips, C. (Eds.): SPARC Assessment of Upper Tropospheric and Stratospheric Water Vapour, WCRP – No. 113, WMO/TD – No. 1043, SPARC Report No. 2, Paris, 2000.

Kley, D., Smit, H. G. J., Nawrath, S., Luo, Z., Nédélec, P., and Johnson, R. H.: Tropical Atlantic convection as revealed by ozone and relative humidity measurements, J. Geophys. Res., 112, doi:10.1029/2007JD008599, 2007.

Koop, T., Luo, B., Tsias, A., and Peter, T.: Water activity as the determinant for homogeneous ice nucleation in aqueous solutions, Nature, 406(6796), 611-614, doi:10.1038/35020537, 2000.

Krämer, M., Schiller, C., Afchine, A., Bauer, R., Gensch, I., Mangold, A., Schlicht, S., Spelten, N., Sitnikov, N., Borrmann, S., de Reus, M., and Spichtinger, P.: Ice supersaturations and cirrus cloud crystal numbers, Atmos. Chem. Phys., 9, 3505–3522, doi:10.5194/acp-9-3505-2009, 2009.

Krämer, M., Rolf, C., Luebke, A., Afchine, A., Spelten, N., Costa, A., Meyer, J., Zöger, M., Smith, J., Herman, R. L., Buchholz, B., Ebert, V., Baumgardner, D., Borrmann, S., Klingebiel, M., and Avallone, L.: A microphysics guide to cirrus clouds - Part 1: Cirrus types, Atmos. Chem. Phys., 16, 3463-3483, doi:10.5194/acp-16-3463-2016, 2016.

Kunz, A., Schiller, C., Rohrer, F., Smit, H. G. J., Nédélec, P., and Spelten, N.: Statistical analysis of water vapour and ozone in the UTLS observed during SPURT and MOZAIC, Atmos. Chem. Phys., 8, 6603–6615, doi:10.5194/acp-8-6603-2008, 2008.

Kunz, A., Spelten, N., Konopka, P., Müller, R., Forbes, R. M., and Wernli, H.: Comparison of Fast In Situ Stratospheric Hygrometer (FISH) Measurements of Water Vapor in the Upper Troposphere and Lower Stratosphere (UTLS) with ECMWF (re)analysis Data, Atmos. Chem. Phys., 14 (19),10803–22, doi:10.5194/acp-14-10803-2014, 2014.

Lacis, A., Schmidt, G., Rind, D., and Ruedy, R.: Atmospheric CO_2: Principal control knob governing Earths temperature, Science, 330, 356–359, doi:10.1126/science.1190653, 2010.

Lamquin, N., Stubenrauch, C. J., Gierens, K., Burkhardt, U., and Smit, H.: A global climatology of upper-tropospheric ice supersaturation occurrence inferred from the Atmospheric Infrared Sounder calibrated by MOZAIC, Atmos. Chem. Phys., 12, 381- 405, doi:10.5194/acp-12-381-2012, 2012.

Lau,W. K., and Kim, K. M.: Robust Hadley circulation changes and increasing global dryness due to CO_2 warming from CMIP5 model projections, Proc. Natl. Acad. Sci. U. S. A., 112(12), 3630–3635, doi:10.1073/pnas.1418682112, 2015.

Liu, Y. S., Fueglistaler, S., and Haynes, P. H.: Advection–condensation paradigm for stratospheric water vapor, J. Geophys. Res. Atmos., 115(D24), doi:10.1029/2010JD014352, 2010.

Luo, Z., Kley, D., Johnson, R. H., and Smit, H.: Ten years of measurements of tropical upper-tropospheric water vapor by MOZAIC. Part I: Climatology, variability, transport, and relation to deep convection, J. Climate, 20, 418–435, doi:10.1175/JCLI3997.1, 2007.

Luo, Z., Kley, D., Johnson, R. H., and Smit, H.: Ten years of measurements of tropical upper-tropospheric water vapor by MOZAIC. Part II: Assessing the ECMWF humidity analysis, J. Climate, 21, 1449–1466, doi:10.1175/2007JCLI1887.1, 2008.

Lucas, J. M. and Saccucci, M. S.: Exponentially weighted moving average control schemes: properties and enhancements, Technometrics, 32, pp. 1–12, doi:10.2307/1269835, 1990.

Ma, H.-Y., Köhler, M., Li, J.-L. F., Farrara, J. D., Mechoso, C. R., Forbes, R. M., and Waliser,D. E.: Evaluation of an ice cloud parameterization based on a dynamical-microphysical lifetime concept using CloudSat observations and the ERA-Interim reanalysis, J. Geophys. Res., 117, D05210, doi:10.1029/2011JD016275, 2012.

Marenco, A., Thouret, V., Nédélec, P., Smit, H., Helten, M., Kley, D., Karcher, F., Simon, P., Law, K., Pyle, J., Poschmann, G., von Wrede, R., Hume, C., and Cook, T.: Measurement of ozone and water vapor by Airbus in-service aircraft: The MOZAIC airborne program, An overview, J. Geophys. Res., 103, 25631–25642, doi:10.1029/98JD00977, 1998.

May, R. and Webster, C.: Data processing and calibration for tunable diode-laser harmonic absorption spectrometers, J. Quant. Spectrosc. Ra., 49, 335–347, doi:10.1016/0022-4073(93)90098-3, 1993.

Meyer, J., Rolf, C., Schiller, C., Rohs, S., Spelten, N., Afchine, A., Zöger, M., Sitnikov, N., Thornberry, T. D., Rollins, A. W., Bozóki, Z., Tátrai, D., Ebert, V., Kühnreich, B., Mackrodt, P., Möhler, O., Saathoff, H., Rosenlof, K. H. and Krämer, M.: Two decades of water vapor measurements with the FISH fluorescence hygrometer: a review, Atmos. Chem. Phys. Discuss., 15, 7735–7782, doi:10.5194/acpd-15-7735-2015 , 2015.

Miloshevich, L.M., Paukkunen, A., Vomel, H. and Oltmans, S.J.: Development and validation of a time-lag correction for Vaisala radiosonde humidity measurements, J. Atmos. Ocean. Technol., 21,1305-1327, doi:10.1175/1520-0426(2004)021¡1305:DAVOAT¿2.0.CO;2, 2004.

Mitchell, D. L. and Finnegan, W.: Modification of cirrus clouds to reduce global warming, Environ. Res. Lett., 4, 045102, doi:10.1088/1748-9326/4/4/045102, 2009.

Mottaghy, D.: Ozonmessungen in der unteren Stratosphäre, Master thesis, Rheinisch-Westfälische Technische Hochschule Aachen, in cooperation with the Institute for Chemistry and Dynamics of the Geosphere, ICG-1: Stratosphere, 2001.

Müller, R., Kunz, A., Hurst, D. F., Rolf, C., Krämer, M., and Riese, M.: The need for accurate long-term measurements of water vapor in the upper troposphere and lower stratosphere with global coverage, Earth's Future, 4, 25–32, doi:10.1002/2015EF000321, 2016.

Nédélec, P., Blot, R., Boulanger, D., Athier, G., Cousin, J.-M., Gautron, B., Petzold, A., Volz-Thomas, A., and Thouret, V.: Instrumentation on commercial aircraft for monitoring the atmospheric composition on a global scale: the IAGOS system, technical overview of ozone and carbon monoxide measurements, Tellus B, 67, 27791, doi:10.3402/tellusb.v67.27791, 2015.

Nedoluha, G. E., Bevilacqua, R. M., and Hoppel, K. W.: POAM III measurements of dehydration in the Antarctic and comparisons with the Arctic, J. Geophys. Res., 107, 8290, doi:10.1029/2001JD001184, 2002.

Nedoluha, G. E., Benson, C. M., Hoppel, K.W., Alfred, J., Bevilacqua, R. M., and Drdla, K.: Antarctic dehydration 1998-2003: Polar ozone and aerosol measurement III (POAM) measurements and integrated microphysics and aerosol chemistry on trajectories (IMPACT) results with four meteorological models, J. Geophys. Res., 112, D07305, doi:10.1029/2006JD007414, 2007.

Neis, P., Smit, H. G. J., Krämer, M., Spelten, N., and Petzold, A.: Evaluation of the MOZAIC Capacitive Hygrometer during the airborne field study CIRRUS-III, Atmos. Meas. Tech., 8, 1233-1243, doi:10.5194/amt-8-1233-2015, 2015a.

Neis, P., Smit, H. G. J., Rohs, S., Bundke, U., Krämer, M., Spelten, N., Ebert, V., Buchholz, B., Thomas, K., and Petzold, A.: Quality assessment of MOZAIC and IAGOS capacitive hygrometers: insights from airborne field studies, Tellus B, 67, 28320, doi:10.3402/tellusb.v67.28320, 2015b.

Ovarlez, J., Gayet, J. F., Gierens, K., Ström, J., Ovarlez, H., Auriol, F., Busen, R., and Schumann, U.: Water vapour measurements inside cirrus clouds in Northern and Southern hemispheres during INCA, Geophy. Res. Lett, 29(16), doi:10.1029/2001GL014440, 2002.

Pan, L. L. and Randel, W. J. and Gary, B. L. and Mahoney, M. J., and Hintsa, E. J.: Definitions and sharpness of the extratropical tropopause: A trace gas perspective, J. Geophys. Res. Atmos., 109, D23103, doi:10.1029/2004JD004982, 2004.

Pan, L. L., Bowman, K. P., Shapiro, M., Randel, W. J., Gao, R. S., Campos, T., Davis, C., Schauffler, S., Ridley, B. A., Wei, J. C., and Barnet, C.: Chemical behavior of the tropopause observed during the Stratosphere-Troposphere Analyses of Regional Transport experiment, J. Geophys. Res., 112, D18110, doi:10.1029/2007JD008645, 2007.

Pan, L. L., Kunz, A., Homeyer, C. R., Munchak, L. A., Kinnison, D. E., and Tilmes, S.: Commentary on using equivalent latitude in the upper troposphere and lower stratosphere, Atmos. Chem. Phys., 12, 9187-9199, doi:10.5194/acp-12-9187-2012, 2012.

Peixoto, J. P. and Oort, A. H.: The climatology of Relative Humidity in the Atmosphere, J. Climate, 9, 3443–3463, doi:10.1175/1520-0442(1996)009¡3443:TCORHI¿2.0.CO;2, 1996.

Petetin, H., Thouret, V. ,Fontaine, A., Sauvage, B., Athier, G, Blot, R., Boulanger, D., Cousin, J.-M., and Nédélec, P.: Characterizing tropospheric ozone and CO around Frankfurt between 1994–2012 based on MOZAIC-IAGOS aircraft measurements, Atmos. Chem. Phys., 16, 15147–15163, doi:10.5194/acp-16-15147-2016, 2015.

Petzold, A., Volz-Thomas, A., Thouret, V., Cammas, J.-P., and Brenninkmeijer, C.: IAGOS – In-service Aircraft for a Global Observing System, in: 3rd International Conference on Transport, Atmosphere and Climate, Germany, 25–28 June 2012, 69–76, 2013.

Petzold, A., Thouret, V., Gerbig, C., Zahn, A., Brenninkmeijer, C. A. M., Gallagher, M., Hermann, M., Pontaud, M., Ziereis, H., Boulanger, D., Marshall, J., Nédélec, P., Smit, H. G. J., Firess, U., Flaud, J.-M., Wahner, A., Cammas, J.-P., and Volz-Thomas, A.: Global-Scale Atmosphere Monitoring by In-Service Aircraft - Current Achievements and Future Prospects of the European Research Infrastructure IAGOS, Tellus B, 67, 28452, doi:10.3402/tellusb.v67.28452, 2015.

Petzold, A., Krämer, M., Neis, P., Rolf, C., Rohs, S., Berkes, F., Smit, H. G. J., Gallagher, M., Beswick, K., Lloyd, G., Baumgardner, D., Spichtinger, P., Nédélec, P., Ebert, V., Buchholz, B., Riese, M., and Wahner, A.: Upper tropospheric water vapour and its interaction with cirrus clouds as seen from IAGOS long-term routine in-situ observations, Faraday Discuss., doi:10.1039/C7FD00006E, 2017.

Ploeger, F., Günther, G., Konopka, P., Fueglistaler, S., Müller, R., Hoppe, C., Kunz, A., Spang, R., Groo, J.-U., and Riese, M.: Horizontal water vapor transport in the lower stratosphere from subtropics to high latitudes during boreal summer, J. Geophys. Res. Atmos., 118,8111–8127, doi:10.1002/jgrd.50636, 2013.

Plumb, R. A.: Stratospheric transport, J. Meteorol. Soc. Jpn., 80, 793–809, doi:10.2151/jmsj.80.793, 2002.

Riese, M., Ploeger, F., Rap, A., Vogel, B., Konopka, P., Dameris, M., and Forster, P.: Impact of uncertainties in atmospheric mixing on simulated UTLS composition and related radiative effects, J. Geophys. Res. Atmos., 117, D16305, doi:10.1029/2012JD017751, 2012.

Randel, W. J., Wu, F., Vömel, H., Nedoluha, G. E., and Forster, P.: Decreases in stratospheric water vapor after 2001: Links to changes in the tropical tropopause and the Brewer-Dobson circulation, J. Geophys. Res., 111, D12312, doi:10.1029/2005JD006744, 2006.

Rohs, S., Schiller, C., Riese, M., Engel, A., Schmidt, U., Wetter, T, Levin, I., Nakazawa, T., and Aoki, S.: Long-term changes of methane and hydrogen in the stratosphere in the period 1978 – 2003 and their impact on the abundance of stratospheric water vapor, J. Geophys. Res., 111, D14315, doi:10.1029/2005JD006877, 2006.

Rolf, C., Afchine, A., Bozem, H., Buchholz, B., Ebert, V., Guggenmoser, T., Hoor, P., Konopka, P., Kretschmer, E., Müller, S., Schlager, H., Spelten, N., Suminska-Ebersoldt, O., Ungermann, J., Zahn, A., and Krämer, M.: Transport of Antarctic stratospheric strongly dehydrated air into the troposphere observed during the HALO-ESMVal campaign 2012, Atmos. Chem. Phys., 15, 9143-9158, doi:10.5194/acp-15-9143-2015, 2015.

Rollins, A. W., Thornberry, T. D., Gao, R. S., Smith, J. B., Syares, D. S., Sargent, M. R., Schiller, C., Krämer, M., Spelten, N., Hurst, D. F., Jordan, A. F., Hall, E. G., Vömel, H., Diskin, G. S., Podolske, J. R., Christensen, L. E., Rosenlof, K. H., Jensen, E. J., and Fahey, D. W.: Evaluation of UT/LS hygrometer accuracy by intercomparison during the NASA MACPEX mission, J. Geophys. Res. Atmos., 119, 1915–1935, doi:10.1002/ 2013JD020817, 2014.

Rosenlof, K. H., Oltmans, S. J., Kley, D., Russell III, J. M., Chiou, E.-W., Chu, W. P., Johnson, D. G., Kelly, K. K., Michelsen, H. A., Nedoluha, G. E., Remsberg, E. E., Toon, G. C., and McCormick, M. P. : Stratospheric water vapor increases over the past half century, Geophys. Res. Lett., 28, 1195–1199, doi:10.1029/2000GL012502, 2001.

Sassen, K., Wang, Z., and Liu, D.: Global distribution of cirrus clouds from CloudSat/Cloud−Aerosol lidar and infrared pathfinder satellite observations (CALIPSO) measurements, J. Geophys. Res. Atmos., 113, D00A12, doi:10.1029/2008JD009972, 2008.

Sawa, Y., Machida, T., and Matsueda, H.: Seasonal variations of CO2 near the tropopause observed by commercial aircraft, J. Geophys. Res. Atmos., 113, D23301, doi:10.1029/2008JD010568, 2008.

Schlager, H., Konopka, P., Schulte, P., Schumann, U., Ziereis, H., Arnold, F., Klemm, M., Hagen, D., Whitefield, P., and Ovarlez, J.: In situ observations of air traffic emission signatures in the North Atlantic flight corridor, J. Geophys. Res., 102, 10739–10750, doi:10.1029/96JD03748, 1997.

Schneider, T., OGorman, P. A., and Levine, X. J.: Water vapor and the dynamics of climate changes, Rev. Geophys., 48, RG3001, doi:10.1029/2009RG000302, 2010.

Schumann, U.: Pollution from aircraft emissions in the North Atlantic flight corridor (POLINAT), Air Pollut. Res. Rep. 58, Rep. EUR 16978 EN, Europ. Commission, Luxembourg, 1997.

Seidel, D. J., Berger, F. H., Diamond, H. J., Dykema, J., Goodrich, D., Immler, F., Murray, W., Peterson, T., Sisterson, D., Sommer, M., Thorne, P., Vömel, H., and Wang, J.: Reference upper-air observations for climate: rationale, progress, and plans, Bull. Am. Meteorol. Soc., 90, 361–369, doi:10.1175/2008BAMS2540.1, 2009.

Shi, L., and Bates, J. J.: Three decades of intersatellite-calibrated High-Resolution Infrared Radiation Sounder upper tropospheric water vapor, J. Geophys. Res., 116, D04108, doi:10.1029/2010JD014847, 2011.

Simmons, A. J., Poli, P., Dee, D. P., Berrisford, P., Hersbach, H., Kobayashi, S., and Peubey, C.: Estimating Low-Frequency Variability and Trends in Atmospheric Temperature Using ERA-Interim, Q. J. R. Meteorol. Soc., 140 (679), 329–53, doi:10.1002/qj.2317, 2014.

Smit, H., Sträter, W., Helten, M., and Kley, D.: Environmental Simulation Facility to Calibrate Airborne Ozone and Humidity Sensors, Tech. rep., Berichte des Forschungszentrums Jülich; Report No. 3796, 2000.

Smit, H. G. J., Volz-Thomas, A., Helten, M., Paetz, W., and Kley, D.: An in-flight calibration method for near-real-time humidity measurements with the airborne MOZAIC sensor, J. Atmos. Ocean. Tech., 25, 656–666, doi:10.1175/2007JTECHA975.1, 2008.

Smit, H. G. J., Rohs, S., Neis, P., Boulanger, D., Krämer, M., Wahner, A., and Petzold, A.: Technical Note: Reanalysis of upper troposphere humidity data from the MOZAIC programme for the period 1994 to 2009, Atmos. Chem. Phys., 14, 13241–13255, doi:10.5194/acp-14-13241-2014, 2014.

Solomon, S., Garcia, R. R., and Stordal, F.: Transport processes and ozone perturbations, J. Geophys. Res., 90, 12,981-12,989, doi:10.1029/JD090iD07p12981, 1985.

Solomon, S., Rosenlof, K., Portmann, R., Daniel, J., Davis, S., Sanford, T., and Plattner, G.-K.: Contributions of stratospheric water vapor to decadal changes in the rate of global warming, Science, 327, 1219–1223, doi:10.1126/science.1182488, 2010.

Sonntag, D.: Advancements in the field of hygrometry, Meteorol. Z., 3, 51–66, 1994.

Spang, R., Günther, G., Riese, M., Hoffmann, L., Müller, R., and Griessbach, S.: Satellite observations of cirrus clouds in the Northern Hemisphere lowermost stratosphere. Atmos. Chem. Phys., 15(2), 927–950, doi:10.5194/acp-15-927-2015, 2015.

Spichtinger, P., Gierens, K., and Read, W.: The statistical distribution law of relative humidity in the global tropopause region, Meteorol. Z., 11, 83–88, doi:10.1127/0941-2948/2002/0011-0083, 2002.

Spichtinger, P., Gierens, K., Leiterer, U., and Dier, H.: Ice supersaturation in the tropopause region over Lindenberg, Germany, Meteorol. Z., 12, 143–156, doi:10.1127/0941-2948/2003/0012-0143, 2003a.

Spichtinger, P., Gierens, K., and Read, W.: The global distribution of ice-supersaturated regions as seen by the Microwave Limb Sounder, Q. J. Roy. Meteor. Soc., 129, 3391-3410, doi:10.1256/qj.02.141, 2003b.

Spichtinger, P., Gierens, K., Smit, H. G. J., Ovarlez, J., and Gayet, J.-F.: On the distribution of relative humidity in cirrus clouds, Atmos. Chem. Phys., 4, 639–647, doi:1680-7324/acp/2004-4-639, 2004.

Spichtinger, P. and Gierens, K.: Modelling of cirrus clouds – Part 1a: Model description and validation, Atmos. Chem. Phys., 9, 685–706, doi:10.5194/acp-9-685-2009, 2009.

Spichtinger, P.: Shallow cirrus convection—a source for ice supersaturation, Tellus A, 66, 19937, doi:10.3402/tellusa.v66.19937, 2014.

Spichtinger, P. and Leschner, M.: Horizontal scales of ice-supersaturated regions, Tellus B, 68, 29020, doi:10.3402/tellusb.v68.29020, 2016.

Sprenger, M. and Wernli, H.: A northern hemispheric climatology of cross-tropopause exchange for the ERA15 time period (1979–1993), J. Geophys. Res. Atmos., 108, 8521, doi:10.1029/2002JD002636, 2003.

Stickney, T. M., Shedlov, M., and Thompson, D. I.: Rosemount total temperature sensors, Tech. rep., 5755, Revision B, Aerosp. Div. Rosemount Inc., 1990.

Stubenrauch, C. J., Cros, S., Guignard, A., and Lamquin, N.: A six-year global cloud climatology from the Atmospheric Infrared Sounder aboard the Aqua satellite: Statistical analysis in synergy with CALIPSO and CloudSat, Atmos. Chem. Phys., 10, 7197-7214, doi:10.5194/acp-10-7197-2010, 2010.

Thompson, A. M.: The oxidizing capacity of the earths atmosphere: Probable past and future changes, Science, 256, 1157–1165, doi:10.1126/science.256.5060.1157, 1992.

Thouret, V., Marenco, A., Logan, J., Nédélec, P., and Grouhel, C.: Comparisons of ozone measurements from the MOZAIC airborne program and the ozone sounding network at eight locations, J. Geophys. Res. Atmos., D19, 25695–25720, doi:10.1029/98JD02243, 1998a.

Thouret, V., Marenco, A., Nédélec, P., and Grouhel, C.: Ozone climatologies at 9-12 km altitude as seen by the MOZAIC airborne program between September 1994 and August 1996, J. Geophys. Res. Atmos., 103(D19), 25653–25679, doi:10.1029/98JD01807, 1998b.

Thouret, V., Cammas, J.-P., Sauvage, B., Athier, G., Zbinden, R., Nédélec, P., Simon, P., and Karcher, F.: Tropopause referenced ozone climatology and inter-annual variability (1994-2003) from the MOZAIC programme: a review, Atmos. Chem. Phys., 6, 1033–1051, doi:10.5194/acp-6-1033-2006, 2006.

Tilmes, S., Pan, L. L., Hoor, P., Atlas, E., Avery, M. A., Campos, T., Christensen, L. E., Diskin, G. S., Gao, R.-S., Herman, R. L., Hintsa, E. J., Loewenstein, M., Lopez, J., Paige, M. E., Pittman, J. V., Podolske, J. R., Proffitt, M. R., Sachse, G. W., Schiller, C., Schlager, H., Smith, J., Spelten, N., Webster, C., Weinheimer, A., and Zondlo, M. A.: An aircraft-based upper troposphere lower stratosphere O3 , CO, and H2O climatology for the Northern Hemisphere, J. Geophys. Res., D14, D14303, doi:10.1029/2009JD012731, 2010.

Tompkins, A. M., Gierens, K., and Rädel, G.: Ice supersaturation in the ECMWF integrated forecast system, Q. J. R. Meteorol. Soc., 133, 53–63, doi:10.1002/qj.14, 2007.

van der Ent, R. J. and Tuinenburg, O. A.: The residence time of water in the atmosphere revisited, Hydrol. Earth Syst. Sci., 21, 779-790, doi:10.5194/hess-21-779-2017, 2017.

Volz-Thomas, A. and Cammas, J.-P., Brenninkmeijer, C. A. M., Machida, T., Cooper, O., Sweeney, C., and Waibel, A.: Civil Aviation Monitors Air Quality and Climate, EM Magazine, Air & Waste Management Association., 16–19, Oct. 2009.

Vömel, H., David, D. E., and Smith, K.: Accuracy of tropospheric and stratospheric water vapor measurements by the cryogenic frost point hygrometer: Instrumental details and observations, J. Geophys. Res., 112, D08305, doi:10.1029/2006JD007224, 2007.

Wendisch, M., Pilewskie, P., Pommier, J., Howard, S., Yang, P., Heymsfield, A. J., Schmitt, C. G., Baumgardner, D., and Mayer, B.: Impact of cirrus crystal shape on solar spectral irradiance: A case study for subtropical cirrus, J. Geophys. Res., 110, D03202, doi:10.1029/2004JD005294, 2005.

Wendisch, M., Yang, P., and Pilewskie, P.: Effects of ice crystal habit on thermal infrared radiative properties and forcing of cirrus. J. Geophys. Res., 112(D8), doi:10.1029/2006JD007899, 2007.

Wild, M., Folini, D., Schrär, C., Loeb, N., Dutton, E. G., and König-Langlo, G.: The global energy balance from a surface perspective, Clim. Dyn. 40, 3107–3134, doi:10.1007/s00382-012-1569-8, 2013.

Wildmann, N. and Kaufmann, F. and Bange, J.: An inverse-modelling approach for frequency response correction of capacitive humidity sensors in ABL research with small remotely piloted aircraft (RPA), Atmos. Meas. Tech., 7, 3059–3069, doi:10.5194/amt-7-3059-2014, 2014.

WMO (World Meteorological Organization): Meteorology – A three-dimensional science: Second Session of the Commission for Aerology, WMO Bull. IV(4), WMO, Geneva, 134–138, 1957.

Zahn, A., Brenninkmeijer, C. A. M., and van Velthoven, P. F. J.: Passenger aircraft project CARIBIC 1997-2002, Part I: the extratropical chemical tropopause, Atmos. Chem. Phys. Discuss., 4, 1091-1117, doi:10.5194/acpd-4-1091-2004, 2004.

Zahn A., E. Christner, P. F. J. van Velthoven, A. Rauthe-Schch, and C. A.M. Brenninkmeijer: Processes controlling water vapor in the upper troposphere/lowermost stratosphere: An analysis of 8 years of monthly measurements by the IAGOS-CARIBIC observatory, J. Geophys. Res. Atmos., 119, 11, 505-11, 525, doi:10.1002/ 2014JD021687, 2014.

Zöger, M., Afchine, A., Eicke, N., Gerhards, M., Klein, E., McKenna, D., Morschel, U., Schmidt, U., Tan, V., Tuitjer, F., Woyke, T., and Schiller, C.: Fast in situ stratospheric hygrometers: A new family of balloon-borne and airborne Lyman alpha photofragment fluorescence hygrometers, J. Geophys. Res., 104, 1807–1816, doi:10.1029/1998JD100025, 1999.

LIST OF FIGURES

LIST OF TABLES

Band / Volume 381
Untersuchungen zur Deckschichtbildung auf $LiNi_{0,5}Mn_{1,5}O_4$-Hochvoltkathoden
Die Kathoden/Elektrolyt-Grenzfläche in Hochvolt-Lithium-Ionen-Batterien
K. Wedlich (2017), xvi, 157, xvii-xxvi pp
ISBN: 978-3-95806-249-8

Band / Volume 382
Charakterisierung gradierter Eisen/Wolfram-Schichten für die erste Wand von Fusionsreaktoren
S. Heuer (2017), x, 234 pp
ISBN: 978-3-95806-252-8

Band / Volume 383
High resolution imaging and modeling of aquifer structure
N. Güting (2017), viii, 107 pp
ISBN: 978-3-95806-253-5

Band / Volume 384
IEK-3 Report 2017
Sektorkopplung –
Forschung für ein integriertes Energiesystem
(2017), 182 pp
ISBN: 978-3-95806-256-6

Band / Volume 385
Bestimmung der Wolframerosion mittels optischer Spektroskopie unter ITER-relevanten Plasmabedingungen
M. Laengner (2017), vi, 184, XI pp
ISBN: 978-3-95806-257-3

Band / Volume 386
IEK-3 Report 2017
Sector Coupling –
Research for an Integrated Energy System
(2017), 175 pp
ISBN: 978-3-95806-258-0

Band / Volume 387
Photochemistry of Highly Oxidized Multifunctional Organic Molecules: a Chamber Study
L. I. M. Pullinen (2017), II, 96, xviii pp
ISBN: 978-3-95806-260-3

Band / Volume 388
Poröse Transportschichten für die Polymerelektrolytmembran-Wasserelektrolyse
M. Höh (2017), VI, 186 pp
ISBN: 978-3-95806-262-7

Band / Volume 389
Modelling of High Temperature Polymer Electrolyte Fuel Cells
Q. Cao (2017), 173 pp
ISBN: 978-3-95806-263-4

Band / Volume 390
Potential use of nitrification inhibitors for mitigating N_2O emission from soils
D. Wu (2017), 206 pp
ISBN: 978-3-95806-264-1

Band / Volume 391
Mechanical Characterization of Solid Oxide Fuel Cells and Sealants
J. Wei (2017), II, 151 pp
ISBN: 978-3-95806-266-5

Band / Volume 392
Microcrystalline Silicon Carbide for Silicon Heterojunction Solar Cells
M. B. Pomaska (2017), 150 pp
ISBN: 978-3-95806-267-2

Band / Volume 393
Einfluss der Kristallisation auf das Fließverhalten oxidischer Schmelzen
S. Seebold (2017), 168 pp
ISBN: 978-3-95806-268-9

Band / Volume 394
Water vapour in the UTLS – Climatologies and Transport
P. R. Neis (2017), x, 124 pp
ISBN: 978-3-95806-269-6

Energie & Umwelt /
Energy & Environment
Band / Volume 394
ISBN 978-3-95806-269-6